ACTIVE, POLYMER-BASED COMPOSITE MATERIAL IMPLEMENTING SIMPLE SHEAR

A Dissertation

by

SANG JIN LEE

Submitted to the Office of Graduate Studies of
Texas A&M University
in partial fulfillment of the requirements for the degree of

DOCTOR OF PHILOSOPHY

December 2008

Major Subject: Mechanical Engineering

ACTIVE, POLYMER-BASED COMPOSITE MATERIAL IMPLEMENTING SIMPLE SHEAR

A Dissertation

by

SANG JIN LEE

Submitted to the Office of Graduate Studies of
Texas A&M University
in partial fulfillment of the requirements for the degree of

DOCTOR OF PHILOSOPHY

Approved by:

Chair of Committee, Terry S. Creasy
Committee Members, Alan B. Palazzolo
James G. Boyd
Jyhwen Wang
Head of Department, Dennis O`Neal

December 2008

Major Subject: Mechanical Engineering

ABSTRACT

Active, Polymer-Based Composite Material
Implementing Simple Shear.
(December 2008)
Sang Jin Lee, B.S.; M.S., Ajou University;
M.S., The Pennsylvania State University
Chair of Advisory Committee: Dr. Terry S. Creasy

A novel active material for controllable, high work density applications was designed, fabricated, analyzed, and tested. This active material uses a lens-shaped element to implement simple shear motion with gas pressure actuation. The lens element is a bladder-filled Kevlar fabric embedded in a polyurethane matrix.

The polyurethane's hyperelastic material parameters were found by experiment and estimated by numerical analysis. The Ogden material constant set found shows good agreement within the shear actuator's working range.

A fabricated, single-element shear actuator reached 34.2% free shear strain when pressurized to 1.03 MPa. A unitary shear actuator was modeled as were single-acting and dual-acting shear actuator arrays so that solitary and multi-cell behaviors were estimated. Actuator work performance and power from nonlinear finite element analysis found conventional work density is 0.2289 MJ/m^3 and 0.2482 MJ/m^3, for the single-acting and double-acting shear actuator, respectively. Scientific work densities are

0.0758 MJ/m^3 and 0.0375 MJ/m^3, for single-acting and double-acting shear actuators, respectively. Calculation shows the volumetric power for a single-acting shear actuator is 0.4578 MW/m^3 and 0.4964 MW/m^3 for the double-acting shear actuator.

Finally, a nastic actuator is applied to twist a generic structural beam. The nastic-material actuated structure has an advantage over conventional actuator systems. Work per unit volume for nastic materials is 2280~8471% higher than conventional, discrete actuators that use electric motors. When compared by work per unit mass, this nastic actuator is 2592~13900% better than conventional actuator because nastic actuator is made from lighter materials and it distributes the actuation throughout the structure, which eliminates connecting components.

The nastic actuator's volumetric power is 2217~8602% higher than conventional actuators. Finally, the nastic actuator is 2656~14269% higher than conventional actuators for power per unit mass.

DEDICATION

To Jesus Christ, my parents, my wife, Younju, my son, Hyun Soo, my daughter, Abigail, my brother, and my academic advisor, Dr. Terry S. Creasy.

ACKNOWLEDGEMENTS

This material is based upon work supported by DARPA and the U.S. Army Research, Development and Engineering Command under contract W911 W6-04-C-0069. I thank them for providing the financial support for performing my research.

I would like to express special thanks to my advisor Dr. Terry S. Creasy for his guidance, encouragement, and support throughout my graduate study at Texas A&M University. I would also like to thank my committee members, Dr. Palazzolo, Dr. Boyd, and Dr. Jyhwen Wang, for their insight and feedback.

I am also deeply thankful to my labmates, Jaehyeuk, Gene, Roston, Viral, Omotayo, and Dr. Jonghyun Kim, for their assistance while finishing my study.

I am greatly indebted to my parents and parents-in-law for their continuous support and encouragement. I also would like to express special thanks to my wife, Youn Ju Kim, my son, Hyun Soo, and daughter, Abigail, for their love, prayers, and strong encouragement.

Lastly, but first of all, I would like to express special, special thanks to my Lord, Jesus Christ who made all things, including this study, possible. May He receive all the honor and glory due him.

TABLE OF CONTENTS

Page

CHAPTER

CHAPTER Page

CHAPTER Page

Page

LIST OF FIGURES

Page

Page

Page

LIST OF TABLES

CHAPTER I

INTRODUCTION

1.1 Motivation and Significance of the Research

Conventional mechanical actuation needs many mechanical links and joints, for example, in variable-sweep aircraft wings and in flight control surfaces. In addition, there has been a continuous search for lighter materials and efficient structures in the transport industry—especially in aerospace because flying vehicles must meet weight constraints [1]. Adaptive/shape-changing materials might enable a structure to change its functional shape or its material/structural properties; therefore, shape-changing materials might replace complex mechanical links and actuators with integral, that is, embedded and bonded, acutators. These materials might reduce overall weight and energy used for actuation because no—or fewer—links would be necessary to move loads from the actuator to the structure.

Recently, Sater and Main suggested a new mechanical motion concept: nastic materials [2]. These active materials will mimic a plant's ability to generate large strains while still performing a structural function. Unlike conventional mechanical actuators,

---

This dissertation follows the style of Journal of Biomedical Materials Research Part B: Applied Biomaterials.

nastic material distributes actuators throughout the structure. This material might enable fast, continuous, and large shape changes.

Current shape changing structures have few degrees-of-freedom. Variable sweep wings, variable pitch propellers, flaps, and rudders have a single degree of freedom. For these structures hinges and bearings carry structural and actuation loads. Hinges and bearings constrain the degrees of freedom. True morphing wings might need three or four degrees of freedom and the wings might requires smooth, continuous shape changes [2].

A shape-changing material inspired by plant motion has many degrees of freedom—perhaps with a low weight penalty for the additional capability—and must maintain structural integrity throughout its motion range. This is the motivation for creating this material and it drives this research. The first step in applying nastic materials is to define the issues critical to their design and use.

.

1.2 Definition of the Critical Issues

Tzou et al. [3] states that functional, shape changing materials can be employed only when research addresses these critical issues:

1. Design, modeling, simulating, optimizing
2. Controlling, precisely actuating, signal-processing, transducer systems
3. Manufacturing, controlling quality, producing the material
4. Structures, structural dynamics, monitoring

5. Materials, composites, integration, material systems
6. Reliability, failure analysis
7. Applied mathematics, numerical tools
8. Computers, microprocessor, CAD/CAM
9. Electrofluids, optics, multifield coupling

Integrating these issues is essential to producing a novel active material with large strains and high work density that carries structural loads. This material should have distributed shape-changing capability throughout to enable highly adaptable, conformable structures. This thesis covers three aspects from Tzou's critical issue list. These aspects are

- Design, modeling: Element design is based on an elementary analysis.
  Nastic actuator performance is estimated from numerical models.
- Materials: High stiffness fibers and elastomer matrix.
  A hyperelastic material, which has non-linear large deformation behavior, is characterized.
- Structures: Twisting beam structure.
  System level performance for a twisting beam is estimated and discussed.

1.3 Research Goal and Objectives

The research goal was to develop a novel active material with functions inspired by plant nastic motion. The material had to obtain high work performance with its deformation dominated by simple shear with relatively small—or zero—volumetric expansion while carrying structural loads. To achieve this goal, this research had these objectives:

- To measure the hyperelastic material parameters for a polyurethane matrix
- To design the lens-shaped element to achieve best shear deformations
- To built a single direction shear actuator and measure its free strain behavior
- To develop a numerical model for single and multi-cell shear actuators and predict their work performance
- To build a nastic-actuated, split beam model in FEA compare it to a conventional actuator

CHAPTER II

LITERATURE REVIEW

2.1 Smart Materials and Systems

Smart materials—sometimes called active materials—can change their shape or properties by a pre-set program or by responding to an external stimulus. Commercial smart materials include piezoelectrics, shape memory alloys, electrostrictive materials, and magnetostrictive materials. This section reviews the history, characteristics, advantages, and drawbacks these materials have.

2.1.1 Smart/Active materials

This section presents four active materials:

MAGNETOSTRICTIVE MATERIALS

Magnetostrictive materials change their length in response to a magnetic field. The magnetic force causes strains by aligning magnetic domains. This phenomena was first discovered in 1842 by James Prescott Joule, and it is called the Joule effect after him [1, 3]. While most materials have a weak magentostictive effect, commercial alloy Terfenol-D can have larger strains at moderate magnetic strength than a piezoelectric material has under great electric charge [4, 5].

According to Banks et al. [6], a magnetostrictive material has these drawbacks:

- The governing equation for magnetic field strength and generated strain is inherently nonlinear.
- The material has hysteresis.
- Magnetostrictive materials are heavy and large.

PIEZOELECTRIC MATERIALS

Piezoelectric materials were also found in the 19th century. The Curie brothers are credited first observed this material in 1880 [1, 7]. Piezoelectricity means “pressure electricity”. Piezoelectric materials produce electricity upon pressure loading; therefore, they make good sensors. Also, piezoelectrics deform under an applied electric field; therefore, they make good actuators. Their stress/strain and electric field/voltage response is coupled.

Piezoelectricity is a first-order effect at low electric field, and at this field level strain is proportional to the electric field. The displacement direction depends on whether the electric field is positive or negative. But, under a high electric field, electromechanical hysteresis occurs and this hysteresis causes servodisplacement control problems in precision actuation at large-stroke [3, 8].

Many applications employ piezoelectric materials. For example, ultrasonic transducers, accelerometers, gramophones, resonators, filters, and ink-jet printers use piezoelectrics to work.

SHAPE MEMORY ALLOYS

Mechanically deformed shape memory alloys (SMA) return to their original shape at an actuation temperature. This is called the shape-memory effect. SMA material has a thermo-mechanical energy transformation [1, 5-7]. Chang and Read found this behavior in a gold cadmium (AuCd) sample in 1932 [3]. Later, in 1938, that behavior was found in brass. By 1962, Buehler, Gilfrich and Wiley observed shape-memory effect in nickel-titanium alloy. They called it Nitinol (NiTi). NiTi is the dominant commercial SMA in the market.

The shape-memory effect comes from the NiTi alloy's shift between austenite and martensite structures. The SMA microstructure is martensite at low temperature. At higher temperature, SMA exhibits the austenite structure, which is more rigid than martensite. An actuator exhibits free strains to 8% [5]. Thus, it will generate large forces when constrained.

SMA has these drawbacks:

- Response is slow, there are large thermal time constants,
- Temperature range is limited, the temperature must support the phase change region
- Energy input is large, heat is lost to the system

The constitutive equations for SMA structures are found in Lagoudas, Boyd, Aboudi.[9-11]. For recent structural applications, Elzey et al. studied a sandwich panel that has SMA facesheets and stainless steel core [12] in 2002. It showed shape-reversing sandwich panel with a one-way shape-memory effect. In 2003, Dano et al. [13] developed a theory for SMA wires applied to unsymmetric laminates. The SMA wires changed the equilibrium configuration—the laminate will snap-through from one position to another. They claimed the laminate's overall shape change can be predicted from the SMA wire temperature.

ELECTROSTRICTIVE MATERIALS

Another active material is electrostrictive. Electrostrictive material is like magnetostrictive material except that an applied electric field generates mechanical deformations. Electrostrictive materials can perform as sensors and actuators.

Dielectric materials have these drawbacks:

- Their strain-field relations and field-dependent parameters are nonlinear
- The elements are temperature dependent.

2.1.2 Shape changing structures

Dean and James presented the seminal adaptive/shape changing structure technology in 1974 [14]. They developed an adaptive structure that corrects errors in a mirrored surface using forces produced by piezoelectric actuators.

Lucato et al. [15] constructed a shape morphing structure by using a Kagome lattice structure [16]. Kagome is a Japanese word representing a basket weave pattern. The structure has a stainless steel active face and core, with a polycarbonate passive core, and electric motor actuators. Two shape changes—hinging and twisting—are possible for this structure. The authors claim this structure can sustain large passive load with light weight.

Research about morphing aircraft wings is active [17-20]. The idea is—unlike variable sweep wings—to change the whole wing's shape and area, so that an aerospace vehicle could be a multi-purpose platform. For example, one structure might be a fighter, a heavy carrier, and a reconnaissance aircraft.

Most researchers employ shape memory alloys for wing morphing because wing shape change requires high actuation forces and shape memory alloys are the best candidates to meet this requirement so far.

After 2003, Cadogan et al. [21-26] studied a morphing inflatable wing for a small Unmanned Aerial Vehicle (UAV). Their wing morphing is for roll control. The wing's aft end causes section camber changes. The authors employed nastic structure concepts as a candidate for actuation along with other means, for example, piezoelectrics, pneumatics, shape memory alloys, electric motors, and hydraulics [21, 22]. Section 2.3 presents the Cadogan work in more detail.

In 2007 and 2008, NewScientistTech magazine [27, 28] reported that researchers from the Netherlands are making a small unmanned aircraft that mimics bird's wing changes. Lentink and his colleagues took the idea from swifts [29, 30]. They call their small UAV "RoboSwift" [28]. It has four individual wing regions hinged and connected to each other. These regions move independently, and they respond quickly by small electric motor actuation. They claim this might enable quick flight control in a cheaper morphing aircraft than the morphing wing program by DARPA [20].

2.1.3 Synthetic multifunctional materials

Synthetic multifunctional material (SMFM) is a structural material that contains at least one additional function besides load-bearing [31, 32]. DARPA initiated this research in 1998. The research project included powerfoil, which is as the airfoil and also as the power sources, for small unmanned air vehicle, carbon nanotube fibers, multifunctional electro-elastomers, tensegrity structures, and machine-augmented composites (MAC).

Matic [33] has categorized multifunctional materials into 3 classes:

- Added subsystems
- Co-located components
- Integrated materials

For multifunctional material design, he suggests starting from unifunctional design. Combinated unifunctional characteristics could be employed for multifunctional design.

In 2002 Hawkins proposed machine-augmented composites (MAC) [34]. In his concept, mechanical and physical properties are tailored by embedding simple machines into a matrix. Hawkins showed a composite material with mechanical properties augmented by embedded microscale simple machines. The Z-machine concept in Figure 1 is a passive shear-extension coupling element.

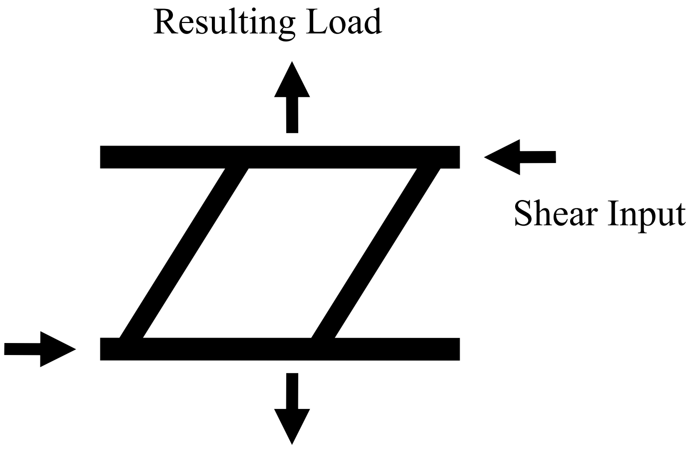

Figure 1. This schematic diagram shows a simple stress/strain conversion machine (after ref. [31]). This concept applied to the Z-machine.

Working within the MAC concept, Kim [35, 36] and McCutcheon [37-39] used the hourglass machine in Figure 2 to augment an elastomer matrix and the material showed good stiffness with excellent damping. Kim also suggested the active MAC for specific requirements. A bio-inspired active composite material might enhance performance by adding actuation to structural load carrying. Nastic materials that mimic the plant motion have been recently studied. However, we must first discuss actuators.

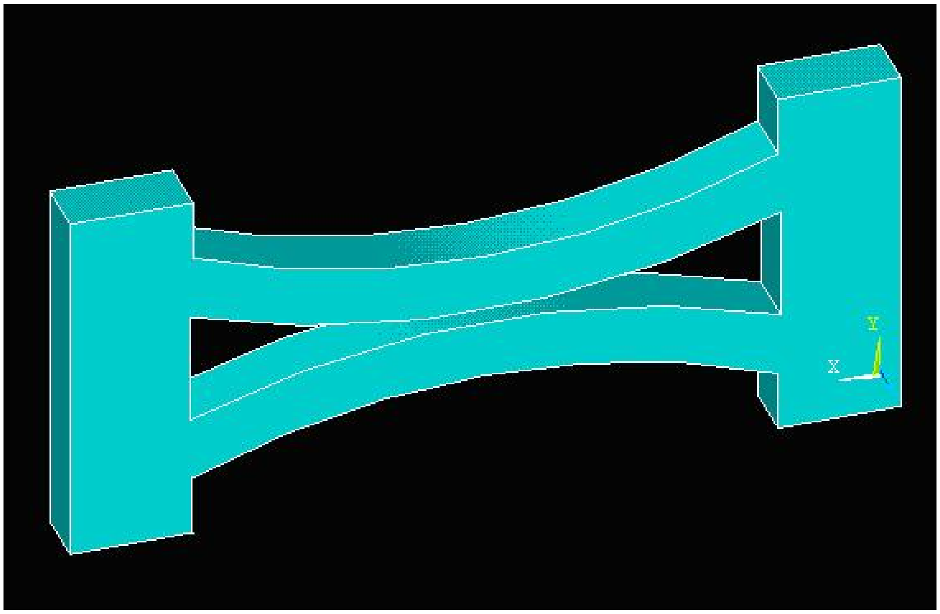

Figure 2. Hourglass (HG) machine for Finite Element Modeling

2.2 Actuating Materials

Actuators fall two categories[40]. The first category is natural actuators like human muscle. The second category is man-made actuators: pneumatic, piezoelectric, and shape memory alloy actuators.

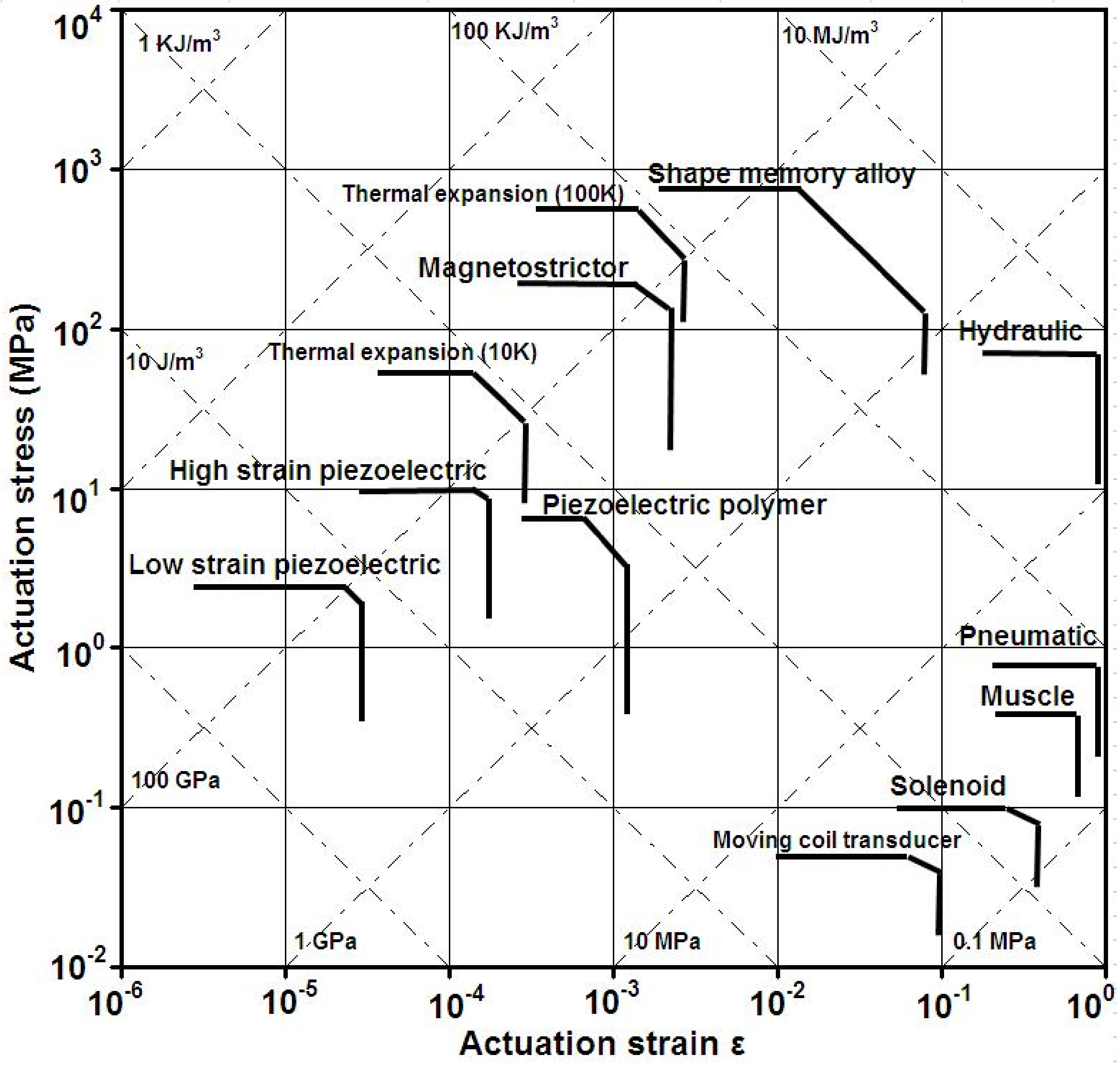

Figure 3. Actuator performances chart (after ref. [40]).
There are several measures of actuator performances. The actuation stress – actuation strain relationship appears here. This chart also presents work density because work density—the work per unit volume—can be found from the product actuation stress × actuation strain. Chapters V and VI present shear actuator performance.

Actuator performance characteristics are stress, strain (Figure 3), force, displacement, density, modulus, power, efficiency, and strain resolution. Understanding these characteristics is important when designing mechanical systems. With conventional actuator materials in mind, we can introduce nastic material.

2.3 Introduction to Nastic Material

Nastic movements are plant movements triggered by external stimulus. The direction is not determined by the stimulus; the plant's structure determines the direction [41]. Plant movement is classified by elastic and recoverable changes, i.e., tissue motion and permanent changes, i.e., growth. Nastic movement occurs elastically and is classified by stimulus and movement (for example, see Figure 4). Sometimes plants present large strains in milliseconds.

- Nyctinastic movements are slow, up and down movements that leaves make in a day/night cycle
- Seismonastic movements are sudden movements that respond to mechanical stimulation.

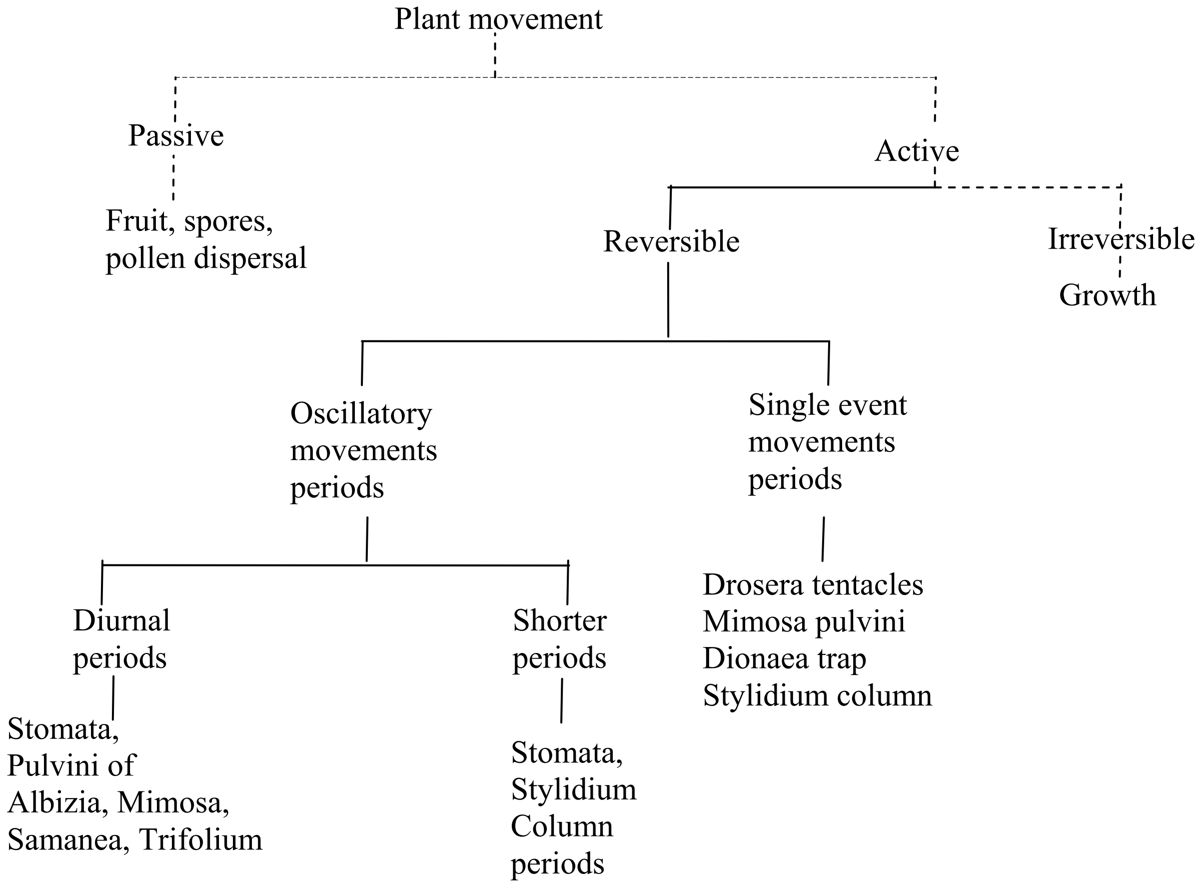

Figure 4. This classification scheme shows nastic movements in plants with continuous lines [42].

An early milestone in modern plant motion research is credited to C. Darwin [43] in 1880. Based on his investigation during a scientific journey to the Galapagos islands, he classified the plant movements into the form that we us now. Bose studied plant motion mechanisms in the 1920s [44-46]. He defined plant motion characteristics including structural shape changes by antagonistic volume changes, motile response by pressure variations in plant cells, and the pressure state controlled by transport through the cell wall.

In 1962, Selsam described and illustrated plant motion classes [47]. Recently, Forterre et al. [48] investigated fast trap-closure performed by “snap-buckling instability” in the Venus flytrap and found that the macroscopic closure mechanism is determined solely by the leaf ‘s bistable geometry.

In 2004, DARPA research initiatives about nastic materials are advancing a new active material class that is highly controllable and reversible material system that can generate 10 MPa in blocked stress and and 20% free strain [49].

A series of morphing wing studies by Cadogan et al. [21, 22, 24] considered nastic materials for high actuation forces in a lightweight material with continuous shape changes for the unmanned aerial vehicle described previously. Figure 5 shows the nastic cells are parallel tubes that can hold pressure. In the left picture within Figure 5, the tubes change their cross section from a collapsed flat sheet into a circle. Therefore, the pressure shortens the nastic cells and transmits forces. The forces rise with the internal pressure.

There is a force limit shown in right picture within Figure 5. When the cell is pressurized, it becomes circular. Consequently, the cell wall angle becomes perpendicular to the original sheet. Therefore, the generated force falls as the cell becomes fully inflated.

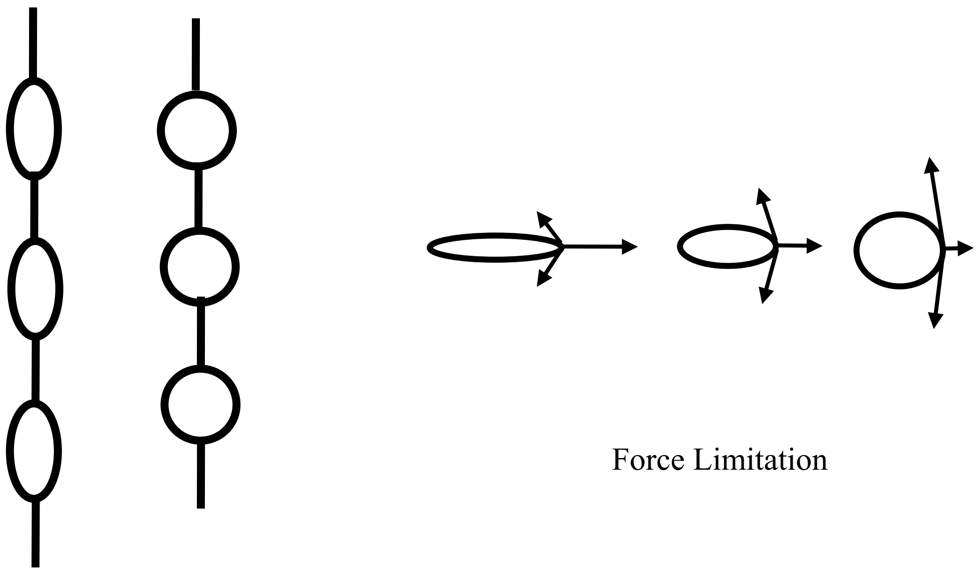

Foreshortening

Force Limitation

Figure 5. Cadogan et al.'s [22] nastic cell concept shortens a membrane by inflating repeated cells. The right image shows that the shape change limits the output force.

The authors did not employ nastic concepts because their nastic actuators did not satisfy their requirements, that is, response was too slow for quick flight control. Instead, they tested piezoelectric actuators, which have an operating frequency as high as KHz, for direction control [22]. In general, their nastic actuators might be okay for slower operating frequency applications. Finally, their inflated cells act only for tensile foreshortening.

More recently, Leo et al. investigated synthetic nastic structures as actuators [50-53] (2005~2007). The actuation is based upon an active transport protein. This material has ion-transport machines from living cells mounted in the walls of elastomeric microballoons. By adding Adenosine tri-phosphate (ATP), the actuator controls the fluid flow through the protein pump. An electric signal opens ion channels to initiate the actuation. Fluids move into the sphere, increase the osmotic pressure, and enable actuation.

2.4 Theoretical Backgrounds for Elastomer Tests

This section explains three typical types of elastomer tests [54-56], starts with simple tensile test, planar tension-pure shear test, and finally, equi-biaxial extension test.

2.4.1 Simple tensile test

The unaixal tension that defined by ASTM puts specimens in plane stress.

Hyperelastic models define deformation as stretch. The stretch λ_i along any principle axis, where i=1,2,3, defined by this equation:

$$\lambda_i = 1 + \varepsilon_i \qquad (1)$$

where ε_i is the principal strain.

One restriction is defined by this quation:

$$\lambda_1 \lambda_2 \lambda_3 = 1 \qquad (2)$$

when the material is incompressible.

For uniaxial stretch caused by a load that caused strain ε_u

$$\lambda_1 = \lambda_u = 1 + \varepsilon_u \qquad (3)$$

and,

$$\lambda_2 = \lambda_3 = 1/\sqrt{\lambda_u} \qquad (4)$$

under uniaxial tension of stretches where λ_u is the stretch along the uniaxial loading direction and ε_u is the nominal tensile strain.

2.4.2 Planar tension-pure shear test

For this test, plane strain condition is imposed, and high aspect ratios (large width to length) specimen is used.

The principal stretches λ_i (i=1,2,3) are (corresponding to length, width and thickness respectively) (with incompressible material)

$$\lambda_1 = \lambda_s, \lambda_2 = 1, \text{and } \lambda_3 = 1/\lambda_s \qquad (5)$$

where λ_s is the stretch in the loading direction.

This can be regarded as the 'pure shear test' because the logarithmic strains are corresponds to the state of pure shear at 45° to the loading direction

$$\varepsilon_1 = \ln\lambda_1 = -\ln\lambda_3 = -\varepsilon_3, \text{ and } \varepsilon_2 = -\ln\lambda_2 = 0 \qquad (6)$$

2.4.3 Equi-biaxial extension test

Equi-biaxial tension tests require a stress state with equal tensile stresses along two orthogonal directions.

The deformation mode with incompressibility:

$$\lambda_1 = \lambda_2 = \lambda_b \text{, and } \lambda_3 = 1/\lambda_b^2 \tag{7}$$

where λ_b is the stretch in the perpendicular loading direction.

$$\varepsilon_b = \lambda_b - 1 \text{ : nominal strain} \tag{8}$$

2.4.4 Uniaxial compression-biaxial extension test

Uniaxial compression test can be a good option to perform when the equi-biaxial test machine is not available.

The uniaxial compression test [57, 58] deformation state is;

$$\lambda_2 = \lambda = L/L_0,\ \lambda_1 = \lambda_3 = \sqrt{A/A_0} \tag{9}$$

And the stress state;

$$\sigma_2 = \sigma = P/A_0,\ \sigma_1 = \sigma_3 = 0 \tag{10}$$

We can get the compression strains and stresses [58] from the biaxial strains and biaxial stresses;

$$\sigma_c = \sigma_b(1+\varepsilon_b)^3,\ \varepsilon_c = 1/(\varepsilon_b+1)^2 - 1 \tag{11}$$

In the same manner, the biaxial strains and stresses are derived from compression strains and stresses using above relationships;

$$\sigma_b = \frac{\sigma_c}{(1+\varepsilon_b)^3},\ \varepsilon_b = \sqrt{\frac{1}{1+\varepsilon_c}} - 1 \tag{12}$$

2.5 Failure Criteria of Pressurized Elastomers

This work has merit only if a good failure criteria provides an limit for the response. This section presents the failure criteria used here.

2.5.1 Failure/Fracture modes of rubber

Rubber and bonded rubber blocks could fail by the following two modes, when the large loads imposed ([59]): (1) horizontal cracks near the bonded edge (Figure 6a), and (2) horizontal cracks in the free surface (Figure 6b).

2.5.2 Failure criteria for free strain case; internal rupture

Failure by internal cracking will occur when the local hydrostatic pressure reaches a critical negative value, which about -0.75 E [60]. Under this triaxial tension, any small cavity will rapidly increase. The criterion for internal rupture is [61]

$$-P_{\max} > \frac{3}{4}E \qquad (13)$$

Where $-P_{\max}$ is the maximum negative pressure developed in the block.

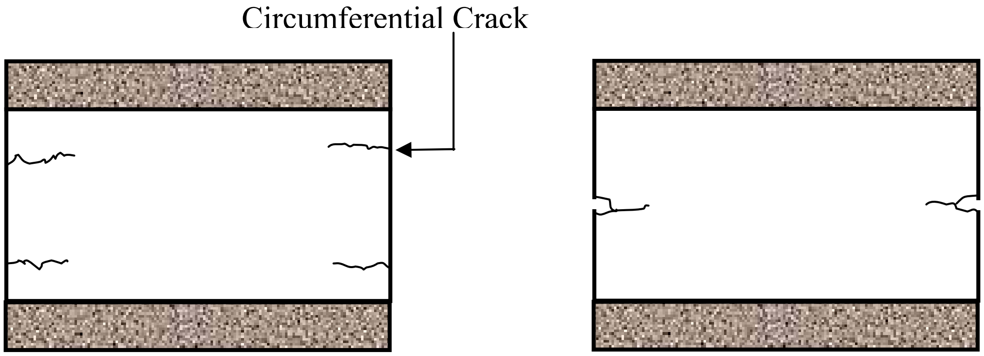

(a) Tearing near the bonded edges

(b) Splitting open of the free surface

Figure 6. For rubber, two fracture modes are possible under static compression (after [59]).

2.5.3 Failure criteria for blocked stress case

For the (incompressible) rubber block under compression [59], maximum shear stress near the bonded edges has to be less than G. In other words, maximum shear deformation cannot be more than 100%.

2.6 Introduction to Hyperelasticity

Reversible, large strain performance is available with two materials: biological tissues and elastomers. For the synthetic nastic material studies here, elastomers are a crucial component that enables large strain actuation. This section presents the theoretical background for modeling hyperelastic materials and the section shows what properties must be measured by experiment.

2.6.1 Background for large deformation theory

For small deformation elasticity the Cauchy stress tensor, which is force/deformed area, is used as the stress measure. However, under large deformation it is difficult to determine the deformed configuration's area. We need a new stress measure for large deformation [62].

The 1st Piola-Kirchoff stress is defined as the force divided by the undeformed area. However, the 1st Piola-Kirchoff stress tensor is not symmetric, and when it and the Green-

Lagrangian strain tensor are multiplied, the product is not consistent with the strain energy density with Cauchy stress with small deformation strain tensor. This makes the 1st Piola-Kirchoff stress unsuitable for numerical analysis. The 2nd Piola-Kirchoff stress tensor is the total force in the undeformed configuration divided by the area in the undeformed configuration. This stress tensor is appropriate for energy density because the strain energy density from 2nd Piola-Kirchoff stress and Green-Lagrangian strain equals the strain energy density from Cauchy stress and small deformation strain tensor.

For hyperelastic materials, stretch is a deformation measure in many cases as well as strain. Stretch is deformed length/original length ratio. Therefore, when there is no deformation, the stretch is unity and the strain is zero.

2.6.2 Theory of hyperelasticity

This section presents a brief overview for hyperelastic model development. The subsections that follow provide details about the models.

Hyperelastic material models are characterized by their strain- energy density functions. Many authors have analyzed hyperelastic or rubberlike materials since the early 20th century [63]. Mooney's [64] (1940) and Rivlin's [65] (1948) work influenced almost all later research. Mooney proposed a two-term phenomenological model for large elastic deformation theory, and Rivlin developed his theory based on Mooney's work. Later, a significant development came from Valanis and Landel [66] (1967). They changed the strain energy function to separable terms regarding the principal directions. Their model influenced Ogden, whose model is widely employed in this area [67, 68] (1972). These theories express the elastic strain energy with a form dictated by continuum mechanics for an initially isotropic, incompressible, hyperelastic solid [69]. Table 1 lists available hyperelastic models.

Oden contributed to early finite element analysis and computation methods in engineering in many areas including nonlinear sold mechanics and fluid mechanics. He also applied hyperelasticity theory to finite element analysis with important remarks about implementing hyperelastic materials incompressibility numerically [70, 71] (1972 and 1982). After him, many researchers worked on developing finite element formulations for incompressible hyperelastic models [72-77].

Simo et al. [78-81] published excellent work for applying hyperelasticity based on continuum mechanics to finite element analysis. Current commercial FEA software, for example, ANSYS®, refer to Simo's and other authors' work described above.

Next, we present details about each model and define the parameters that appear in Table 1.

Table 1. Hyperelastic model summary [57]

Model name	Strain energy functions	Descriptions
Neo-Hookean	$W = C_{10}(I_1 - 3)$	Good up to 40% strain in uniaxial tension, 90% strain in simple shear
Mooney	$W = C_{10}(I_1 - 3) + C_{01}(I_2 - 3)$	Good up to 100% tensile test. Not good at large strains
Three term Mooney-Rivlin	$W = C_{10}(I_1 - 3) + C_{01}(I_2 - 3) + C_{11}(I_1 - 3)(I_2 - 3)$	Good for both filled and unfilled rubbers
Yeoh	$W = C_{10}(I_1 - 3) + C_{20}(I_1 - 3)^2 + C_{30}(I_1 - 3)^2$	Needs to be careful for low strains
Ogden	$W = \sum_{n=1}^{N} \frac{\mu_n}{\alpha_n} J^{\frac{-\alpha_n}{3}} (\lambda_1^{\alpha_n} + \lambda_2^{\alpha_n} + \lambda_3^{\alpha_n} - 3) + 4.5K(J^{-1/3} - 1)^2$ J; Jacobian measuring dilatancy - determinant of deformation gradient f	Good up to 700% strain in simple tension

2.6.2.1 The Neo-Hookean Model

Generally the strain energy functions are strain invariant functions in stretch terms.

$$I_1 = \lambda_1^2 + \lambda_2^2 + \lambda_3^2 \tag{14}$$

$$I_2 = \lambda_1^2\lambda_2^2 + \lambda_2^2\lambda_3^2 + \lambda_3^2\lambda_1^2 \tag{15}$$

$$I_3 = \lambda_1^2\lambda_2^2\lambda_3^2 \tag{16}$$

The simplest hyperelastic form, the Neo-Hookean model, has first and second strain invariants, I_1 and I_2 (Figure 7~Figure 9). The incompressibility constraint forces the third strain invariant $I_3=1$ so that volume is conserved.

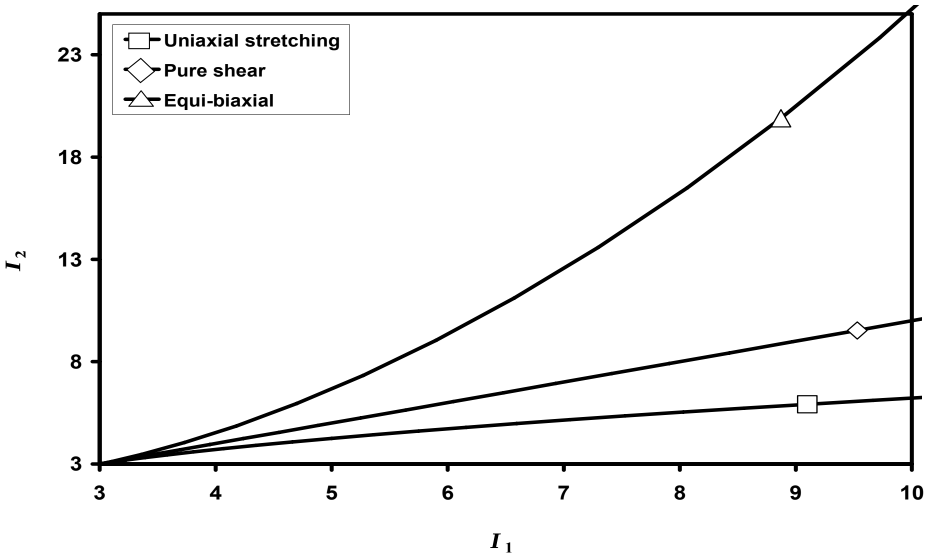

Figure 7. For incompressible elastomers, possible deformations are in the region between uniaxial stretching-marked with a square-and equi-biaxial-marked with a triangle-as I_1 and I_2 functions (after ref. [82]).

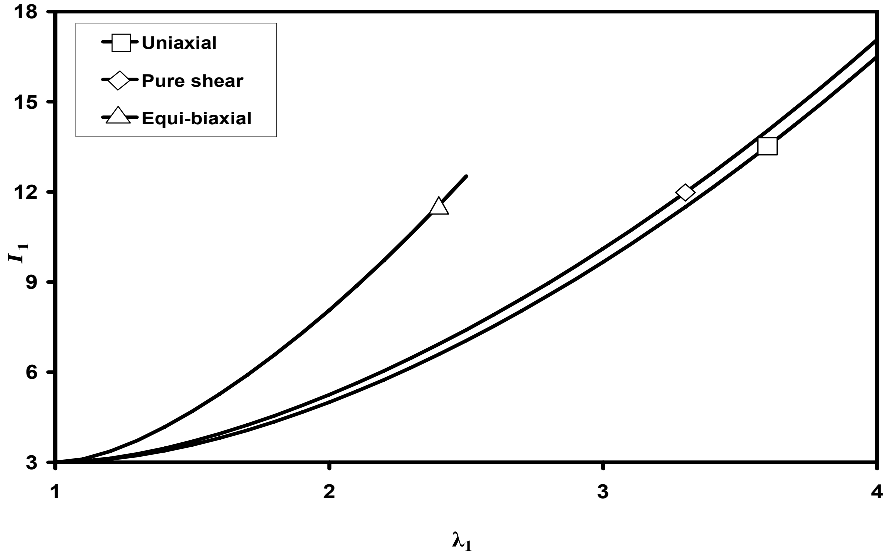

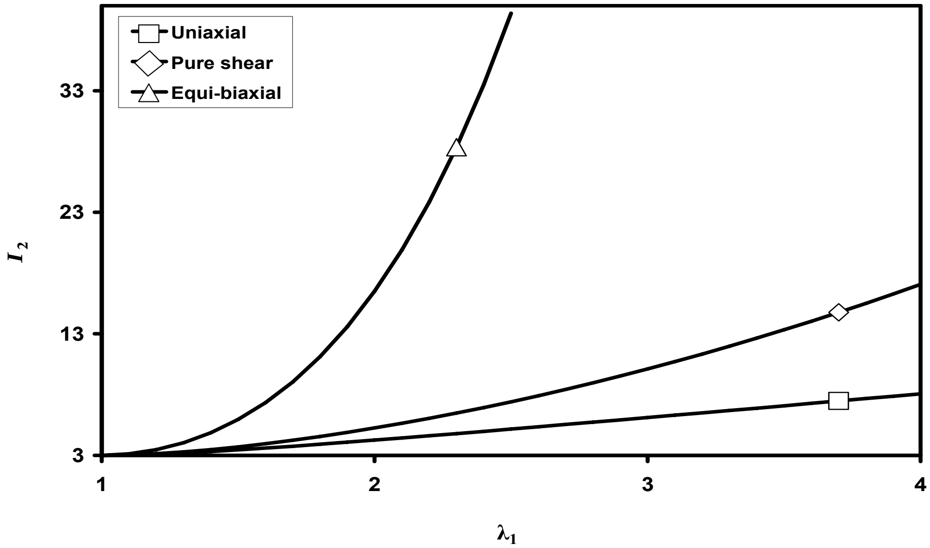

Figure 8. For pure shear, I_1 and I_2 are identical because $\lambda_2 = 1$ in this case.

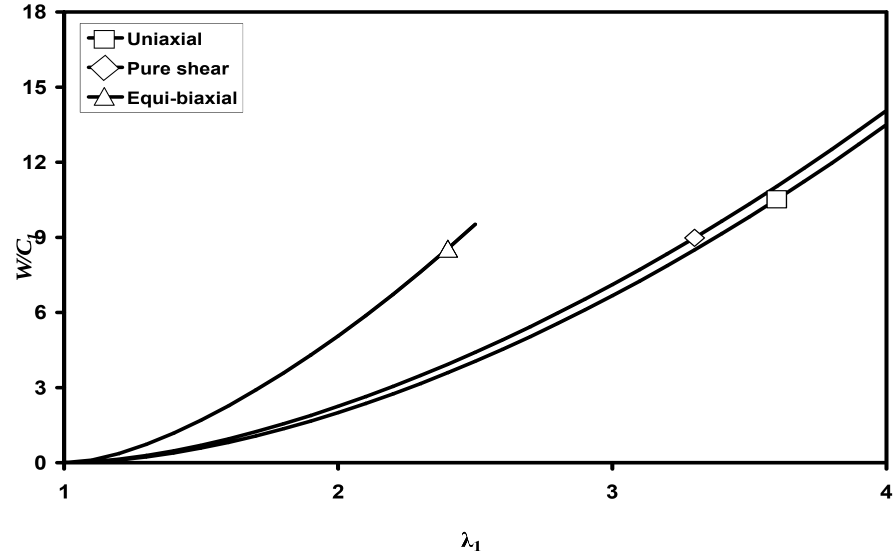

Figure 9. This plot shows that the neo-Hookean model strain energy density contains only first strain invariant terms.

Neo-Hookean model is

$$W = C_1(I_1 - 3) \qquad (17)$$

where C_1 is constant shear modulus [57].

2.6.2.2 (2-term) Mooney Model

The Mooney model – also called as Mooney-Rivlin model – is

$$W = C_1(I_1 - 3) + C_2(I_2 - 3) \qquad (18)$$

From the ref. [83], for a equi-biaxial extension (equivalent to uniaxial compression),

$$\lambda_2^2 = \lambda_3^2 = 1/\lambda_1 \tag{19}$$

so

$$W = C_1(\lambda_1^2 + 2/\lambda_1 - 3) + C_2(1/\lambda_1^2 + 2\lambda_1 - 3) \tag{20}$$

Differentiating W with respect to λ_1 gives (and dropping subscript)

$$f = 2(\lambda - 1/\lambda^2)(C_1 + C_2\lambda) \tag{21}$$

where f is the force per unit unstrained area.

Then,

$$t = 2(\lambda^2 - 1/\lambda)(C_1 + C_2\lambda) \tag{22}$$

where t is corresponding true stress

With this approach, several authors have reported the inconsistency between Mooney's model and experimental data.

For example, Treloar [83] claims that Rivlin and Saunders ref. [84] is inconsistent. He claims that, for simple extension, Mooney's model fits well with experimental data with the ratio of C_2/C_1. However, for uniaxial compression data, which corresponds to equi-biaxial extension, $C_2 \cong 0$. From this inconsistency, Mooney's model does not represent strain density function for a general elastomer property adequately, and the overpredicted simple extension curve and misfit biaxial stress-strain relation have been reported [85].

2.6.2.3 Third or Higher Order Ogden Model

This Ogden model is

$$W=\sum_{n=1}^{N}\frac{\mu_n}{\alpha_n}J^{\frac{-\alpha_n}{3}}(\lambda_1^{\alpha_n}+\lambda_2^{\alpha_n}+\lambda_3^{\alpha_n}-3)+4.5K(J^{-1/3}-1)^2 \qquad (23)$$

More complicated versions, Valanis and Landel model are developed, and Ogden model has been derived based on this model. As the matrix elastomer is highly nonlinear and goes to large deformation more than 600%, the Ogden model has been chosen and used in this research.

2.6.3 Stress softening and Mullins effect

Under repeated tensile strain, many polymers exhibit a reduction in stress after the initial extension; this is the Mullins Effect [86-89]. For rubbery material elasticity it is important to know the Mullins effect; almost 60 years have passed since Mullins' work in 1947 [86]. The Mullins effect is "Phenomenon observed in elastomeric polymers where the equilibrium stress-strain response softens with the strain history" [90]. The Mullin's effect has these features:

- The cycled material has the stress-strain response of virgin material at strains greater than the previous maximum strain
- The cycled material has a more compliant response at strains smaller than the

previous maximum strain

When the Mullins effect occurs, the microstructure beaks down with increasing deformation, but the initial structure cannot be rebuilt.

CHAPTER III

MATERIAL PREPARATION

3.1 Fabrication of Specimen from Soft Polyurethane

Baseline design data needed to complete the analysis came from soft polyurethane specimens tested in simple and planar tension. The next sections present the fabrication method for these specimens.

3.1.1 Simple tensile test

The specimen and test procedure followed specification ASTM D638-03. Dog-bone specimens were prepared from soft polyurethane. The mini-CNC machine in Figure 10 cut a mold in Figure 11 from machinable modeling wax. Figure 12 shows a D638 specimen. The specimens were used for the single extension to failure test and for cyclic testing.

The soft polyurethane (SPU) is a commercial product called FMSC 1035® from Freeman Manufacturing and Supply Company (FMSC). Freeman sells a one-gallon kit including two ½ gallon containers. The constituents for each container are

- Part A: polyurethane polymer, Bis(2-ethylhexyl) phthalate

- Part B: nonhazardous polyol, diethyl toluene diamine, di(methylthio) toluene diamine

When mixed in a 1:1 ratio-by volume or weight-the SPU is a pourable, low viscosity fluid. FMSC 1035 gels in 30 minutes at room temperature 22.2°C (72°F); the SPU must fill any mold before it gels. Demold time is 16 hours at room temperature.

When fully cured, the dog-bone specimen is ready for the tensile test.

Figure 10. Roland PNC-300$^{®}$ mini-CNC machine.
This machine cut the wax mold for specimens.

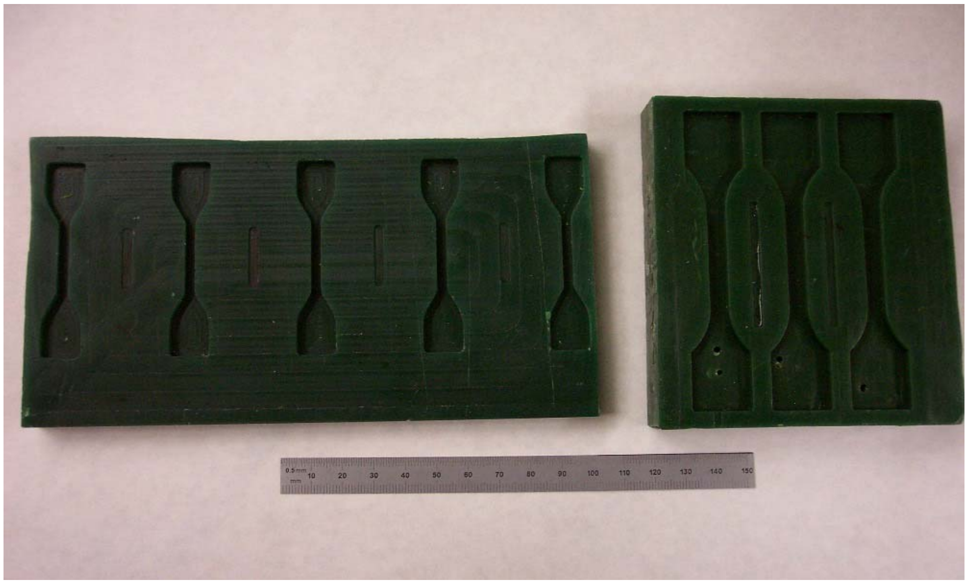

Figure 11. Big and small mold made ASTM D638 specimens.

Figure 12. A dog-bone shaped specimen used for tensile test.

3.1.2 Planar tension test

The equations presented in section 2.5.2 show that a planar tension specimen produces shear deformation in an elastomer. Figure 13 and Figure 14 show the wax mold and originally designed specimen, respectively. The mold for pure shear test specimen is also made from mini-CNC machine. FMSC 1035® resin is also used for this specimen.

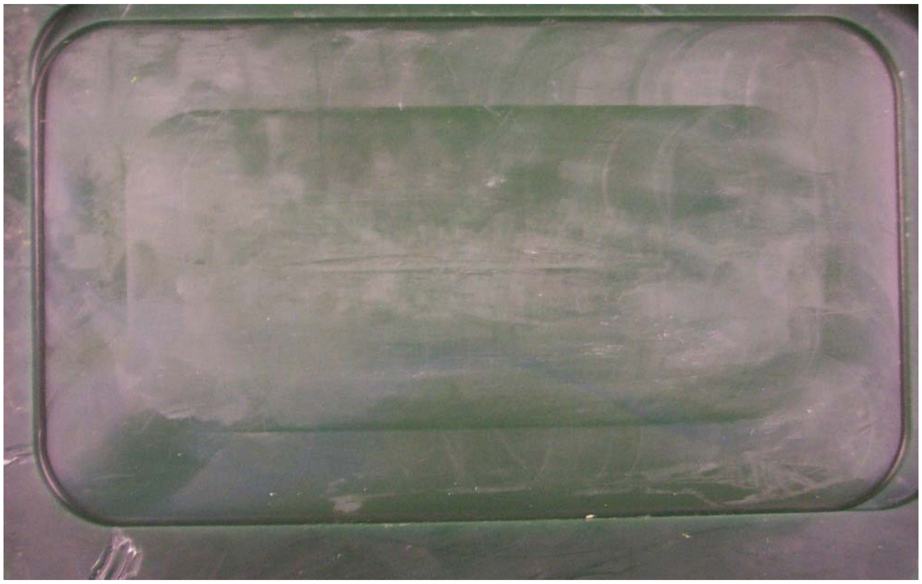

Figure 13. Wax mold made the planar tension specimen.

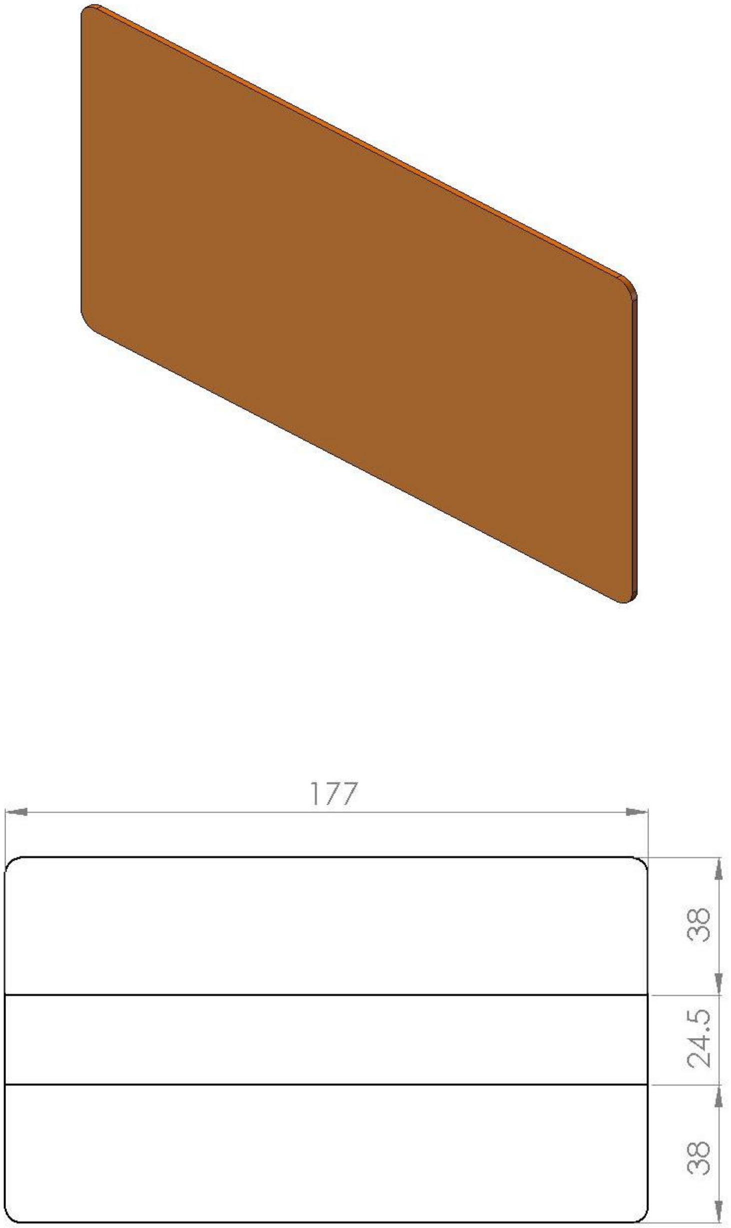

Figure 14. Planar tension-Pure shear test specimen is wider than it is high. The design dimensions are 177 X 100.5 X 1.6mm including initial grip separation 24.5mm.

3.2 Design and Fabrication of Lens Element

Designing a material to deform in simple shear is a challenge. This section presents a first-order method for designing them based on simple shear deformation. First, we look at material response when driven to shear by external forces. At the material element boundary, the displacements follow solid mechanics solutions. Our objective is to create an active material that has simple shear displacement at the boundary for each active material element. In an assembly, these active cells might produce a material that has homogenized response that is simple shear while the interior displacements are what is necessary to move the element boundary and apply forces to the exterior.

The shear actuator uses a lens-shaped element, embedded inside a rubber matrix. The lens element contains a balloon within a Kevlar fabric sleeve. Since this balloon-Kevlar element is lenticular, we start with first-order geometric equation for a lens.

3.2.1 First-order strain equations for a lens-shaped element

As shown in Figure 15, a material in equal biaxial expansion/contraction is equivalent to shear condition when 2θ equals 90° in Mohr's circle. Therefore, the following derivation must find the best initial and final aspect ratio for the lens to achieve pure shear when pressurized. Figure 16 explains the concept of shear actuator.

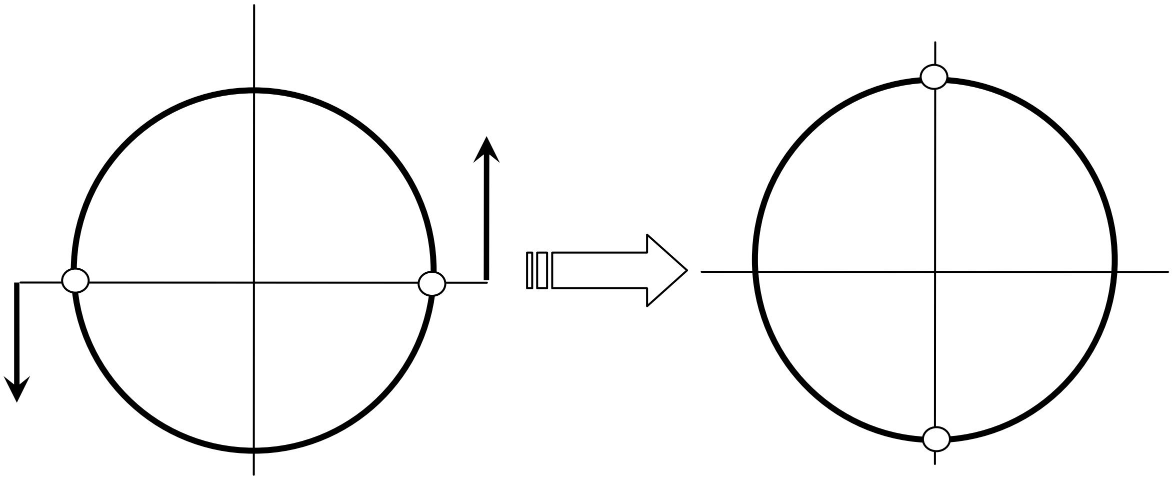

Figure 15. The two-dimensional Mohr's circle for strain shows that pure expansion/contraction-the open circle points in left image-is equivalent to pure shear, which appears at the open circle points in the right image.

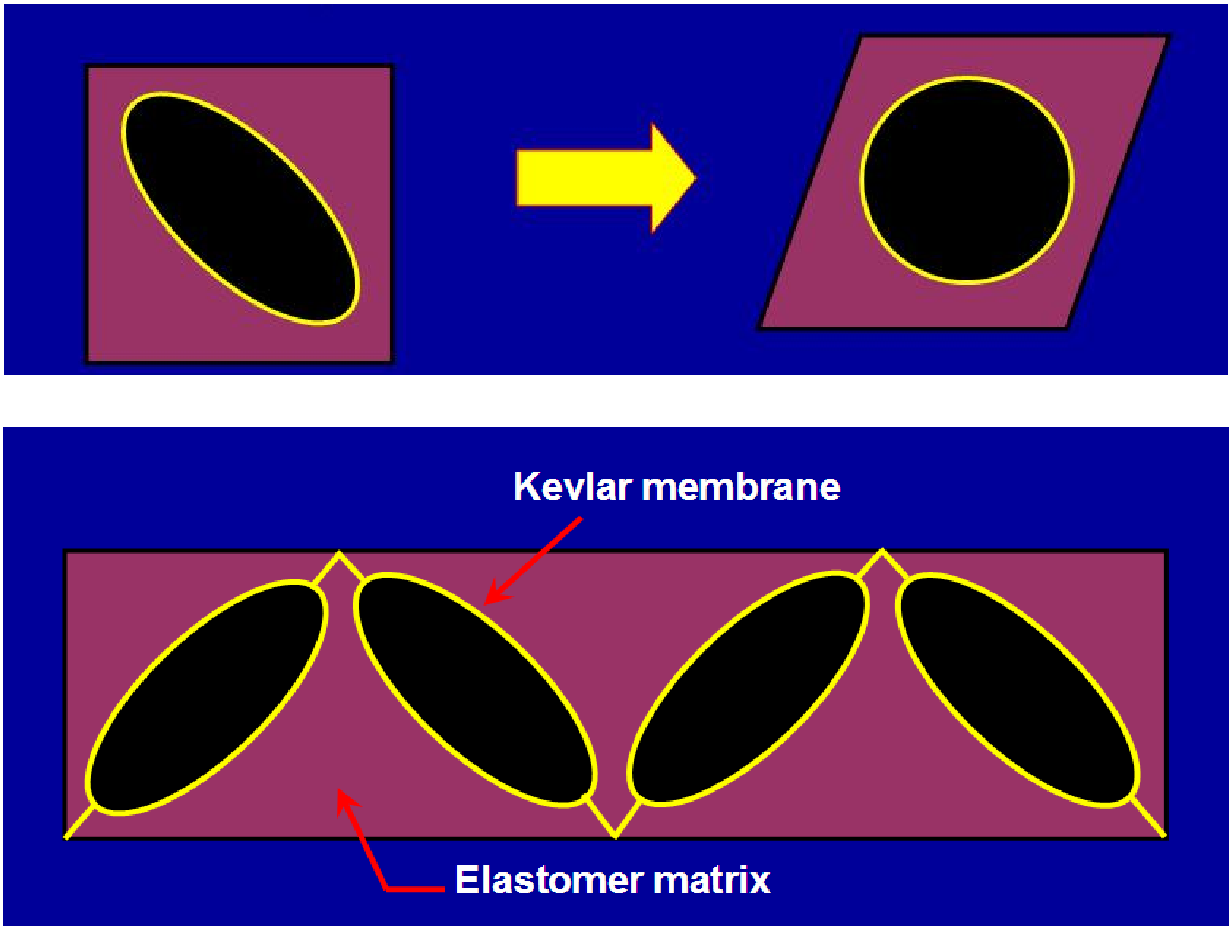

Figure 16. Nastic cells can be arranged as a single-acting shear actuator (top), or as an array the shears left or right as needed (bottom). The lens element is 45° to the shear direction and embedded in the elastomer matrix. The concept claims that the lens element actuator approaches a full circle when pressurized and causes shear deformation.

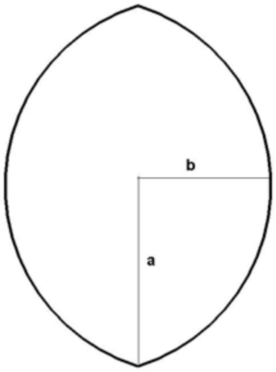

.

Figure 17. This picture shows the geometry of a lens.
A lens is characterized by the length of long axis ‘a’ and short axis ‘b’ as in the picture.

3.2.2 Aspect ratio for best shear deformation

Figure 17 shows the geometry of a lens. Author [91] discusses lens analysis and presents the circle-circle intersection equations

$$2a = \frac{1}{d}\sqrt{4d^2R^2 - (d^2 - r^2 + R^2)^2} \qquad (24)$$

In our case, $r = R$, therefore

$$2a = \frac{1}{d}\sqrt{4d^2R^2 - d^4} = \frac{1}{d}\sqrt{d^2(4R^2 - d^2)} \qquad (25)$$

So,

$$a = \frac{1}{2}\sqrt{4R^2 - d^2} \qquad (26)$$

Where,

$$R = \frac{a^2 + b^2}{2b}, \; d = 2\sqrt{R^2 - a^2} \tag{27}$$

And,

$$b = R - \sqrt{R^2 - a^2} = R - \frac{d}{2} \tag{28}$$

From simple circle-arc relations, the total lens circumference c is

$$c = 2\pi r = 4R\tan^{-1}(\frac{a}{R-b}) \tag{29}$$

Thus, the radius of the circle that has same circumference as a given lens is

$$r = \frac{2R}{\pi}\tan^{-1}(\frac{a}{R-b}) \tag{30}$$

If we set r=1.0, then

$$a = (R-b)\tan(\frac{\pi}{2R}) \tag{31}$$

Now, deleting *a* and *d* from above relationships gives

$$\frac{0.5\sqrt{8Rb - 4b^2}}{R-b} - \tan(\frac{\pi}{2R}) = 0 \tag{32}$$

Also, the lens area *A* is

$$A = 2R^2\sin^{-1}(\frac{a}{R}) - 2a(R-b) \tag{33}$$

For best shear deformation, the aspect ratio must be 1.381 as Figure 18 and Figure 19 show. Figure 20 shows strain ratio variation due to b dimension change.

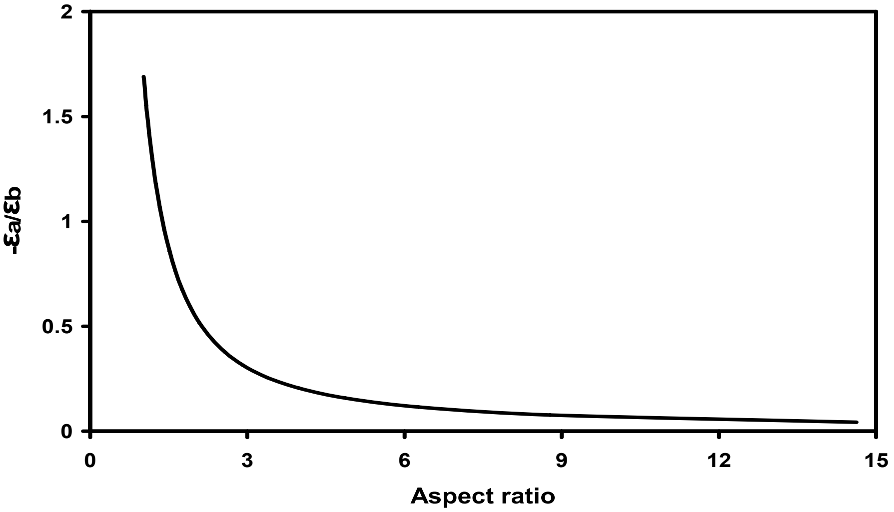

Figure 18. Strain ratio with various aspect ratio shows best shear deformation occurs when the lens aspect ratio—long axis length divided by short axis length—is 1.3817.

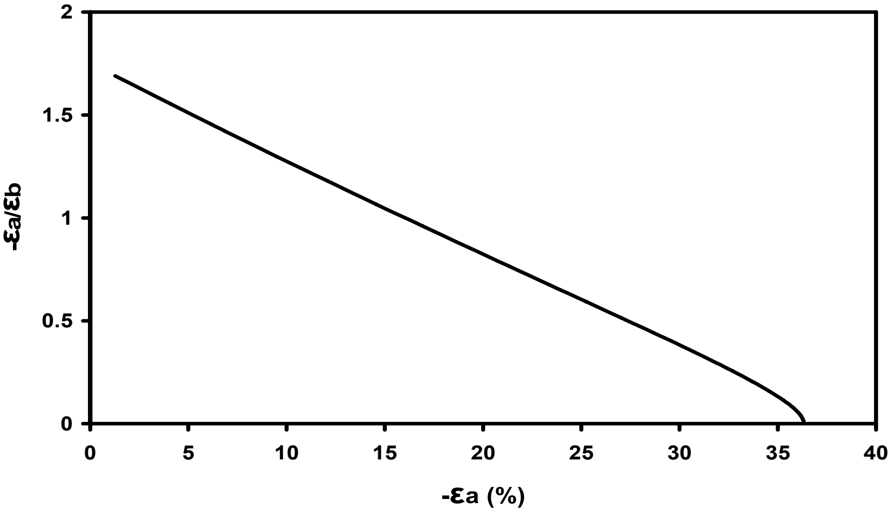

Figure 19. Strain ratio with given lens shape strains.
It shows, when 16.03% strain, pure shear will take place.

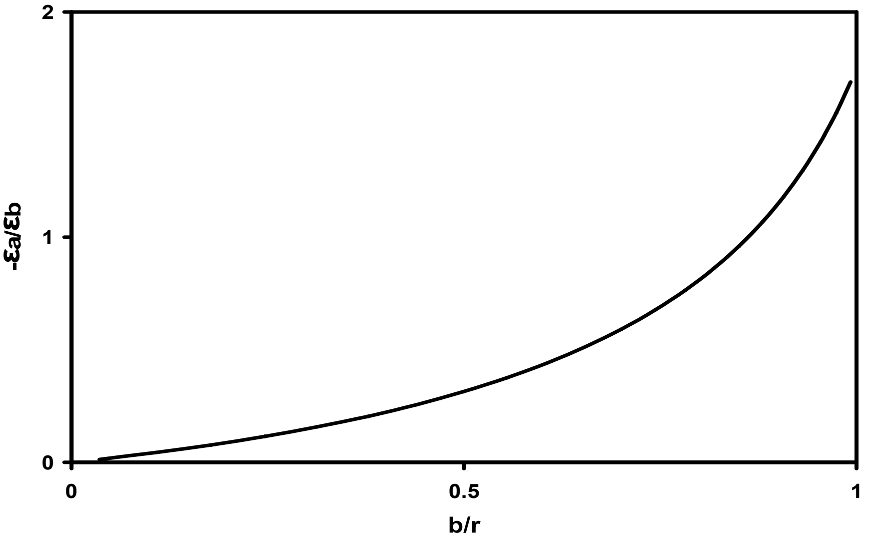

Figure 20. Strain ratio varies when b approached a full circle.

3.2.3 Kevlar fabric lens element

Kevlar fabric ontained from Fiberglast froms the structural base for the lens-element actuator. A toy balloon is inside the fabric. A single-use aluminum crimp clamp connects the toy ballon to a nylon pressure-supply hose (see Figure 21 and Figure 22).

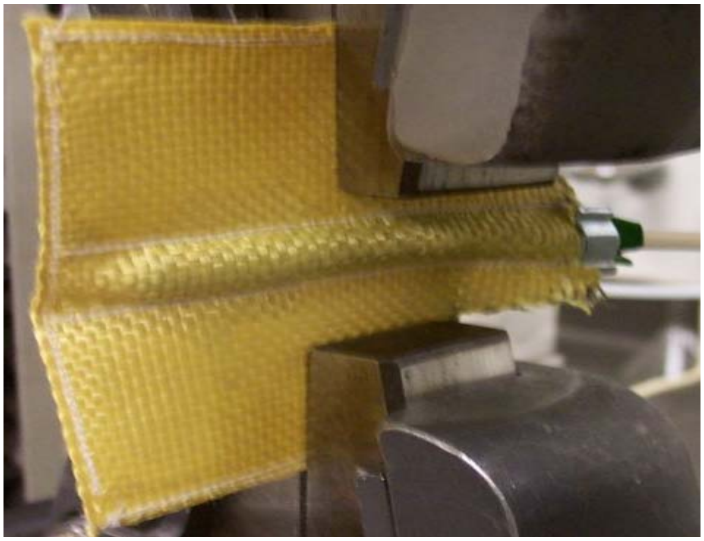

Figure 21. Lens element made from Kevlar fabric

3.3 Fabrication of Shear Actuator

To make shear actuator structure flexible, polyurethane or any other similar flexible material can be applied, and this study used a soft polyurethane matrix material (Freeman Company manufacturing Repro polyurethane 1035 resin system) and Kevlar fabric containing a balloon inside as a lens element.

Figure 22. Portable sewing machine used for Kevlar fabric

The Kevlar fabric element Young’s modulus is 100GPa, Poisson’s ratio 0.35.

With the 1035 resin system, specimens can be made quickly at room temperature without any heat source. The first step in the fabrication process is making a mold with a precise CNC machine (Roland DGA Company Model PNC 300). After this process, pour pre-mixed 1035 resin into the mold and cure at room temperature.

3.3.1 Mold design and CNC machining

The mold is designed by using commercial CAD software SolidWorks®. (see Figure 23~Figure 27). The mold specifications are as follows

- Target shape of lens; Long axis of lens a = 6mm, b = 3.73mm
- Area of lens = 64.06624mm^2
- Volume fraction = 44.5 % (with 12mm X 12mm matrix)

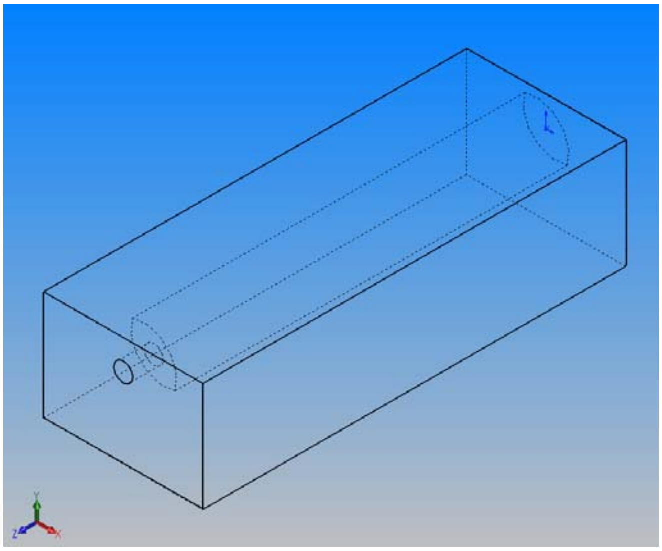

Figure 23. Rotated lens-Block model showing cavity

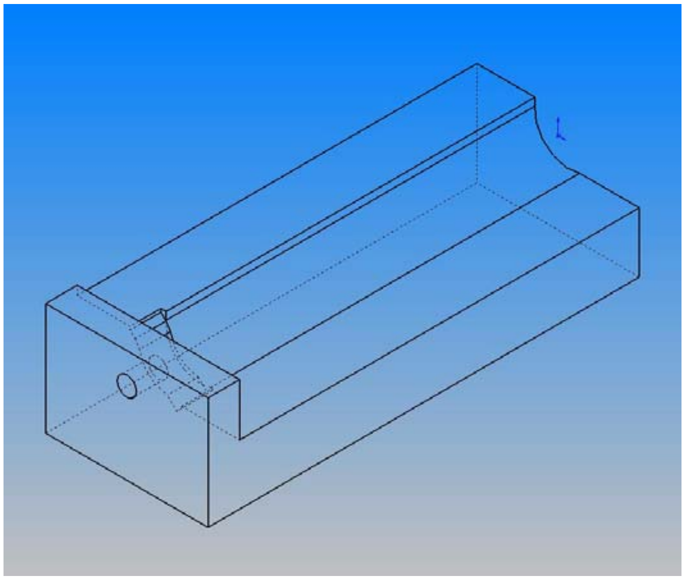

Figure 24. Rotated lens-Block model.
The features are cut-excluded in sequence.

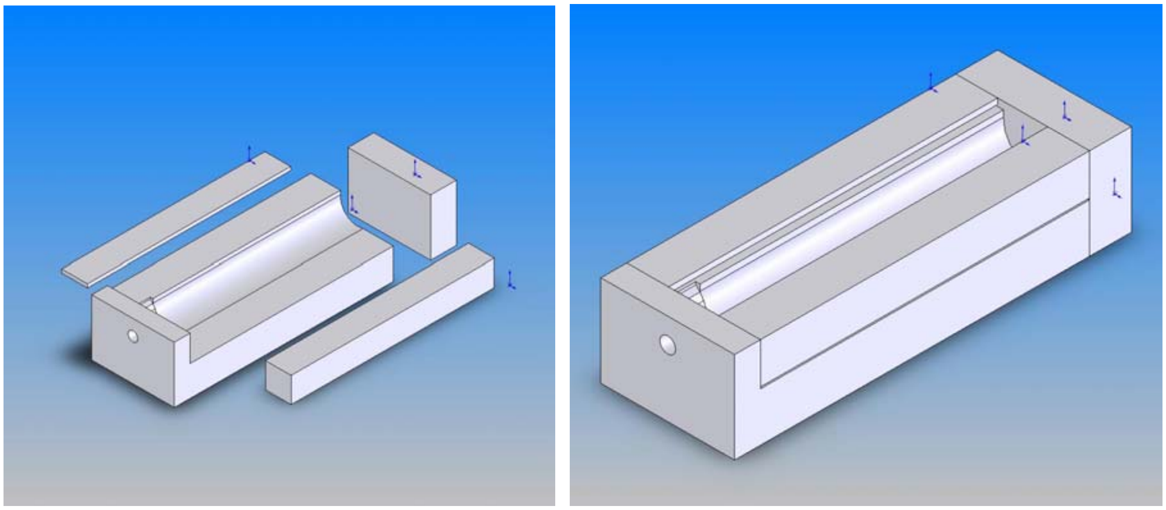

Figure 25. Assembly for the mold (left) and final assembly for the actuator fabrication (right)

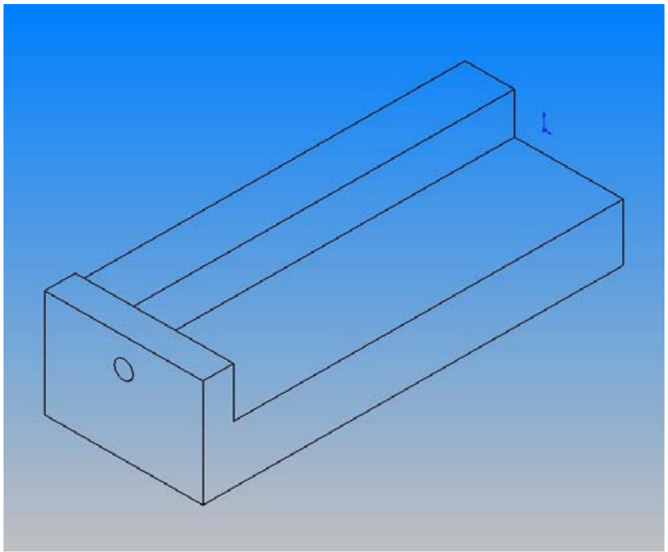

Figure 26. The base mold for 2nd part. Kevlar fabric element is rotated.

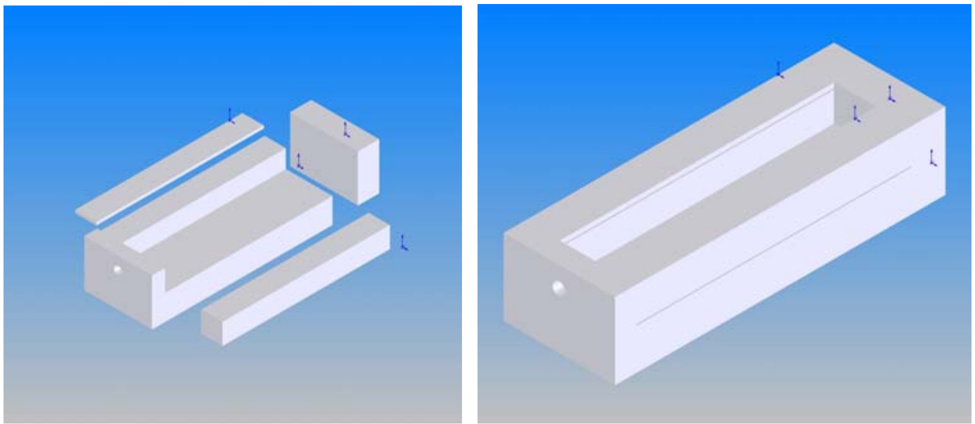

Figure 27. Assembly for the 2nd mold

Figure 28~Figure 31 show the wax mold for shear actuator. The 1st and 2nd mold were made separately as described above.

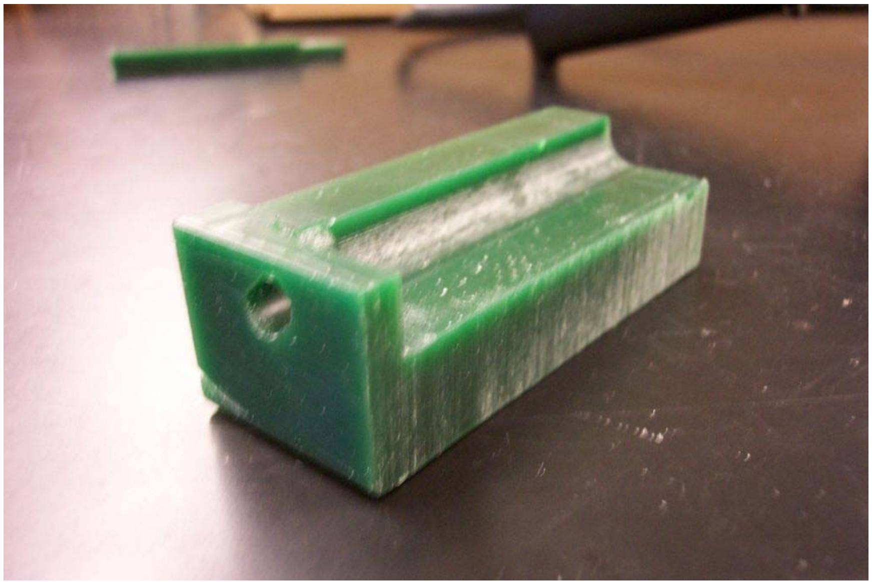

Figure 28. 1st mold for lens-shear actuator.

Figure 29. The top blocks and back blocks applied.

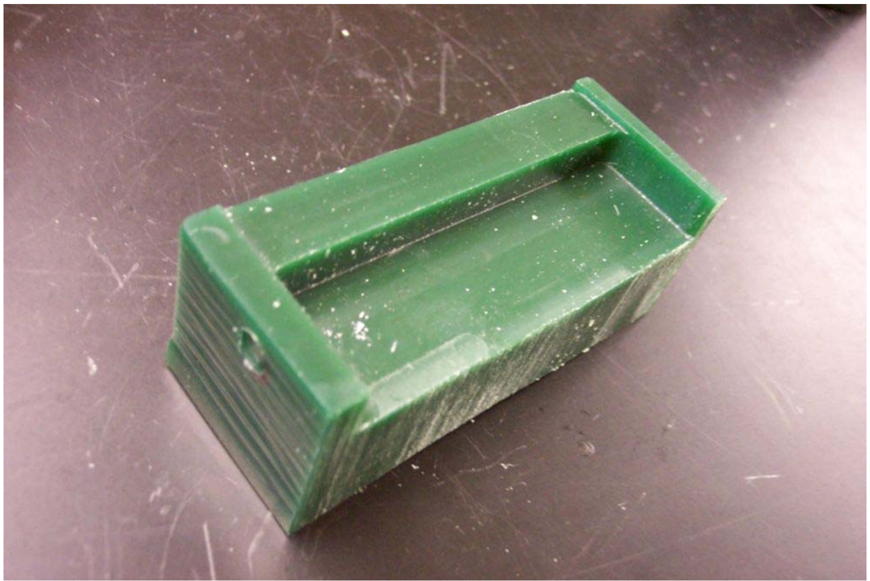

Figure 30. This is 2nd mold for shear actuator.

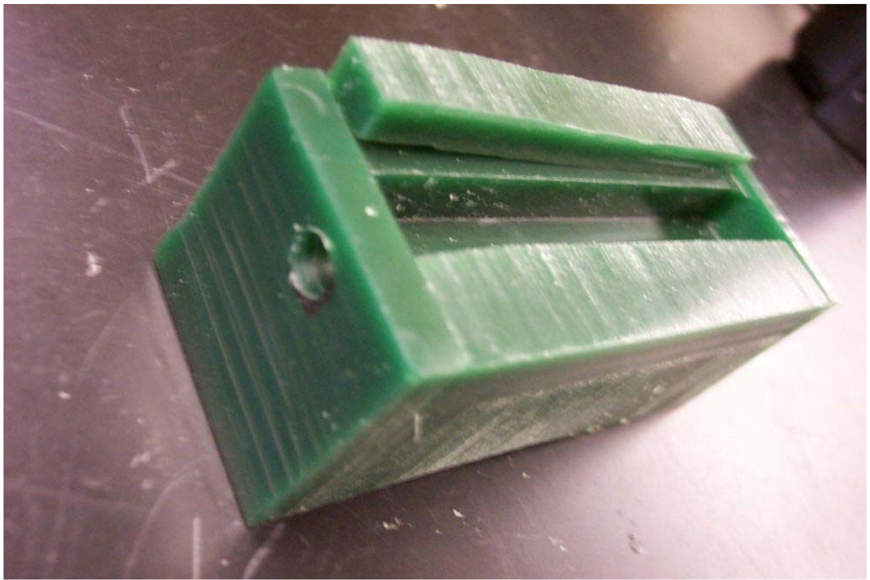

Figure 31. Top and back blocks applied to 2nd mold.

The shear actuator is fabricated as in Figure 32 and Figure 33.

Figure 32. The mold and Kevlar fabric element set up to apply the soft polyurethane resin.

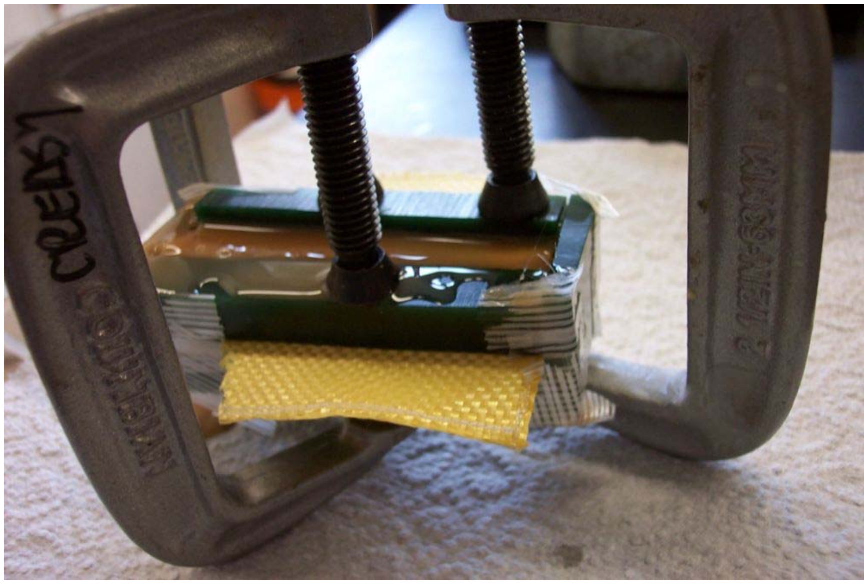

Figure 33. Actuator is in curing process with soft polyurethane resin.
A clamping device put forces to make sure the parts in appropriate place during curing.

Fully constructed shear actuator (Figure 34) is bonded to the aluminum block as in Figure 35.

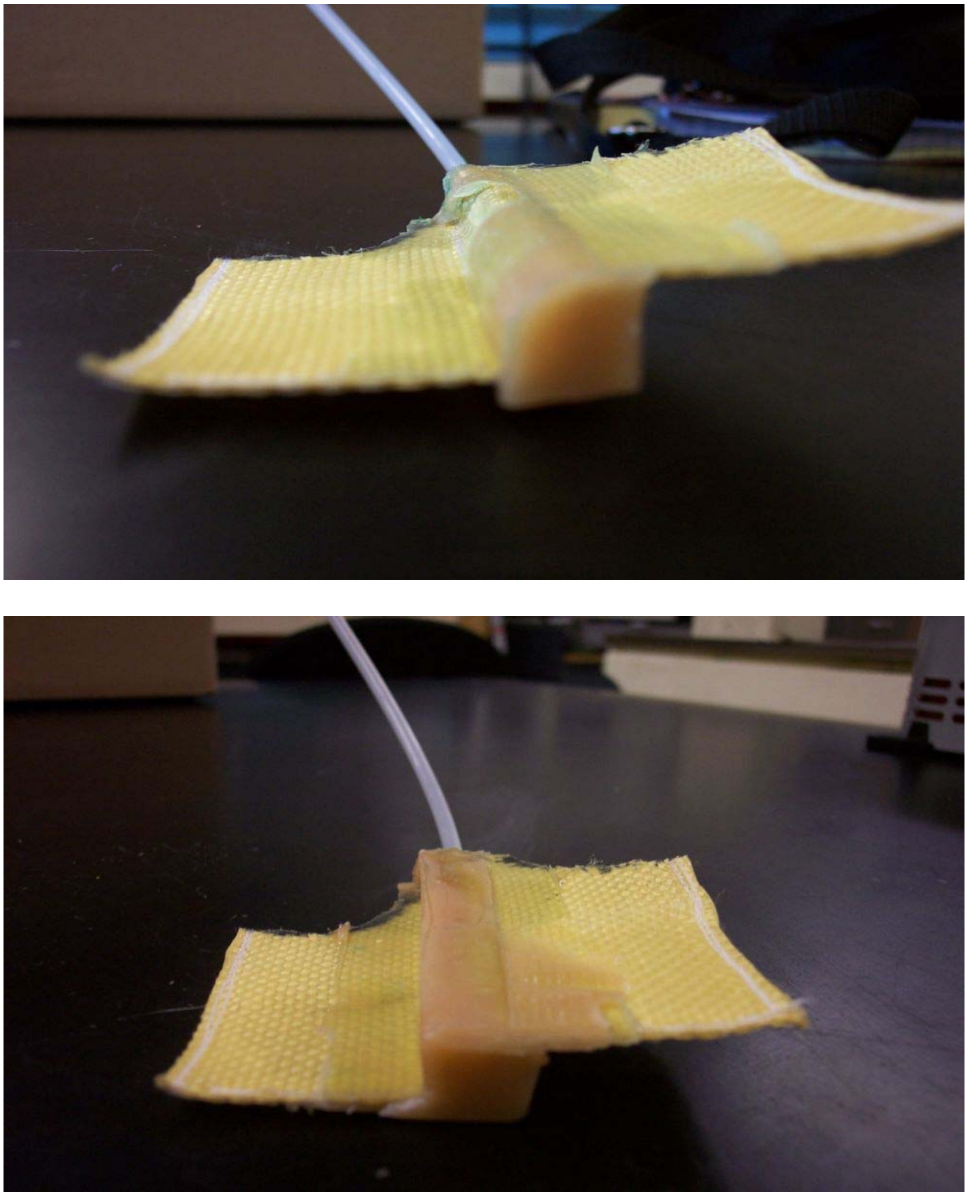

Figure 34. The actuator is fully constructed.
(Top) First part (half), (Bottom) Second work – whole part finished.

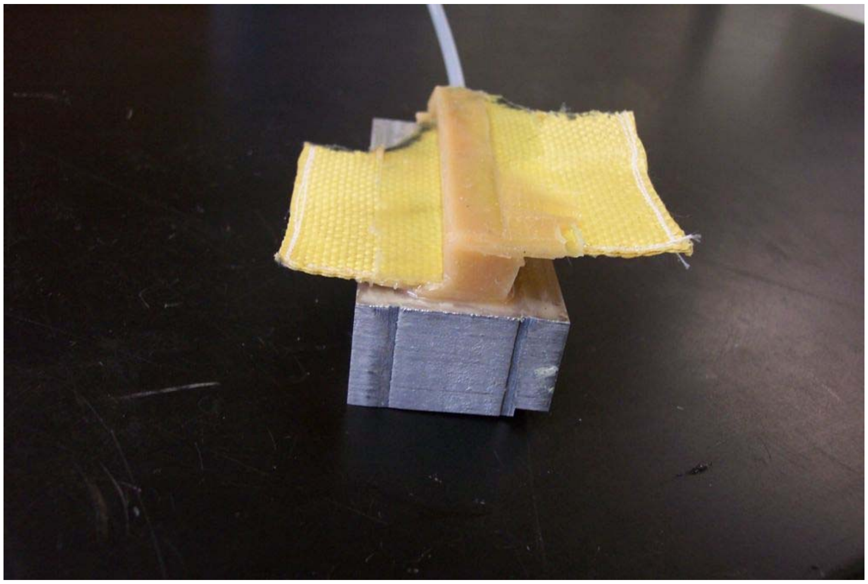

Figure 35. Fabricated shear actuator.
It is bonded to the aluminum block.

3.3.2 Assembly and injection molding of shear actuator

A controlled pressure/vaccum pump provided constant pressure to the balloon inside the lens element to maintain the appropriate initial lens element shape during curing process. After half the actuator is made, the actuator is flipped over to make the remaining half. After finished curing, it is attached to the aluminum plate as the fixed bottom.

3.3.3 Array of shear actuators

A shear actuator panel with 12 elements is fabricated in a similar way to single actuator. The mold is designed to make the half portion, then the other half is made. Then it is fixed to the brass plate as in Figure 36.

Figure 36. A shear actuator panel with 12 elements is fabricated. It is bonded to aluminum base.

CHAPTER IV

EXPERIMENTAL PROCEDURE

4.1 Determination of Hyperelastic Constants

Experimental procedure starts with hyperelastic constants for soft polyurethane matrix. As described in previous chapters, for hyperelastic material, only simple tensile test cannot represent the material property. In this work, simple tensile test and planar tension/pure shear test are performed. In addition, uniaxial compression/biaxial extension test data is estimated and added to the hyperelastic test data to get better material constants to represent material behavior well.

This chapter presents test procedures for simple tensile test and planar tension/pure shear test. The biaxial test data, curvefitting, and hyperelastic constant simulation are described in the next chapter.

4.1.1 Simple tensile test

The tensile test was performed with an Instron 4411 testing machine. This test uses specified the ASTM D638 standard.

4.1.1.1 Conservative Strain to Failure

The cyclic force-displacement relationship - and eventually the cyclic stress-strain relationship – came from a two step procedure.

First, four specimens are tested to failure.

- Install the specimen securely (Figure 37), then mark and measure the gage length.
- Initialize the load cell and displacement
- Set the testing parameters:
  - Crosshead moves at 50.8mm/min (2.0 in/min).
  - The DAQ sample rate is 5 Hz.
- Start the LabView® software to collect the data.
- Start the crosshead.
- Move the crosshead until the specimen fails – repeat the procedure for 4 or more specimens.
- Analyze the data file with spreadsheet software.

Find the shortest strain to failure. Use 90% of the shortest failure strain as the maximum cyclic strain to ensure the specimen not breaking during cyclic tension.

Figure 37. The dog-bone shaped specimen mounted to the crossheads.

4.1.1.2 Cyclic Tensile Behavior

Once the conservative cyclic strain is know, it is time for the second step. As in previous chapter, the hyperelastic material such as soft polyurethane has the Mullins effect. To minimize the Mullins effect, we have to pre-condition the specimen appropriately. At least 4 cycles are needed in this test.

The procedures are same for the first step except that we have to place the stoppage device with calculating the 90% of the shortest failure strain above. If the upper crosshead moves up and hit the stoppage device, it will automatically stop. Then we move the crosshead down until the original position, then move up again. We have at least 4 cycles with this procedure.

The force-displacement plot from the 4th cycle is converted into stress-strain. It will be used to determine the hyperelastic material constants.

4.1.2 Planar tension-pure shear test

Planar tension test also uses Instron 4411 testing machine. It uses wide grip as in Figure 38.

For planar tension-pure shear test, we apply at least 4 pre-conditioning cycles to specimen to remove Mullins effect.

As in the tensile test, the upper part of the specimen is mounted in the upper grip, then the lower part is mounted in the bottom grip. When the test finished, the lower part is removed and then upper part is removed from the grip.

The gage length is also checked. The testing parameters are

- Crosshead speed: 12.7 mm/min (0.5 in/min)
- Sample rate: 5 Hz

After pre-conditioning, the crosshead moves up. For the planar tension-pure shear test in this study, the small dot or cross is marked at the center of the specimen. This is to prove the pure shear condition by observing the dot's shape change.

The crosshead movement is stopped 4 or 5 times until reaching to the top displacement. Pictures are taken with digital camera with focusing the dot at the center. The force-displacement curve is converted into the stress-strain curve and to form another curve in the hyperelastic material test curve set.

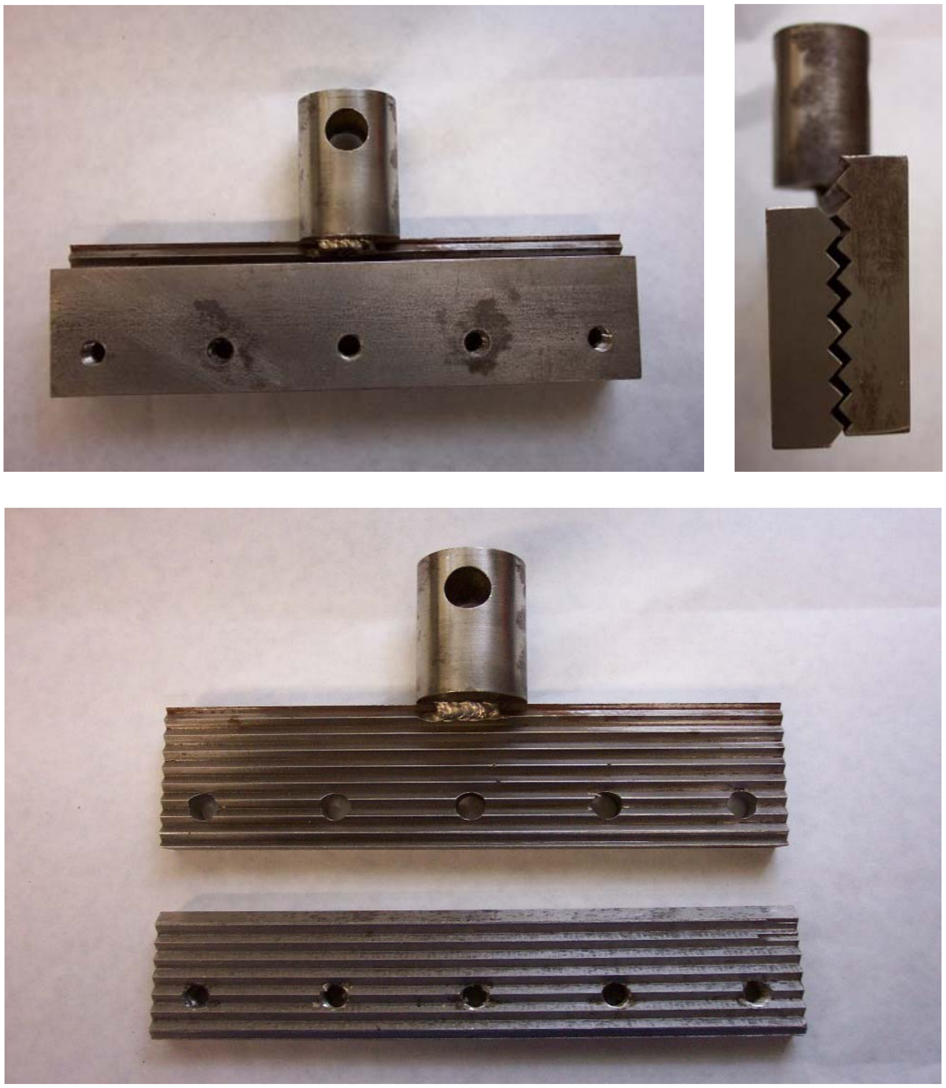

Figure 38. Planar tension test in this work used this grip.
This grip has sharp edges that prevent slipping during planar tension-pure shear test.

4.2 Characterizing the Lens Element – Kevlar Fabric Actuator

Material property—McCutcheon's data—for Kevlar fabric is

- Young's modulus = 100 GPa
- Poisson's ratio 0.35

The lens element is Kevlar fabric, and itself is an actuator. The actuator performance curve is tested by Instron 4411 testing machine. The test procedure is as follows

- A single pull-out test is performed to a Kevlar fabric sheet. The 70% of the maximum force is calculated. This is the conservative force to apply to the lens element.
- The Kevlar fabric lens element sits in the grip as Figure 39 shows. A compressed nitrogen gas fills the lens element.
- After measuring the gage length, the crosshead moves up to reach the conservative force.
- Then it is pressurized by nitrogen gas. At this actuated stage (actuation pressure is held constant), the crosshead moves down slowly so that the Kevlar fabric is going back to the original position.
- The above procedure is repeated for various pressures. The unloading force-displacement represents the actuator performance.

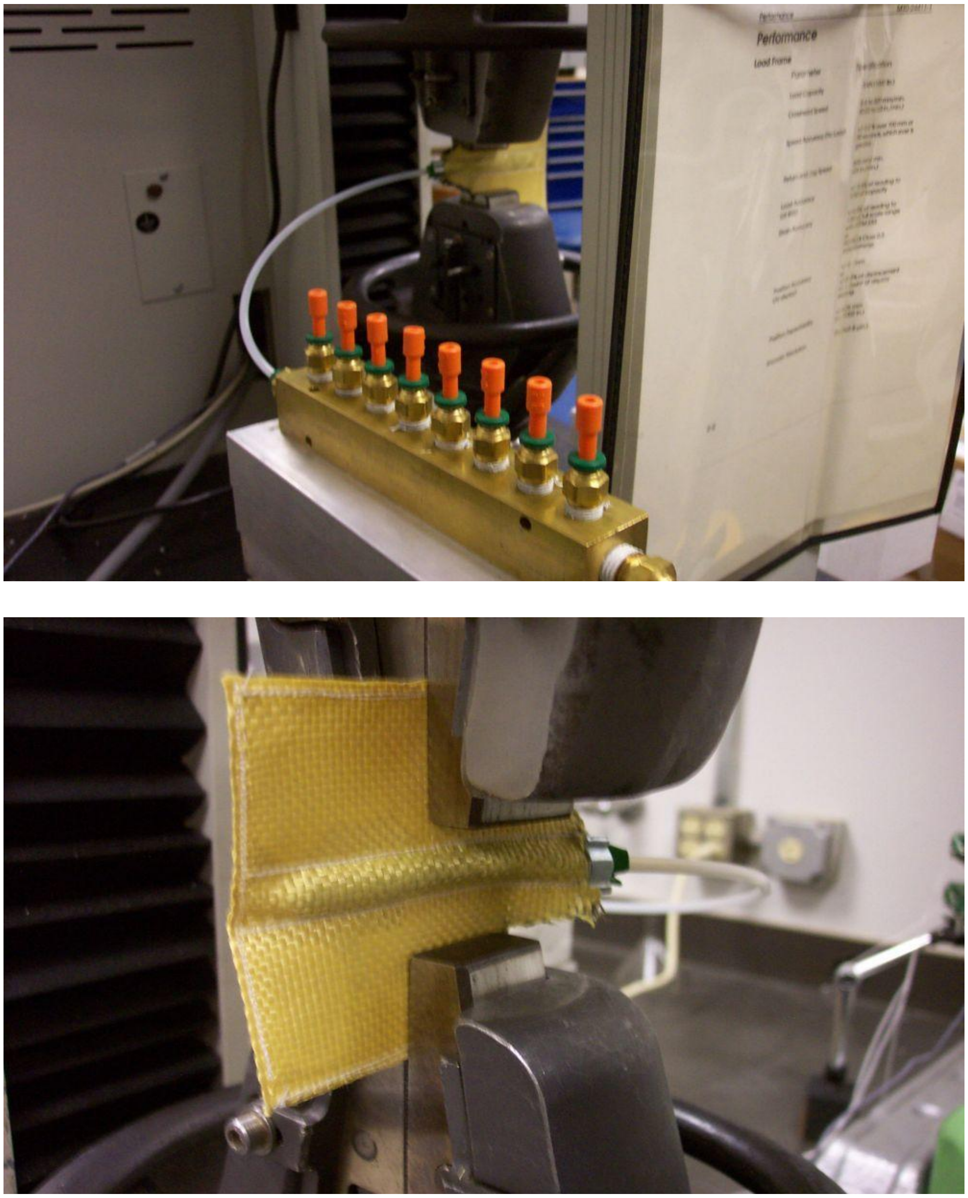

Figure 39. The Kevlar fabric lens element is tested in Instron 4411 machine. A nitrogen bottle is connected to pressurize the actuator.

4.3 Experiments of Shear Actuator- Pressure vs. Free Strain Relationship

To measure the shear amount, the ruler was put on the top of single shear actuator. This shows original reference line. With increasing pressure, the shear amount is measured as in Figure 40. This shows the shear actuator's peak free shear strain vs. pressure plot.

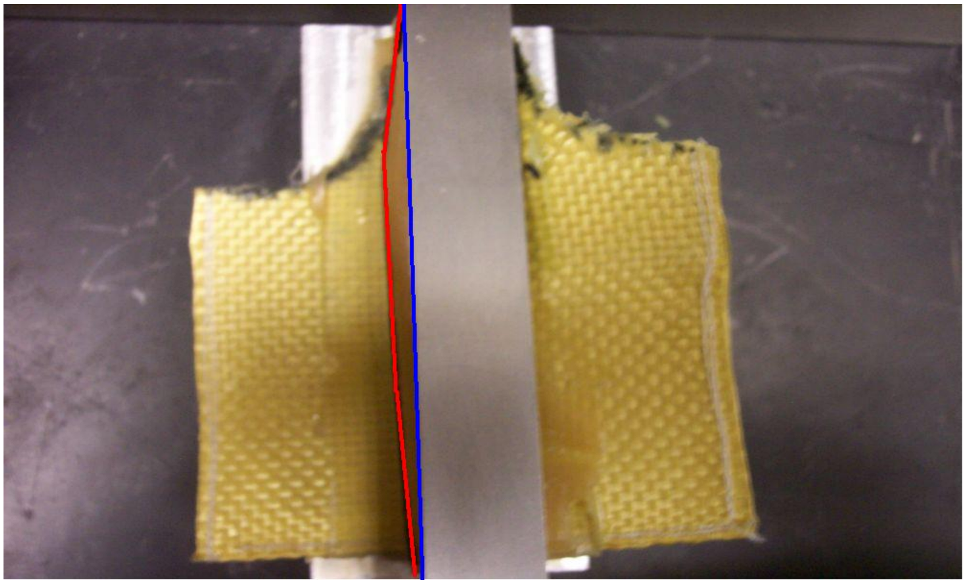

Figure 40. This shows the free strain test for a single shear actuator. The red line shows the free displacement and the blue line shows the initial position.

CHAPTER V

ANALYSIS AND RESULTS OF SHEAR ACTUATOR

5.1 Material Property of Hyperelastic Matrix

In this work, simple tensile test and planar tension-pure shear test have been performed with experimental procedure in previous chapter. For 3rd test data, equi-biaxal tension data is estimated from pure shear test data. Hypereleastic material property (Ogden material model) are found from these three data sets.

FEA simulations show the acceptable range for constants in shear actuator numerical modeling in later a section.

5.1.1 Simple tensile test

Throughout this research, two soft polyurethane resins from Freeman® supply are tested with same tensile test procedure described in previous chapter. The first resin is FMSC 1035T, and it was used in the early stage of hyperelastic material research. It is reported here because the elastomer modeled in this research is based on this resin. The second one is FMSC 1035, which is similar to 1035T. It is the resin used for shear actuator, and in the analysis in this chapter uses this resin.

5.1.1.1 Tensile Test Result of FMSC 1035T® Resin

Dog-bone shaped specimens followed ASTM D638 standard have been made from FMSC 1035T® (Figure 41). It is started with the single tension test using 3 specimens to determine the conservative strain to failure. Test parameters are as the following

- Crosshead speed: 50.8 mm/min (2.0 in/min)
- Sampling rate: 5 Hz
- The gage length: 50mm
- The cross-section area: 18mm^2.

Figure 41. An ASTM D638 specimen from FMSC 1035T® resin is shown after fully cured. The dates when the specimen made have been recorded for every specimen.

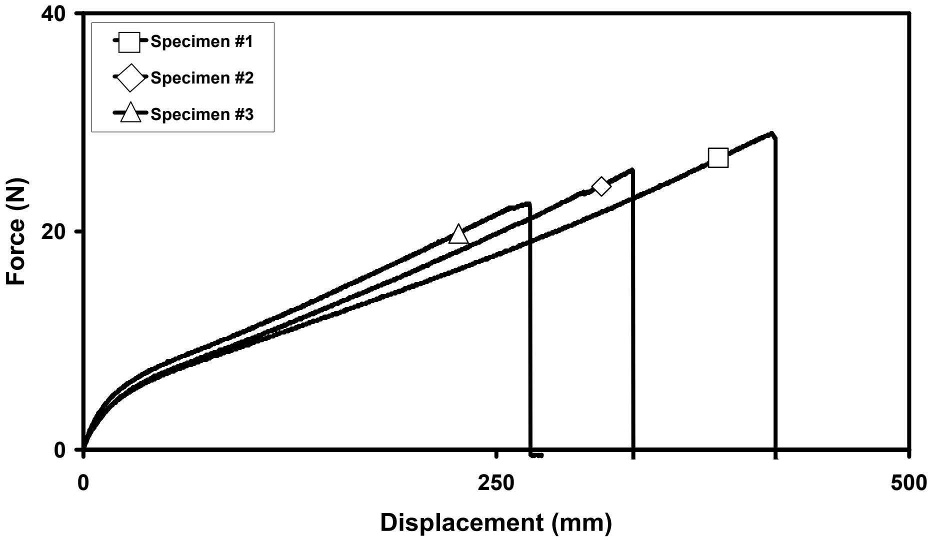

Figure 42. Tensile test result for single extension to failure shows . The force vs. displacement in this plot is converted to stress-strain relationship to determine conservative strain to failure.

The minimum strain to failure from Figure 42 was 667.3%. The 90% of this value was used for cyclic test. The failure stress and strains are shown in Table 2.

Table 2. Failure stress and strains from single pull-out test

Specimen	Failure stress (MPa)	Strain (%)
#1	1.56	855.3
#2	1.42	700.5
#3	1.24	667.3

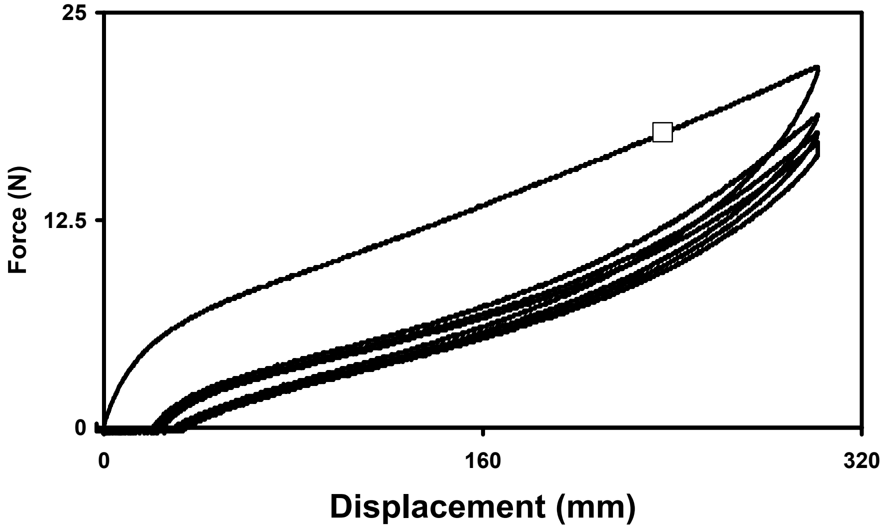

Figure 43. Cyclic test result for a 1035T specimen shows the Mullins effect. The square shows the 1st cycle during increasing displacement.

The cyclic test (Figure 43) has same test parameters as single-pull out test. The 4th cycle data (force-displacement) from 4-cycle test was converted into stress-strain curve (Figure 44) and used to characterize the material constants. Hyperelastic material characterization is described in the later section.

For linear analysis in the earlier stage, the secant modulus is found from the stress-strain curve. The result is shown in Table 3.

The stress and strain values here are all engineering stress and strain values.

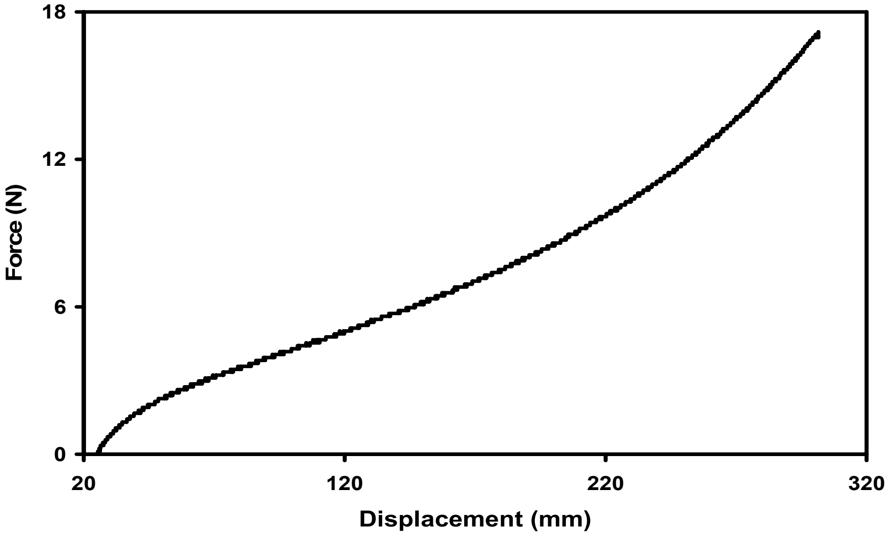

(a)

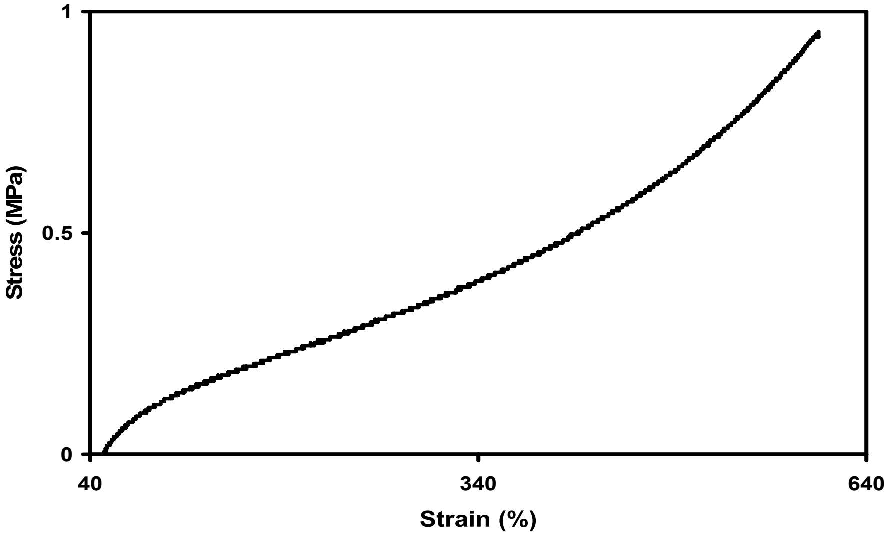

(b)

Figure 44. Tensile test data from the 4th cycle provides the stress-strain relationship; (a) Force-Displacement (b) Stress-Strain

Table 3. Secant modulus comes from tensile test data for the 4th cycle.

Strain (%)	Secant modulus (MPa)
100	0.25
200	0.158
300	0.138
400	0.134

5.1.1.2 Tensile Test Result of FMSC 1035® Resin

This test was done and reported by Ewumi [92] and the procedure described in section 4.1.1. The test parameters are as follows

- Crosshead speed: 50.8mm/min (2 in/min)
- Sampling rate: 5 Hz
- Specimen width: 3.175mm
- Specimen thickness : 3mm
- Gage length: 22mm
- Overall length: 69mm

As in Figure 45, the 90% of the smallest distance to failure was found and used in cyclic test. Force-displacement relationship is found from cyclic test (Figure 46).

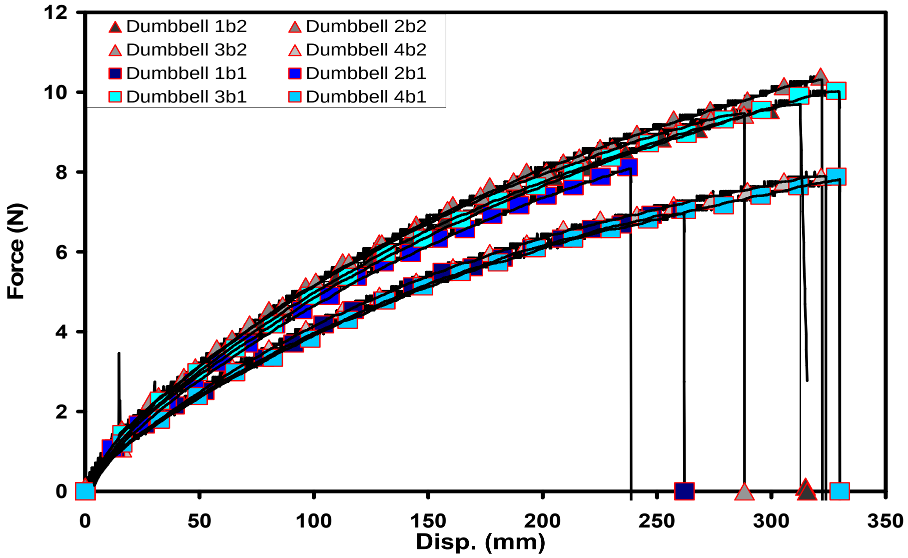

Figure 45. Force vs. displacement plot for 8 specimens to determine maximum length to failure.

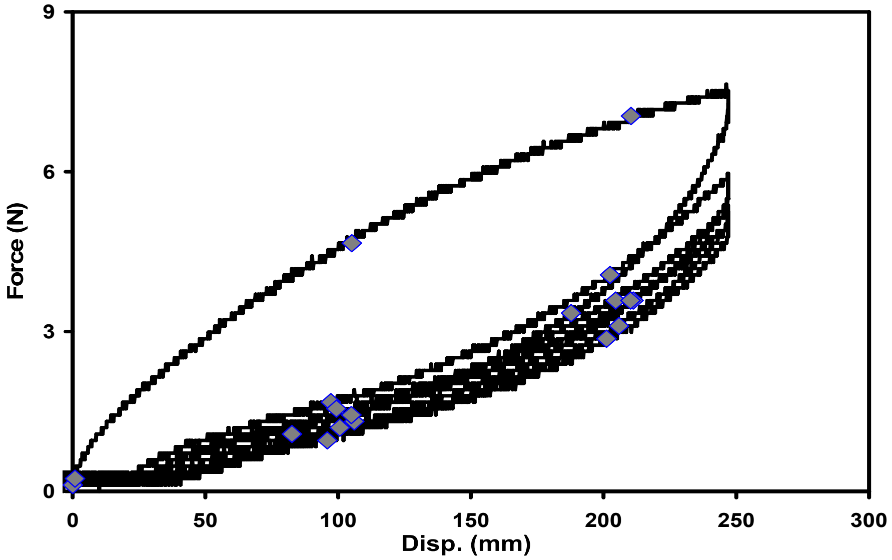

Figure 46. Force vs. displacement relationship is from 4 cycle-test data for 1035 soft polyurethane specimen.

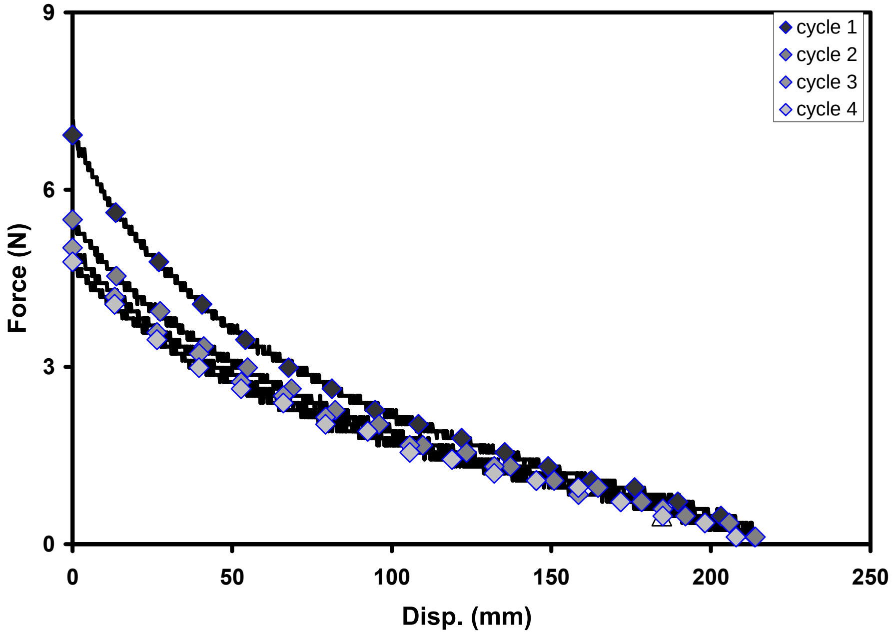

Figure 47. The unloading curve for each cycle show that the unloading response approaches consistent behavior. The 4th cycle test data (force vs. displacement) is converted to stress-strain relationship.

As shown in Figure 47, the unloading curve (force-displacement) is converted to stress vs. strain relationship to determine hyperelastic material property. This is described in later section.

5.1.2 Planar tension-pure shear test

The planar tension test specimens are built from 1035 resin. The wide grip has sharp edges and it gives the unexpected specimen failure during the test as in Figure 48. Therefore, as in Figure 49, thin cloths are applied to the specimen surface to keep the grip serrations from cutting the specimen. The edges are grounded by the files. The even clamping force help prevent slipping during the test.

Figure 48. Sharp edges in the wide grips cut the specimen during initial work.

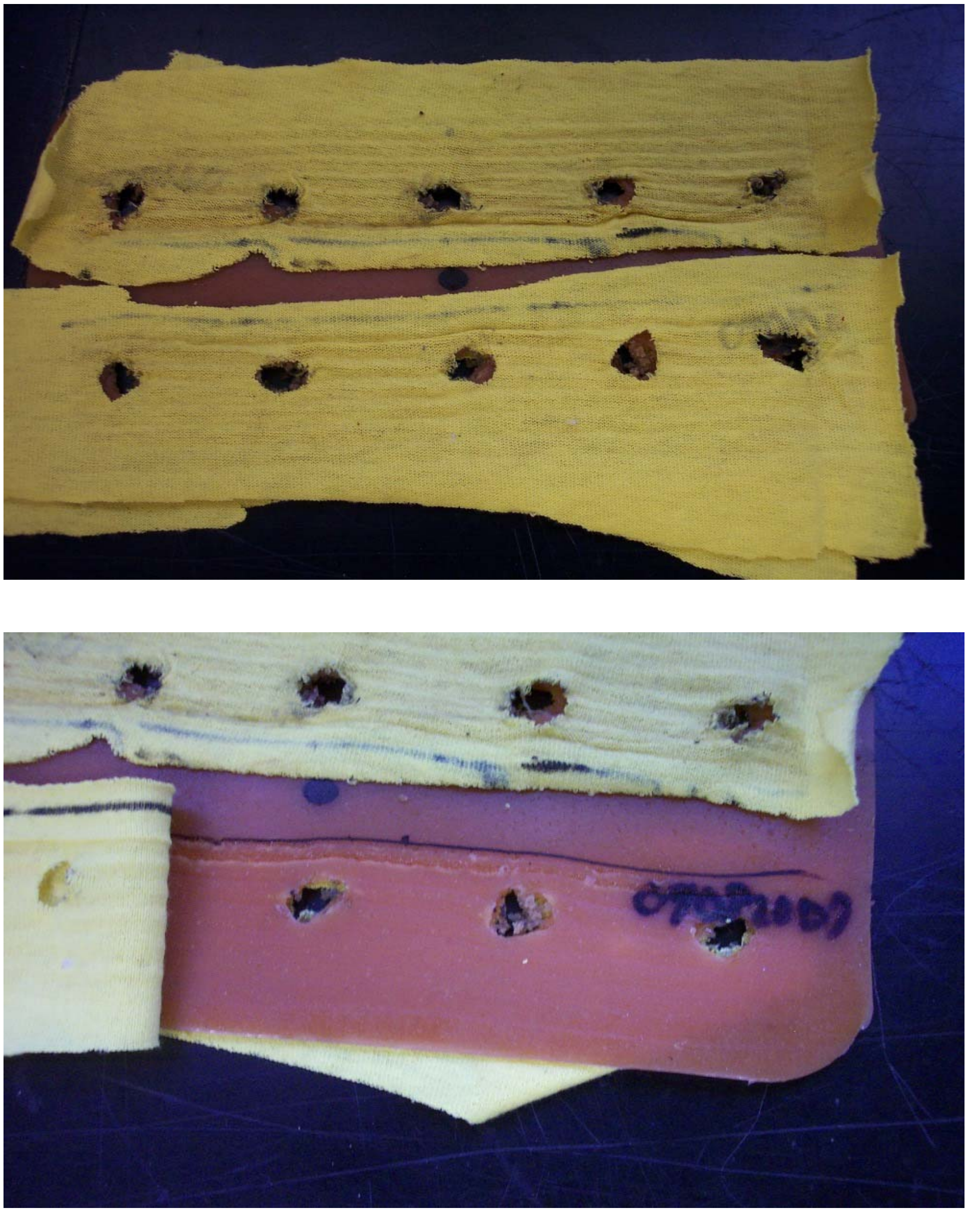

Figure 49. Thin cloths applied on the grip surface allow the test to run without the gripped regions failing. The edges still mark the specimen, but it can endure the planar tension-pure shear test without failure.

With cloths applied to prevent the specimen from failing in the grip, three specimens—denoted as Specimen #1, Specimen #2, and Specimen #3—have been tested and reported in this work.

All specimens were pre-conditioned more than 4 cycles before the test was performed. The planar tension-pure shear test test parameters are as follows

- Gage length: 24.5mm
- Crosshead speed: 12.7 mm/min (0.5 in/min)
- Sample rate: 5 Hz,
- Aspect ratio of specimen: 7.2:1

Figure 50. Picture 1 shows the planar tension-pure shear test for Specimen #1. The small cross in the center of the specimen shows the deformation state of planar tension that is equivalent to pure shear. The marker to the right of the small cross is a reference for image analysis.

Figure 50~Figure 54 show the pictures from the planar tension-pure shear test of Specimen #1. For this case, a small cross was used to show the deformation state of the specimen.

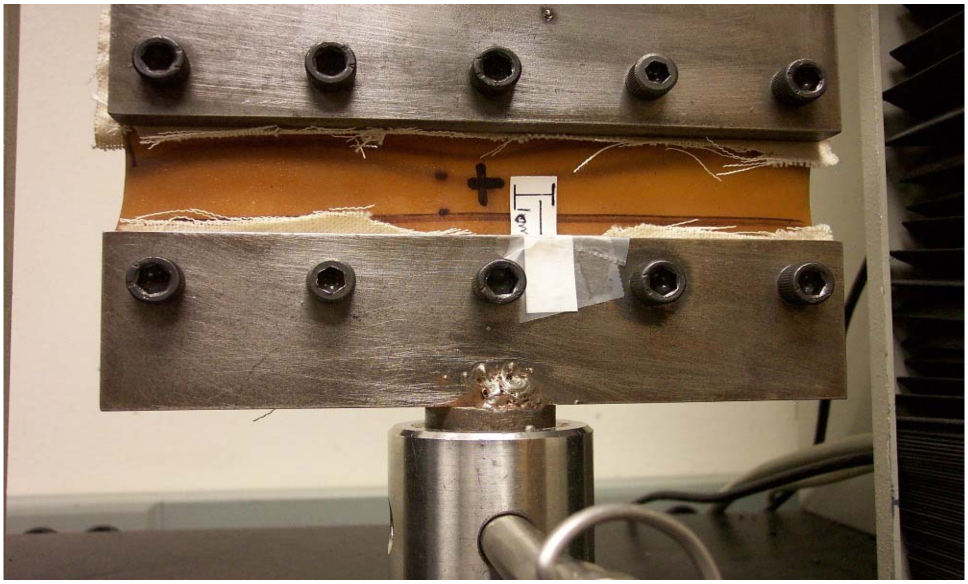

Figure 51. Picture 2 shows Specimen #1 at larger stretch. This shows about 26% deformation.

Figure 52. Picture 3 shows Specimen #1 at about 52% deformation.

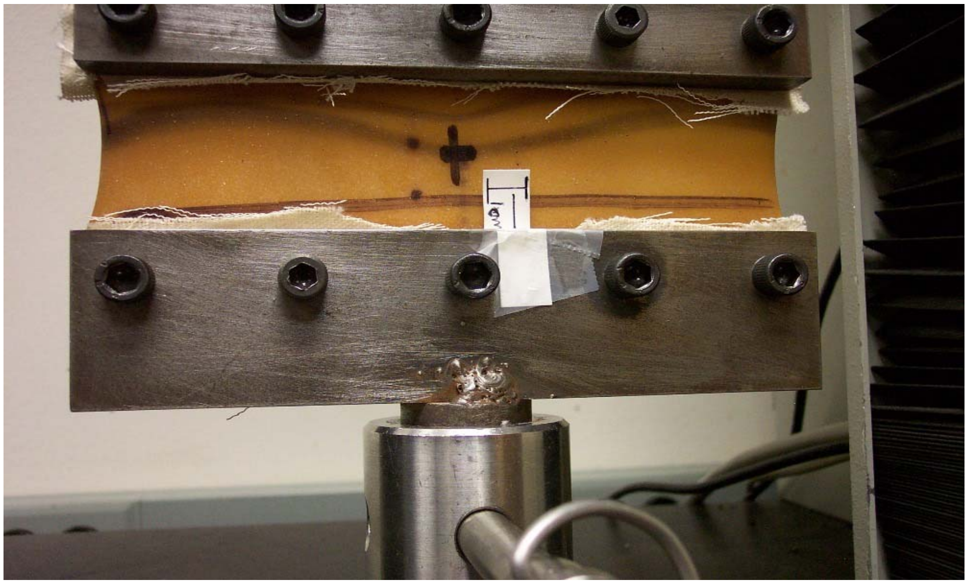

Figure 53. Picture 4 shows Specimen #1 at about 78% deformation.

Figure 54. Picture 5 for Specimen #1. The crosshead movement stopped at about 103% deformation, took this picture, and started in reverse direction to record downward curve.

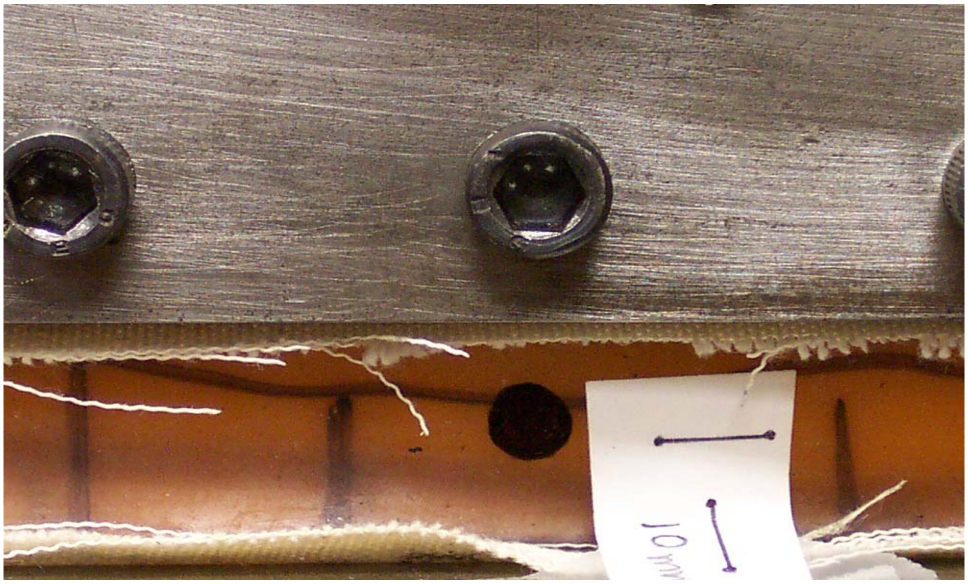

Figure 55. Picture 1 for planar tension-pure shear test with Specimen #2 shows the dot applied to the center of the specimen to verify that the pure shear condition is achieved. This picture is the reference shot that sets the dot's initial dimensions.

Figure 55~Figure 59 show the pictures from the planar tension-pure shear test of Specimen #2. The pictures show a dot applied to the center of the specimen to show the deformation state of the specimen.

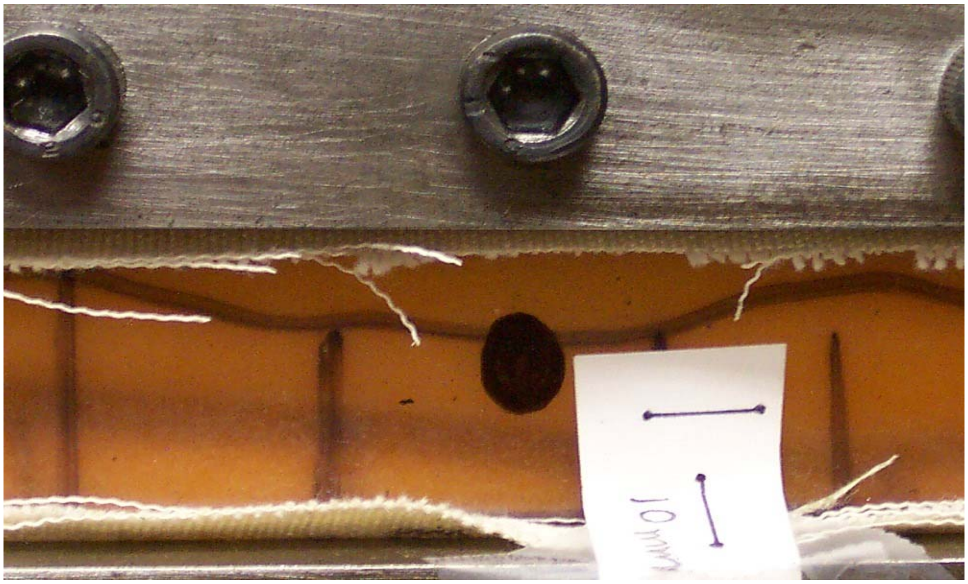

Figure 56. Picture 2 shows the dot on Specimen #2 at about 28% deformation from crosshead movement.

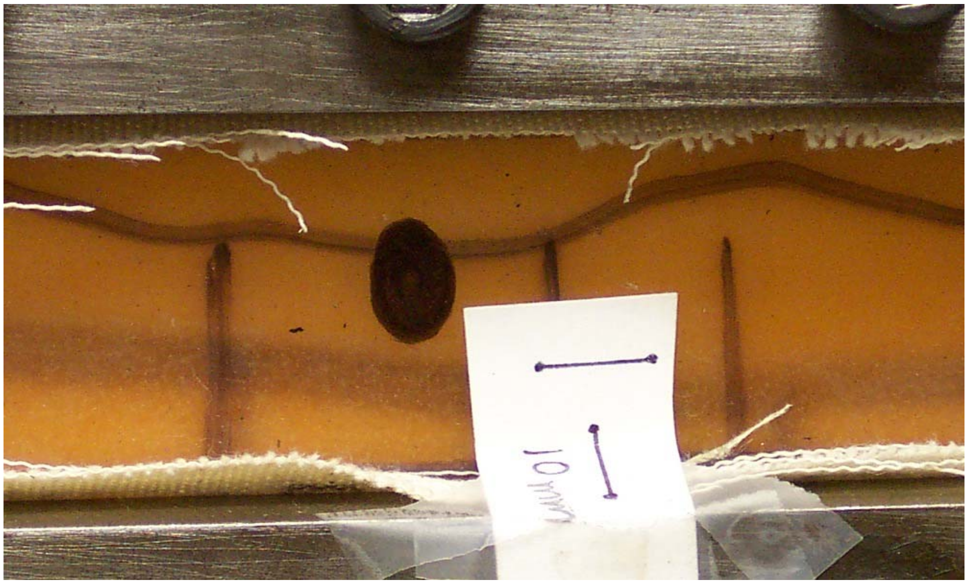

Figure 57. Picture 3 for Specimen #2 shows the dot's ellipsoid shape at about 58% deformation.

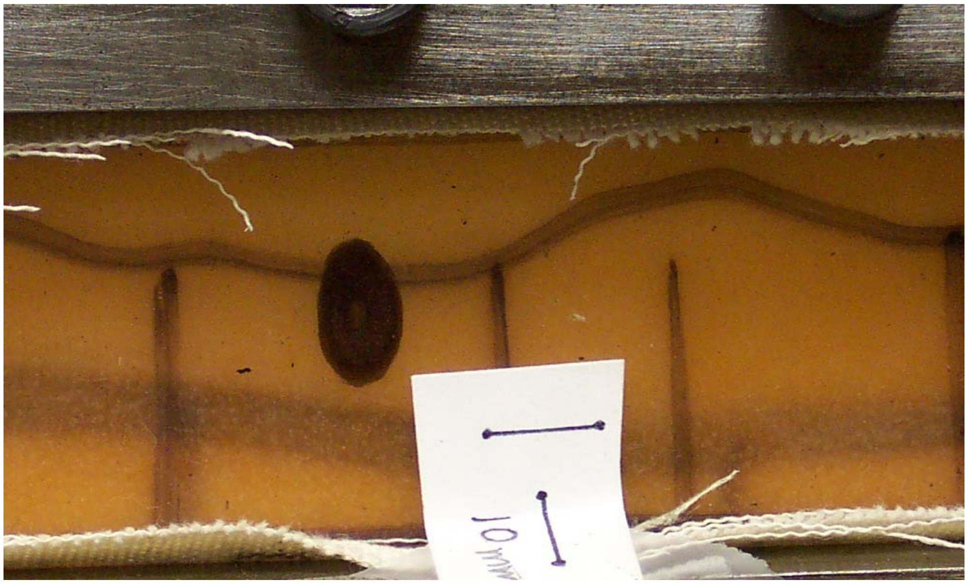

Figure 58. Picture 4 for Specimen #2 shows about 82% deformation.

Figure 59. Picture 5 for Specimen #2 shows the dot with the crosshead stopped at about 108% deformation; this is the maximum deflection applied.

Specimen #3 broke due to the previous split even though it had the fabrics to prevent unexpected break (Figure 60 and Figure 61). Test for Specimen #2 run well and matched well with Specimen #1 results as in Figure 61.

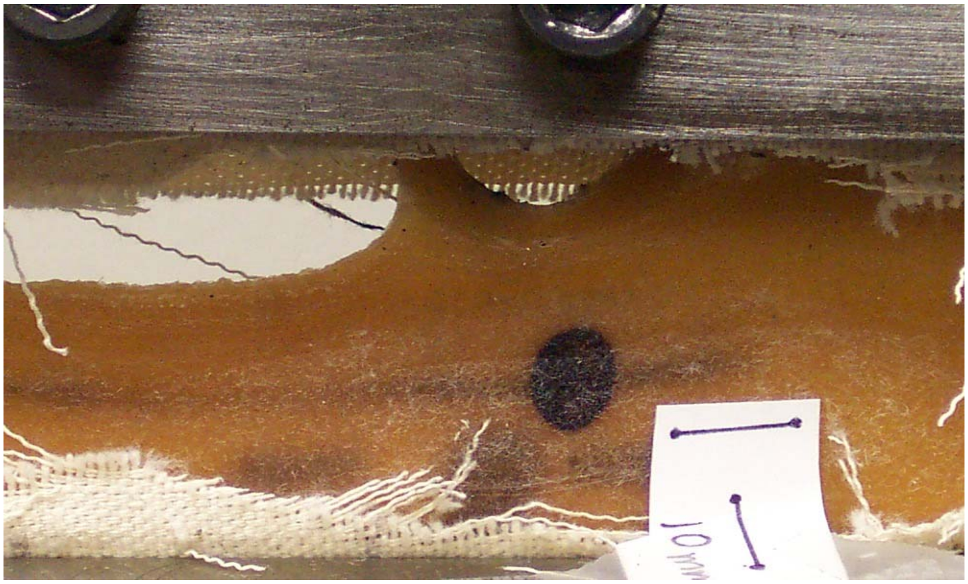

Figure 60. Specimen #3 broke during the test.

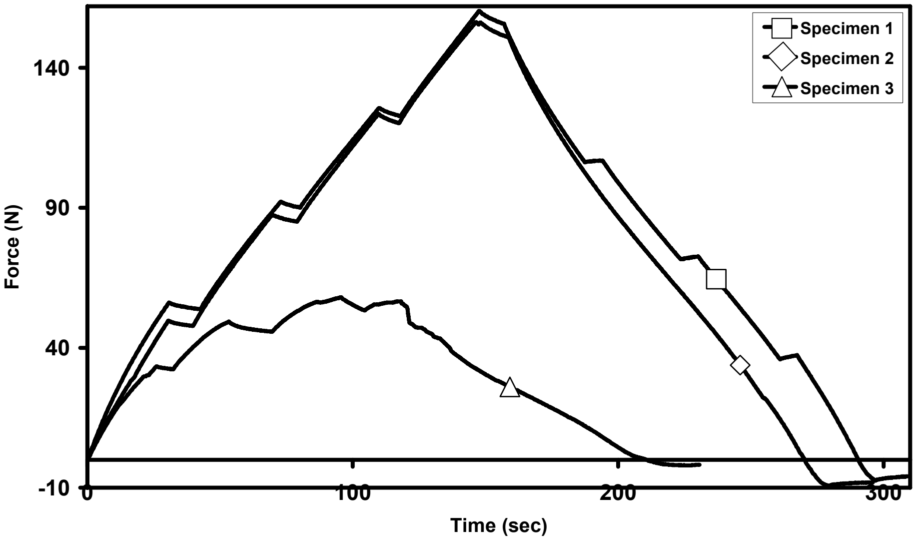

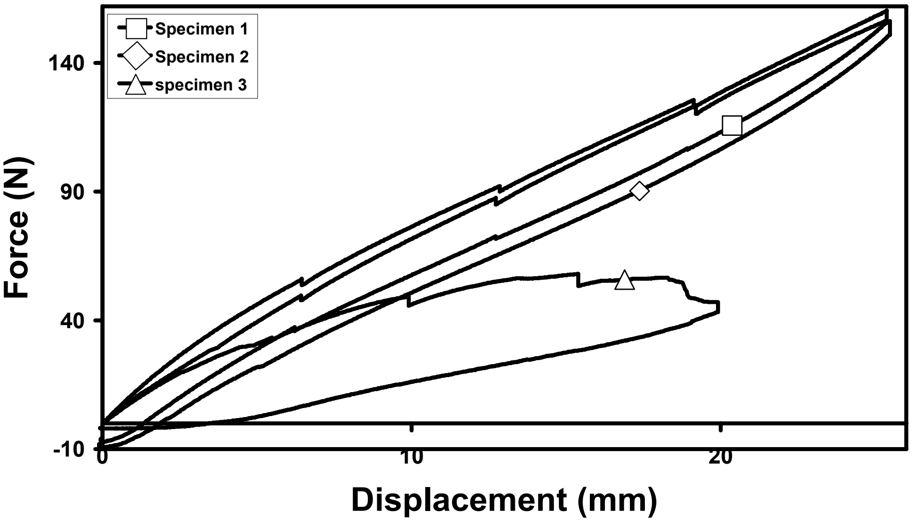

Figure 61. This force vs. time and force vs. displacement shows the uploading curve from Specimen #1 and #2 are relatively matched well. However, it also shows Specimen #3 was broken unexpectedly during the test.

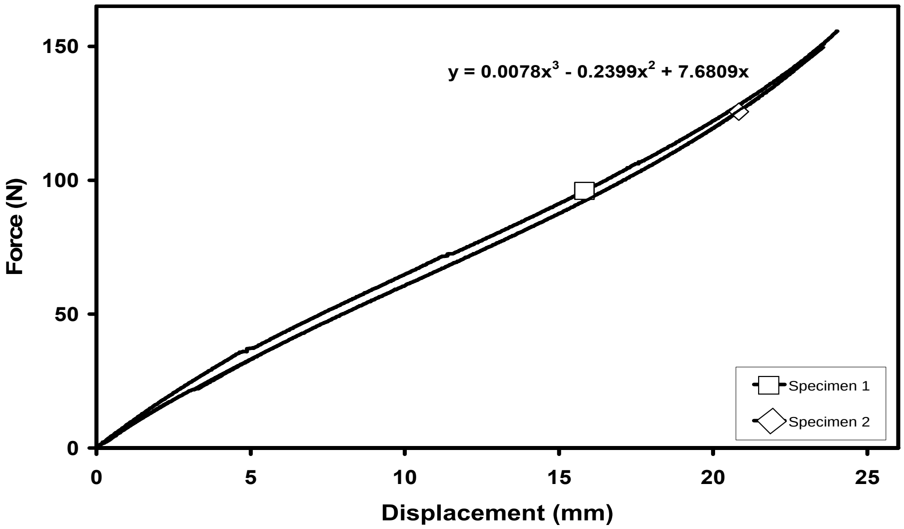

Figure 62. The uploading force vs. displacement relationship for Specimen #1 and Specimen #2 from Figure 61 are similar. Because uploading curves for this case had uneven points (stopped to take pictures), trendline has applied to get a smooth curve.

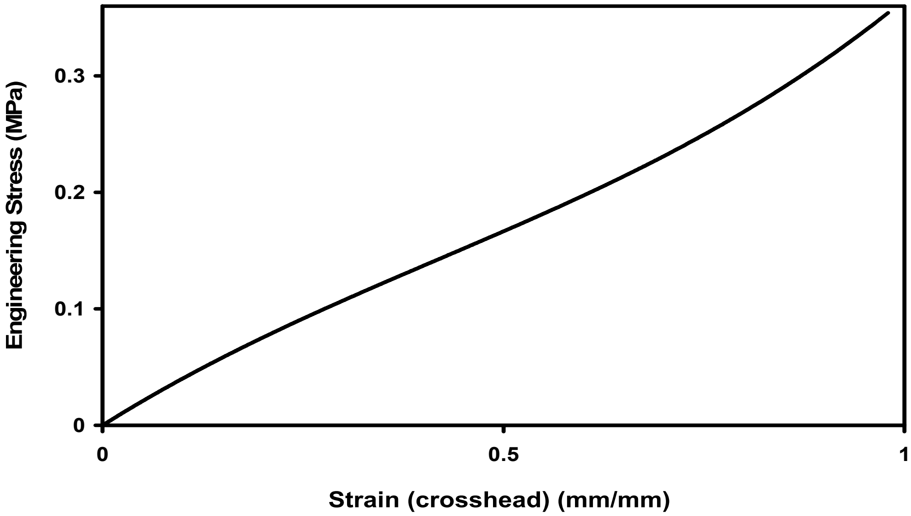

Figure 63. The smoothed line (Force vs. displacement) are converted into stress vs. strain relationship for planar tension-pure shear test. This test data are added to the hyperelastic test curve set to obtain new Ogden constants.

As shown in Figure 61~Figure 63, stress vs. strain relationship is determined from planar tension test. To determine that planar tension test data is equivalent to pure shear data, a small cross was applied to Specimen #1 (Figure 50~Figure 54), and a dot to Specimen #2 (Figure 55~Figure 59). The small cross and dot support checking the difference between the stretch in the polymer and the stretch calculated from crosshead movement.

Here the analysis starts with the difference between vertical deformation calculated from the crosshead movement and from the small cross/dot. As shown in Figure 64, cross's vertical deformation is 105.1%, and the vertical deformation calculated from the crosshead movement is 103.57%. The deformation from crosshead movement is 1.48% less than small cross.

Similarly, from Figure 65, the small cross deformed 108.34% vertically, and gage length vertical deformation is 103.984%. The deformation from crosshead movement is 4.19% less than small cross. From these numbers the values agree within 1.48~4.19%. Therefore, the author claims no difference exists, and the displacement data from crosshead movement was used to calculate strains.

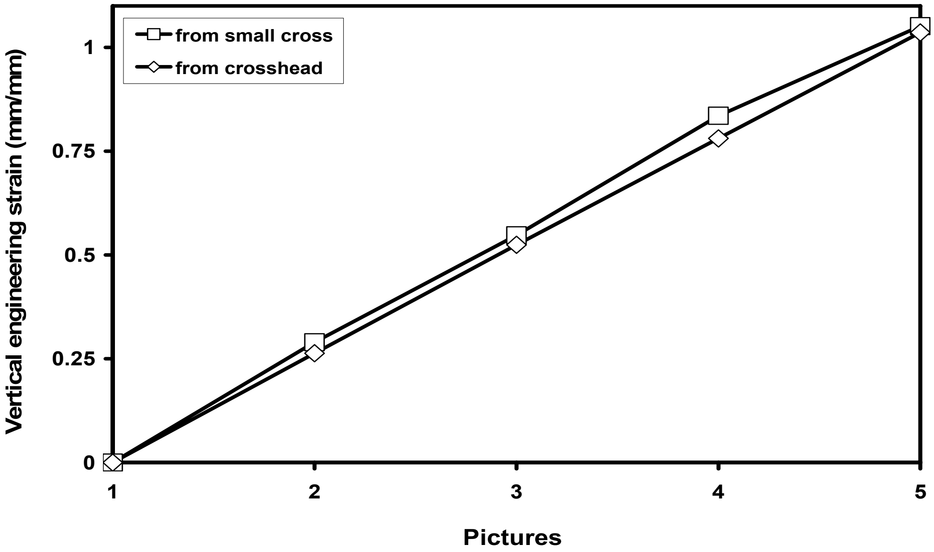

Figure 64. Strain calculated from small cross measures and from crosshead movement for Specimen #1 show strain data from crosshead movement (at 103.6% deformation) are 1.48% less than the data from dot (105.1% deformation) in the middle of the specimen.

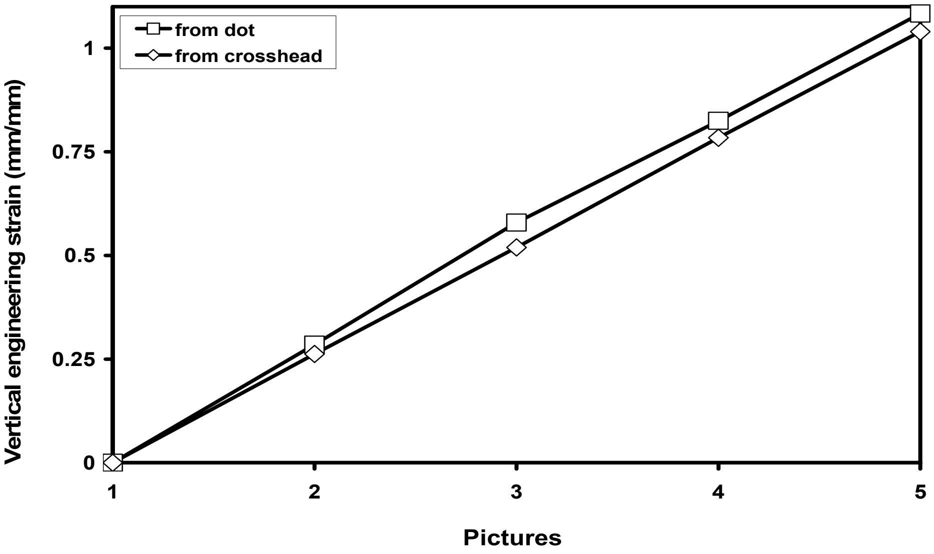

Figure 65. Vertical strain calculated from the dot displacement and from crosshead movement for Specimen #2 shows crosshead movement strains (at 104% deformation) are 4.19% less than the data from dot (108.3% deformation) in the middle of the specimen.

Now, next question is the data from this planar tension test is equivalent to pure shear condition. The explanation about this question is as follows.

Figure 66 and Figure 67 show the image analysis for the small cross (Specimen #1) and for the dot (Specimen #2), respectively. In Figure 66, when the small cross deformed 105.1% vertically in the planar tension test for Specimen #1 (Figure 50~Figure 54), the cross narrowed 0.68% horizontally.

In a similar manner, a dot on planar tension Specimen #2, see Figure 55~Figure 59, narrowed 0.04% horizontally at 108.3% vertical deformation as Figure 67 shows. Therefore, the horizontal strains in Figure 66 and Figure 67 are shown as almost zero compared to vertical strains.

Specimen #1 and Specimen #2 strain states appear as 3D Mohr's circles in Figure 68 and Figure 69, respectively. Both figures have zoomed picture at origin, and dotted lines represents slightly displaced from pure shear condition.

In Figure 68, the small cross strained 71.8% vertically and 0.68% horizontally. For Mohr's circles, true strains are used because planar tension-pure shear conversion is from true strain measure. The vertical extension/horizontal contraction ratio is 104.5:1.

Similarly, Figure 69 shows 73.4% vertical extension and 0.04% horizontal contraction measured from the dot on Specimen #2. For this strain state, vertical extension/horizontal contraction ratio is 1834.9:1.

To make sure these are pure shear condition or not, a reference has been found. Treloar performed planar tension test in ref. [93]. He regarded 520% vertical extension and

12% horizontal contraction as pure shear condition. The vertical extension/horizontal contraction ratio is 43:1.

Compared to Treloar's work, strain states in Specimen #1 and Specimen #2 are regarded as pure shear condition because they have significantly higher vertical extension than horizontal contraction. This means the horizontal contraction at the specimen's centroid is small compared to the vertical deformation; therefore, the plain strain condition was achieved . Planar tension data obtained from wide specimen test can be converted to pure shear data, and it will be added to hyperelastic material parameter set.

The thickness change near the specimen's centroid can be calculated from the measured stretches if the incompressibility applies. The change in thickness can be estimated from vertical stretch by incompressibility condition ($\lambda_1\lambda_2\lambda_3 = 1$, which means volume is conserved during deformation), and plain strain assumption ($\lambda_2 = 1$, which means there is no change in width direction).

The calculation results are summarized in Table 4. As a conclusion, the thickness change between estimation from experimental results and theoretical values are 0.04 % ~ 0.68%.

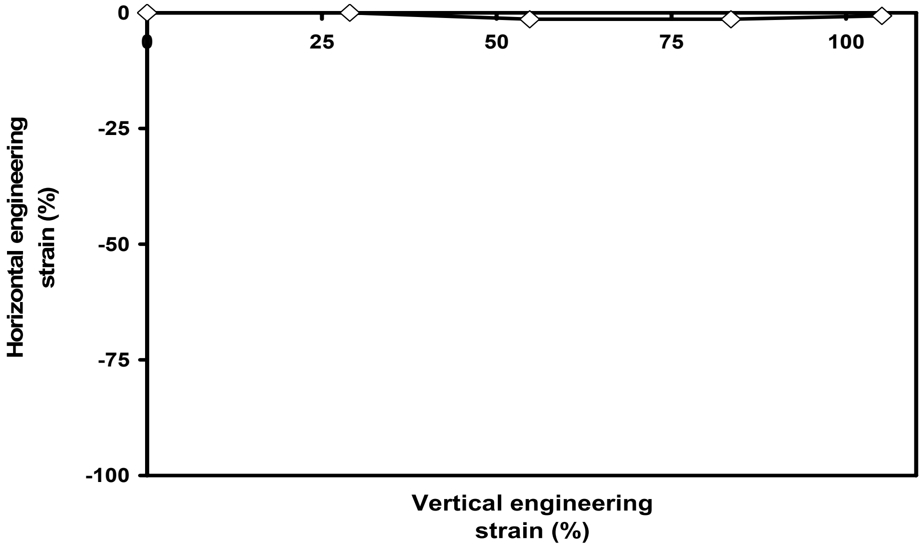

Figure 66. Vertical strain vs. horizontal strain from a small cross placed on Specimen #1 shows that the cross got narrower by less than 1.4%; therefore, horizontal strains in these planar tension experiments are almost zero.

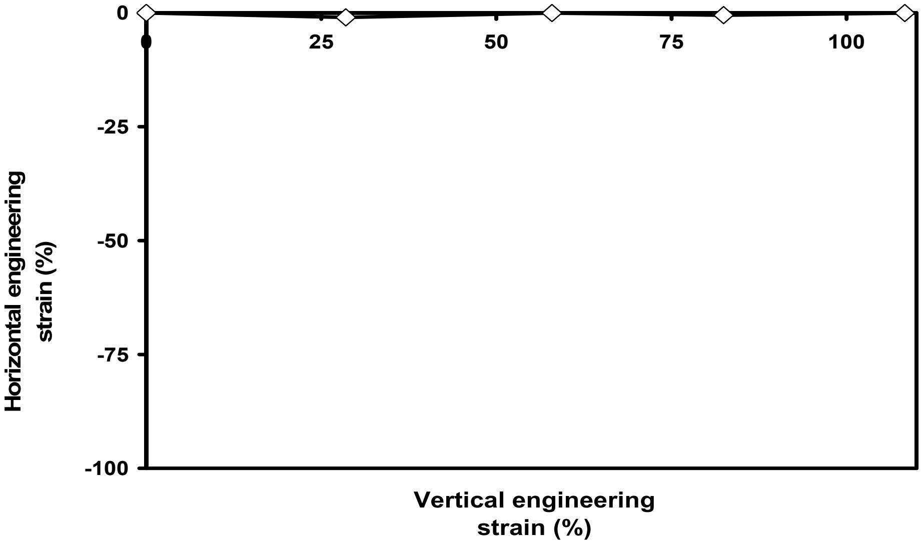

Figure 67. Vertical strain vs. horizontal strain from the dot maker on specimen #2 shows that the dot got narrower by less than 1% with 108.3% vertical strain. Therefore, the horizontal strains are almost zero.

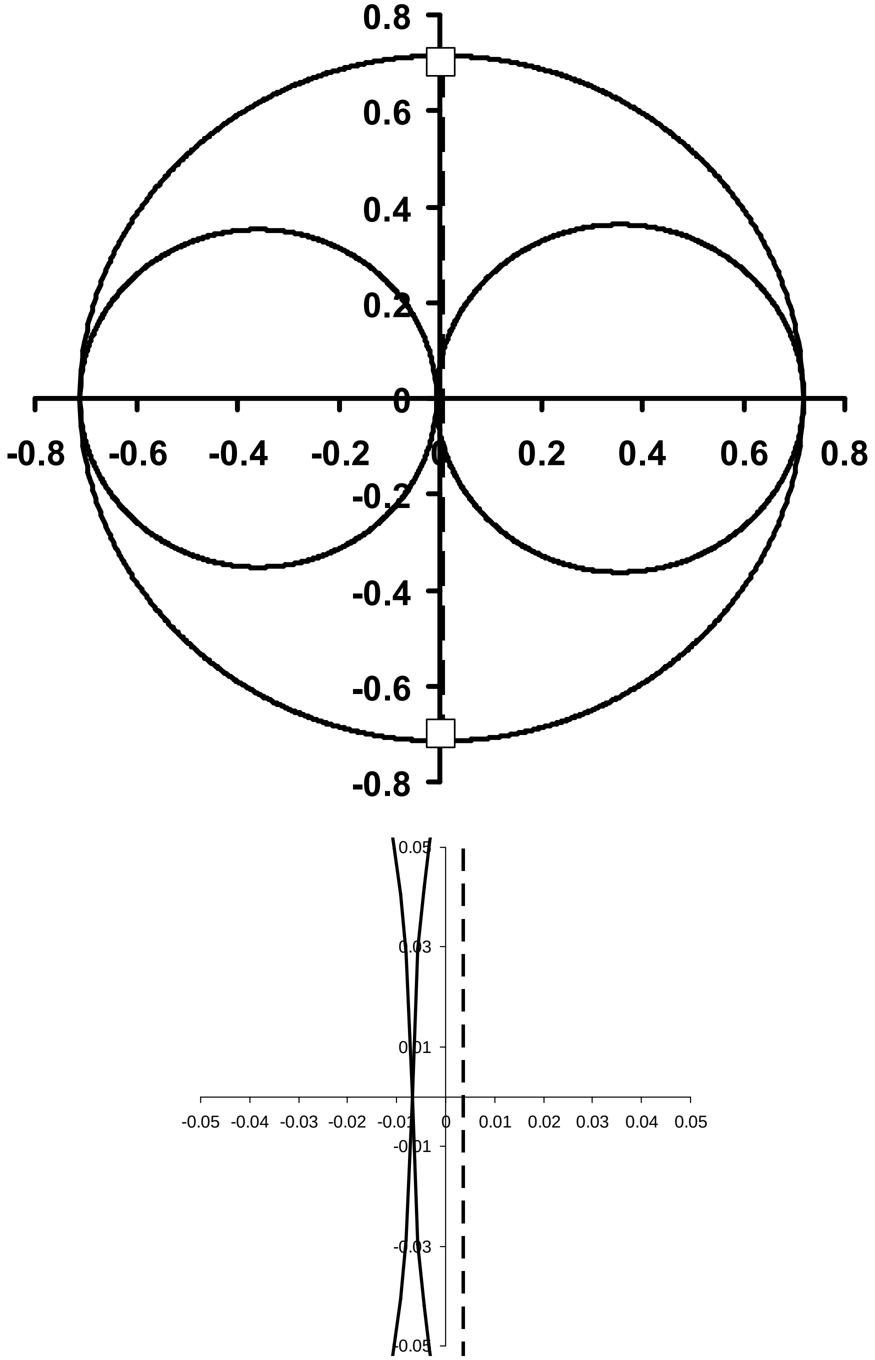

Figure 68. The 3D Mohr's circle from the strain state for the small cross on Specimen #1 shows nearly planar tension behavior. Treloar [93] regarded 520% vertical extension and 12% horizontal contraction (43:1) as pure shear condition. By this criterion the present (104:1) can be treated as the pure shear condition.

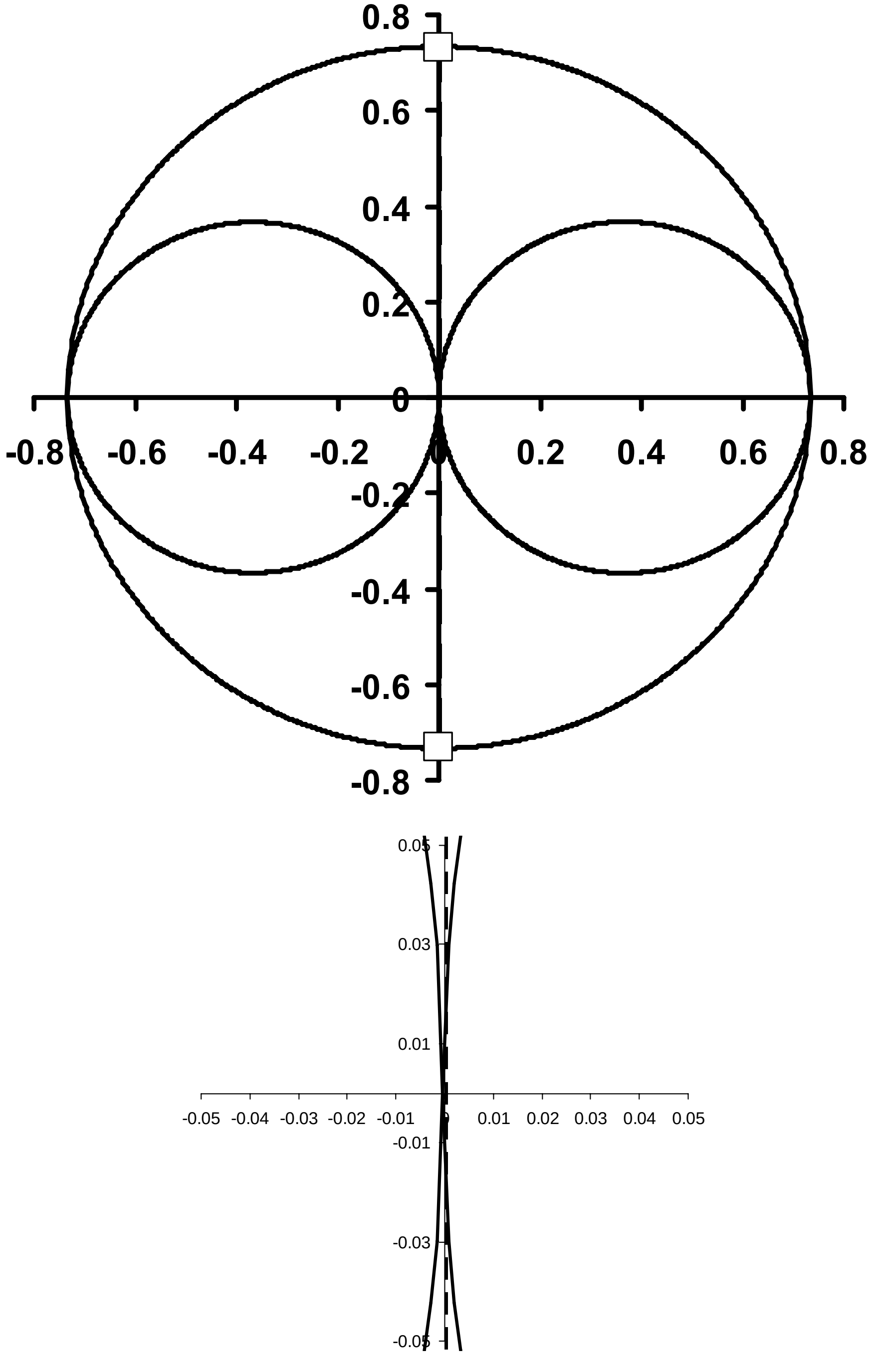

Figure 69. This graph shows that the dot target on Specimen #2 provides a vertical/horizontal stretch ratio that exceeds that Treloar accepts as planar shear.

Table 4. Principal stretches from the center region stretches for Specimens #1 and #2 are close to the ideal values. Parameter λ_1 is the vertical stretch, λ_2 is width stretch, and λ_3 is thickness stretch. Ideally, λ_2 is unity. In the experiment, λ_2 is less than unity.

	λ_1 (Max. value)	λ_2 (Max. value)	$\lambda_3 = 1/(\lambda_1\lambda_2)$ (Calculated from experiment)	$\lambda_3 = 1/\lambda_1$	Difference (%) between experiment and theory
Specimen #1	2.051	0.9932	0.4909	0.4875	0.68
Specimen #2	2.0834	0.9996	0.4802	0.47999	0.04

5.1.3 Hyperelastic material characterization and simulation from 1035T resin

Since Ogden model demands 3-D test data, the error may occur with simple tension test only. Before shear or biaxial test is implemented, using the typical elastomer stress-strain relationship appearing in Figure 70, these test data has been assumed based upon simple tensile test data in Figure 71 to make better accuracy in curvefitting to find material constants [94]. The FEA hyperelastic material simulation is performed and described in this section.

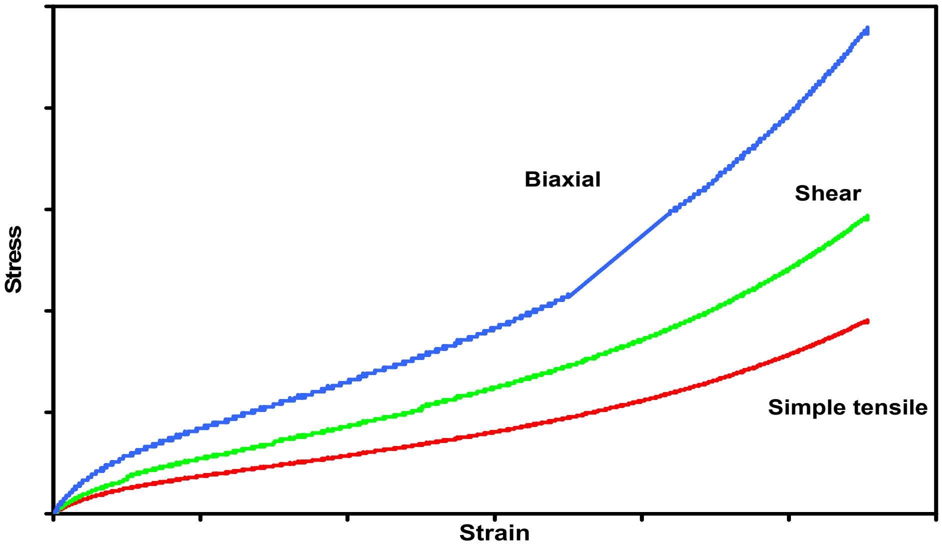

Figure 70. Typical Elastomer Stress-Strain Data Set (after ref. [94])

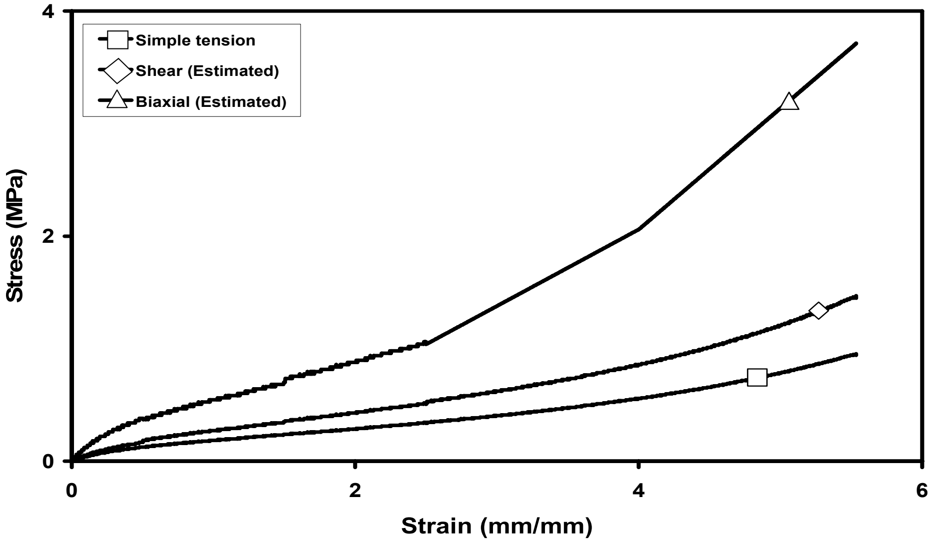

Figure 71. Shear and Biaxial test data assumed using the relationship in Figure 70.

Finally Ogden constants were found using 3 data sets. Commercial FEA software Algor® has been used.

$$\mu_1=3.52521,\ \mu_2=-0.0454221,\ \mu_3=0.00399199\ \text{MPa}$$
$$\alpha_1=0.0751,\ \alpha_2=-1.57,\ \alpha_3=3.9537$$

5.1.3.1 FEA Simulation of 1035T Specimen - Simple Tensile Test

The Ogden constants are consistent only if the FEA model for each experiment returns the same parameters entered. The first check is the simple tension test. Here the properties measured and estimated for 1035T polyurethane. The dog-bone type specimen was modeled—see Figure 72—and the simple tensile test simulated. The simulation results shows good agreement with tensile test data until 120% strain (Figure 73), but it didn't run after that.

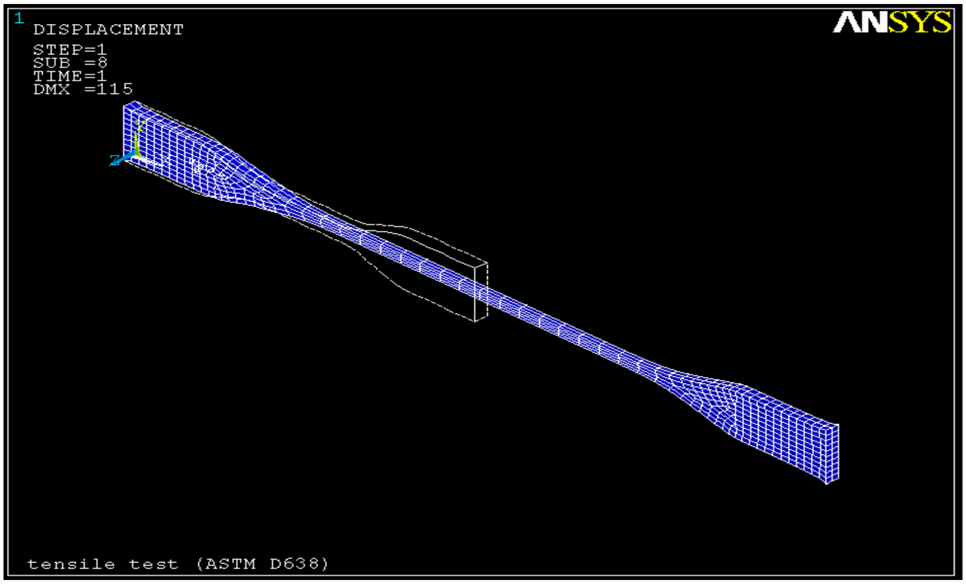

Figure 72. ASTM D638 specimen is simulated using Ogden hyperelastic material constants (100% strain shown).

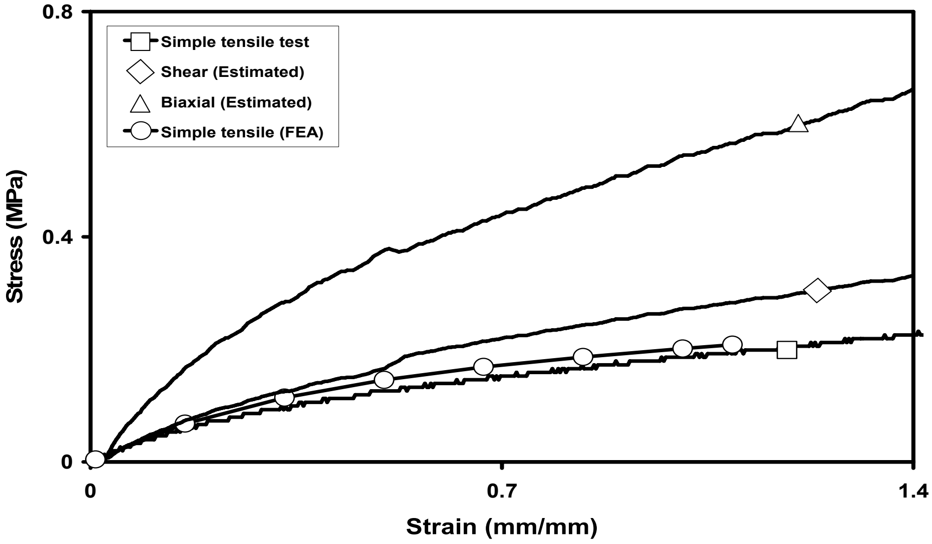

Figure 73. FEA simulation for the simple tensile test shows good agreement to 120% strain.

5.1.3.2 Planar Tension-Pure Shear Test

The FEA simulation for planar tension test started with 200 mm X 30 mm X 1.6mm model (Figure 74 and Figure 75). The specimen aspect ratio is 6.667:1. Boundary conditions imposed as

- Bottom plane of specimen is fixed.
- Top plane can only move vertically.
- Left and right edges are free.

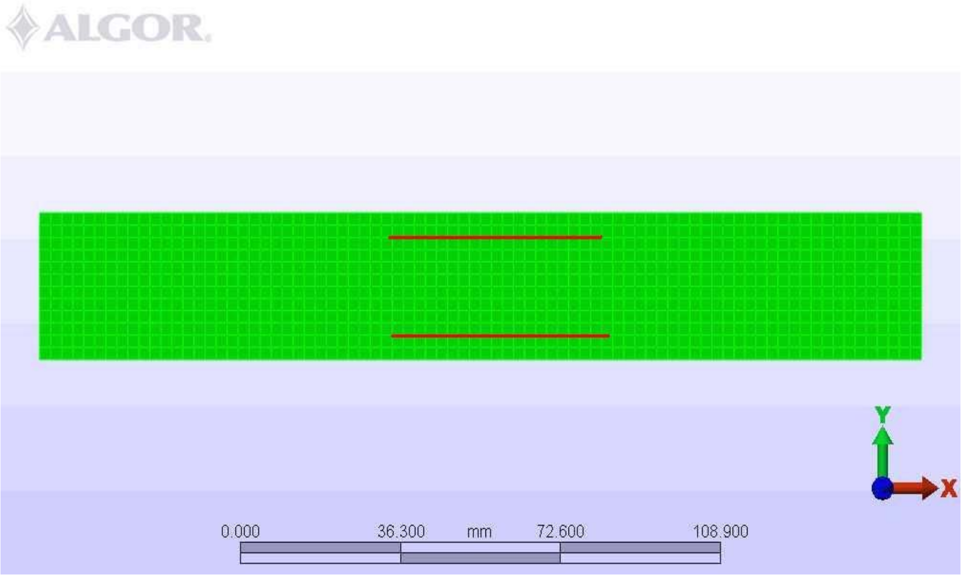

Figure 74. This specimen was modeled by Solidworks® and Algor® software as preprocessor, and then imported by ANSYS for analysis. The red lines are for calculating the strains.

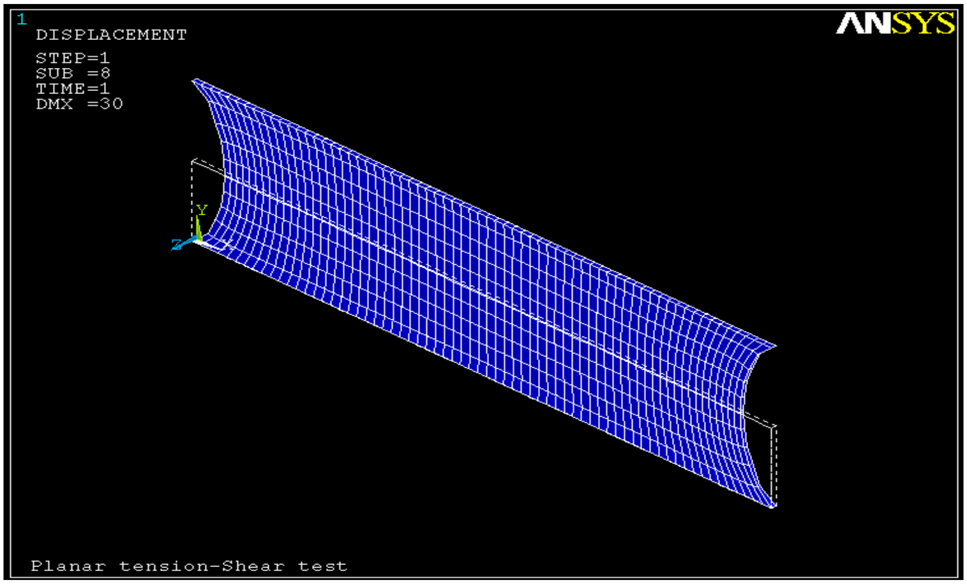

Figure 75. This wide specimen model has free horizontal edges, and fixed bottom. Top plane can only move vertically. Initial grip separation is 30mm. Shown at 100% strain.

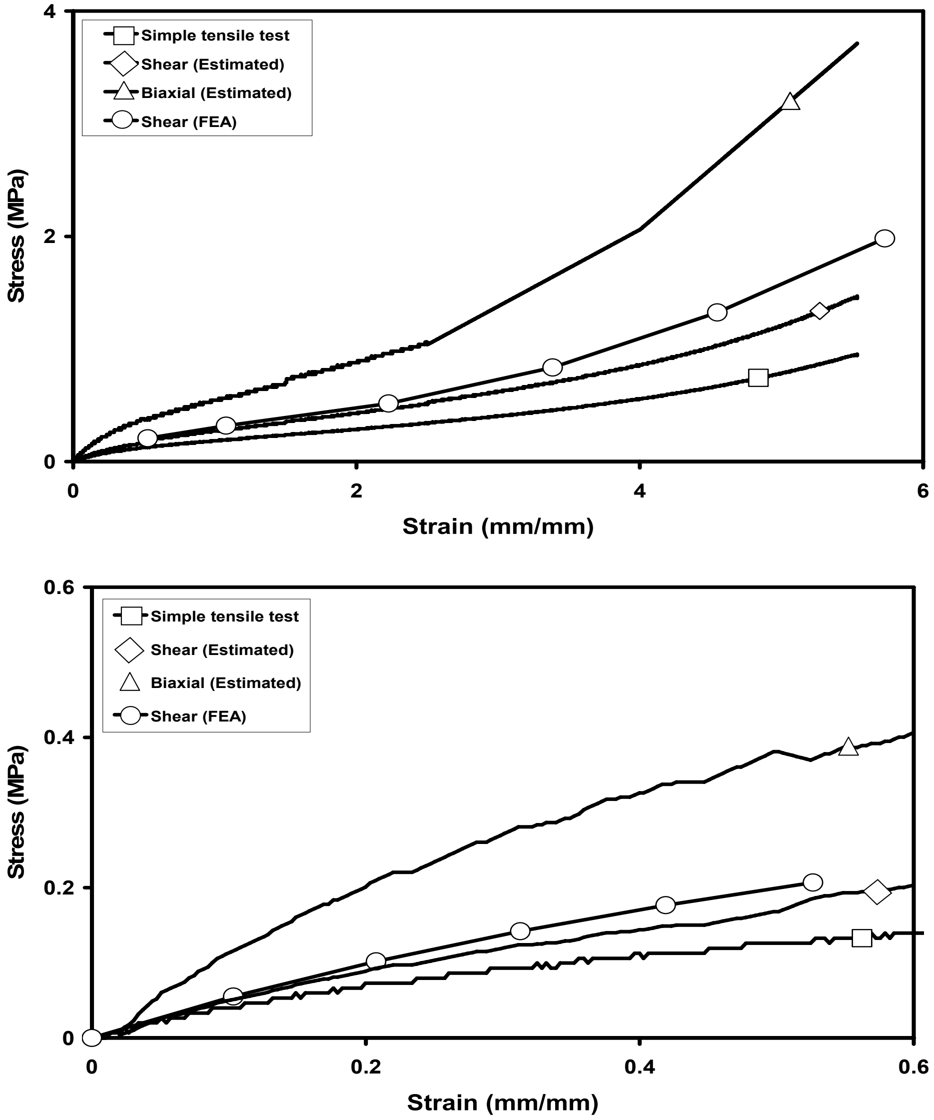

Figure 76. The planar tension simulation provides a good estimate of the experiment response up to 200 percent strain. The top image shows the full analysis and the bottom image provides a detailed view up to 60% strain.

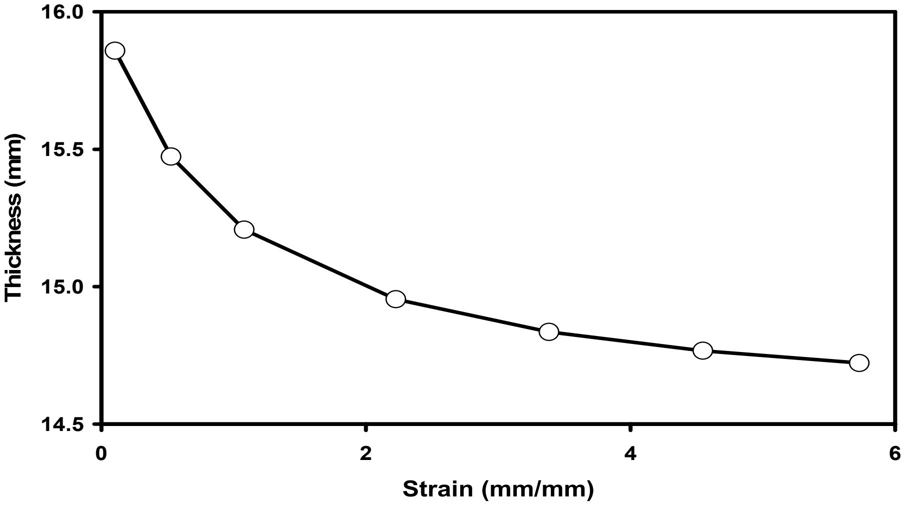

Figure 77. The thickness change calculated from the strain in Figure 76 shows a decaying response as the strain increases.

Figure 76 shows FEA simulation results, and Figure 77 shows thickness change in the specimen's middle section. The theoretical values come from the relationship described in section 2.5.2. The FEA and theoretical value of thickness stretch appear in Figure 78, and show good agreement up to 50% vertical extensions.

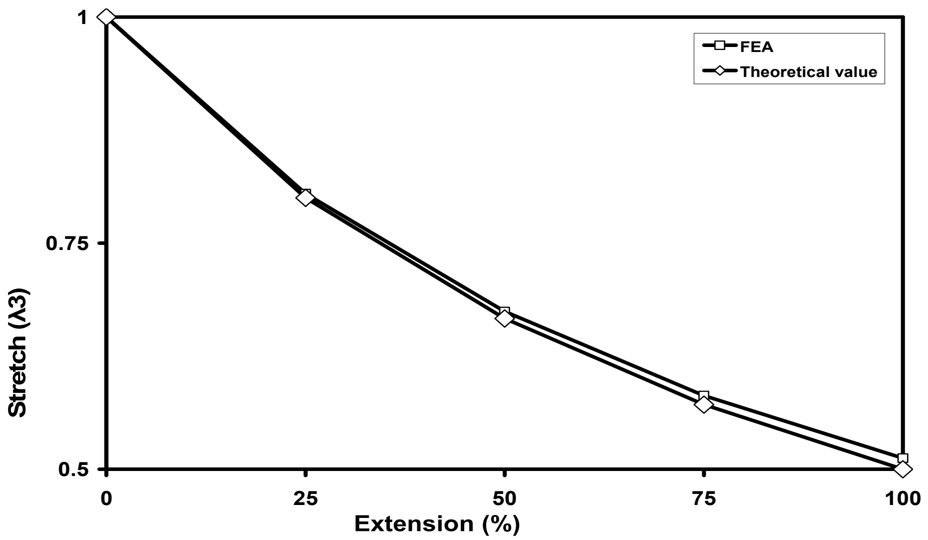

Figure 78. If the FEA model with Ogden parameters does a good job predicting the response, the theoretical and FEA thickness stretches must be similar. The results show good agreement to 50% vertical extensions.

Another boundary condition imposed on the FEA planar tension model keeps left and right edges from moving horizontally; Figure 79 shows this condition. This forces ideal planar tension conditions throughout the model. The results tell us whether the model with free left and right edges—and therefore the physical specimen—is the right size to provide good planar tension data.

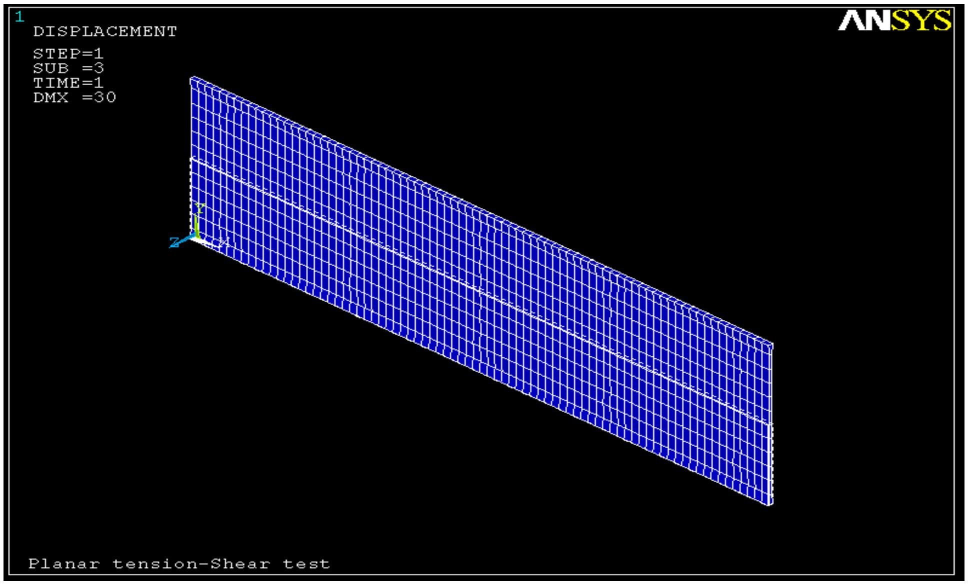

Figure 79. This model has boundary conditions applied to the left and right sides. Because the left and right edges cannot move horizontally, planar tension conditions exist everywhere. Other boundary conditions are same as in Figure 75.

As a conclusion from Figure 80, the FEA model overpredicts with guessed shear curve. As shown in the next pages, free edge condition is more similar to the real test deformation behavior, and also FEA simulation shows it is close to the guessed shear test.

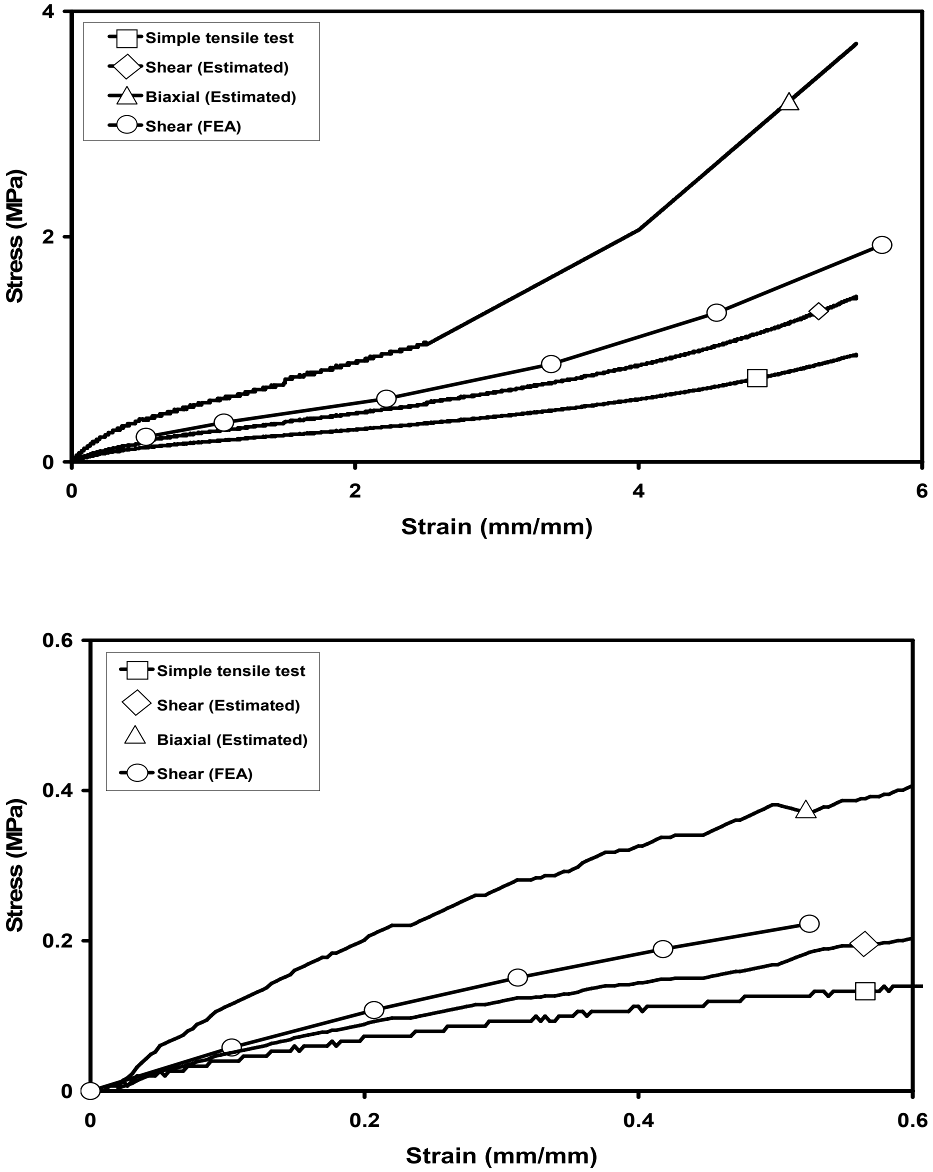

Figure 80. FEA simulation result according to the model in Figure 79 shows that it overpredicts compared to the free edge model in Figure 75.

One experimental finding is that the edge effect in the present planar tension specimen is significant. Figure 81 shows the free-edge curvature during an experiment. An FEA model with periodic boundary condition on the left and right edges represents an infinite model. Figure 82 shows a narrow model with these boundary conditions. As physical specimens become narrow, the center region that has λ_2 stretch at 1.0 is too thin. Most of the stress occurs within edge effect and does not contribute to the shear stress.

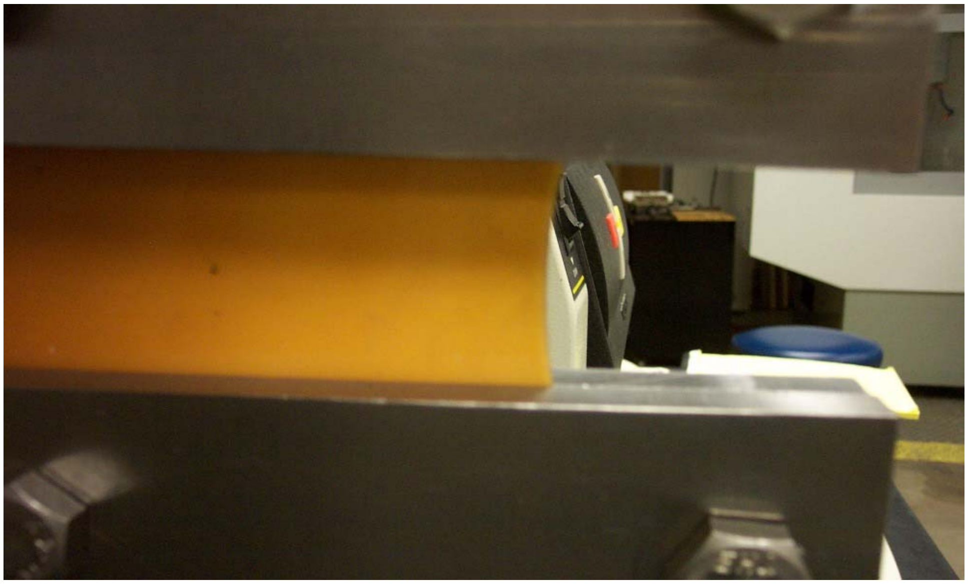

Figure 81. The edge is bow-shape as predicted by FEA (in Figure 75).

As a conclusion about the difference between bowed-edge and ideal plane strain condition, as in Figure 83, the difference of stresses between an infinite model and 10:1 model is 4% at 100% deformation. The difference between an infinite model and 6.667:1 model rises to 6.17%. Therefore, we can conclude the shear stress in a 7.2:1 model, which matched the present physical specimens made from 1035 resin, will be at least 4~6.17% low.

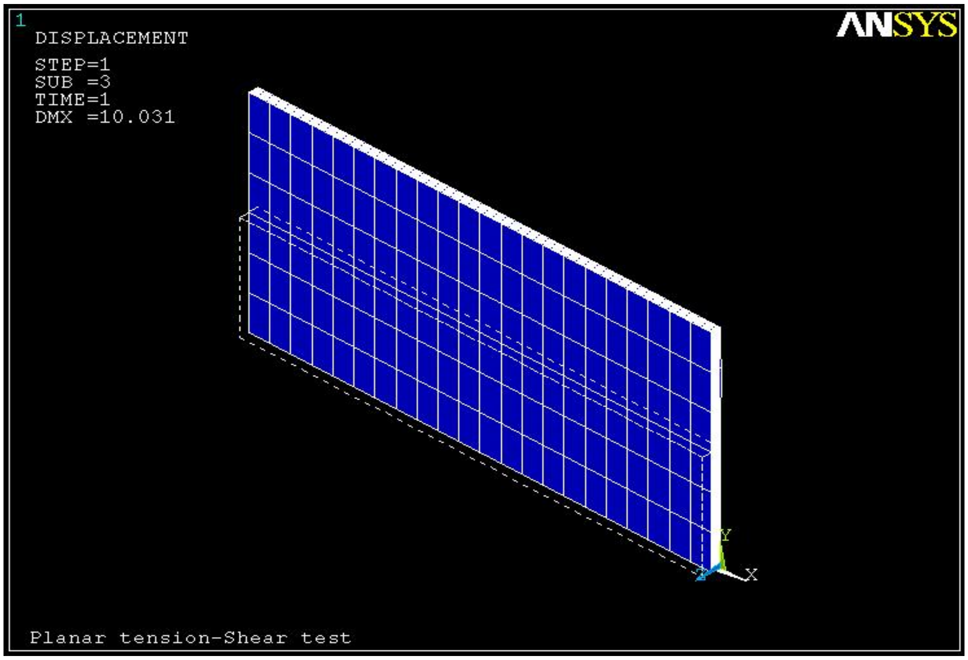

Figure 82. Periodic boundary conditions were imposed on left & right edges of the quarter planar-tension model to check the free-edge effect on shear stress.

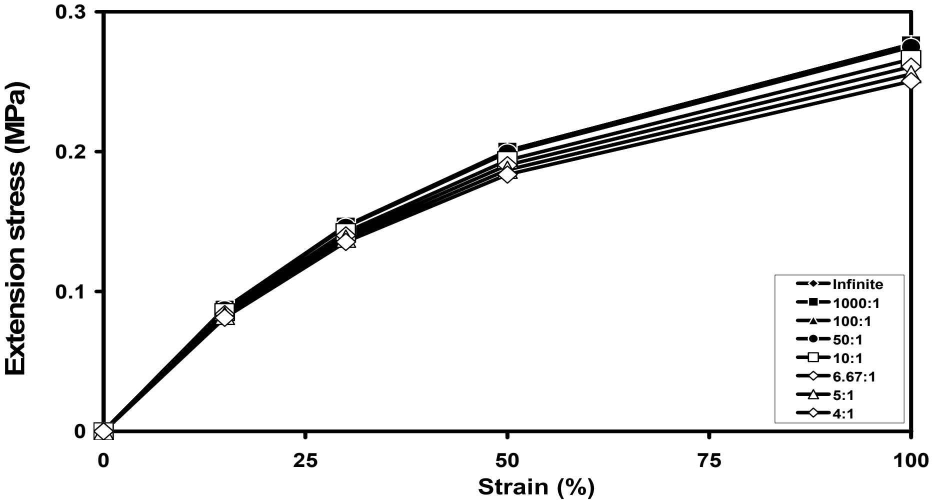

Figure 83. The FEA simulation for stress vs. strain of various aspect ratio specimens is shown. The stress error between an infinite model and a 10:1 model is 4%. The 6.67:1 model has stress 6.17% lower than the ideal condition.

5.1.3.3 Biaxial Extension Test

The FEA equi-biaxial extension test used the same specimen size from ref. [54-56]; Figure 84 shows this specimen. The gripped regions—shown as grey color in Figure 84—extend with equal strains.

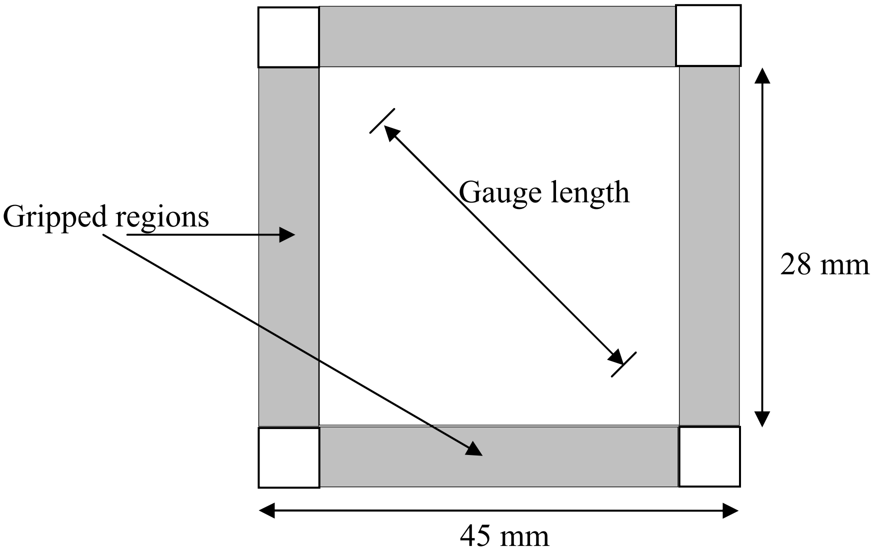

Figure 84. Schematic biaxial test specimen diagram shows key parameters for the test (after [56]).

In conclusion, FEA simulation overpredicts equi-biaxial extension stresses (Figure 85 and Figure 86).

The thickness changes are also checked as in Figure 87, but as in Figure 88, thickness change estimated by FEA and theoretical values are not matched well.

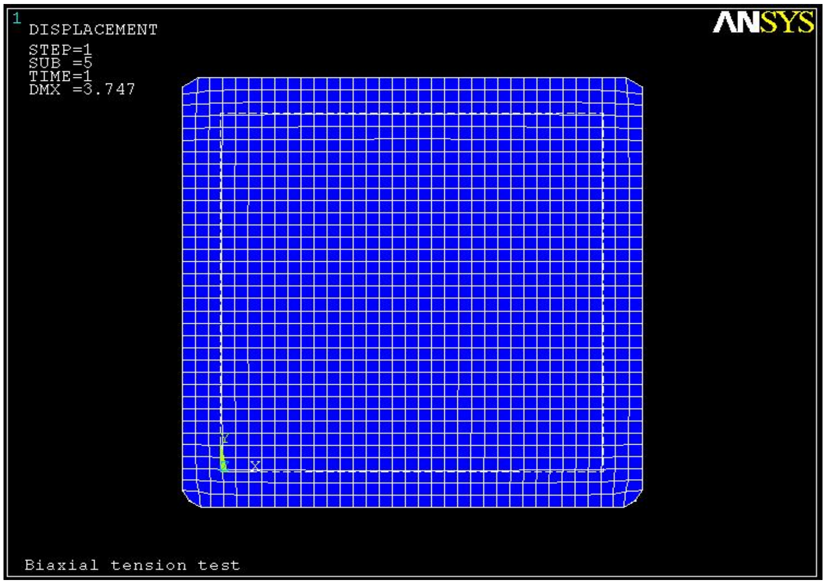

Figure 85. FEA simulation shows 10% deformed equi-biaxial extension specimen.

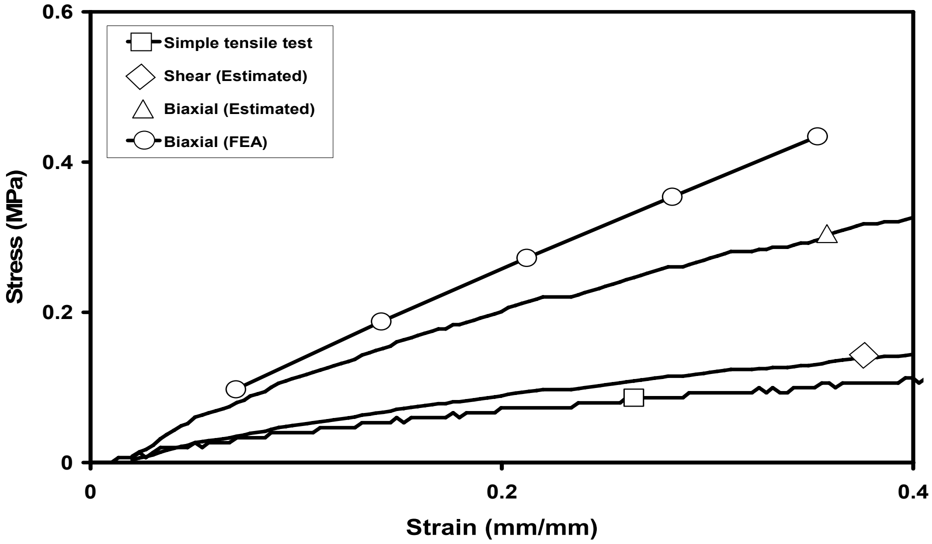

Figure 86. FEA simulation over predicts the stress in the equi-biaxial test.

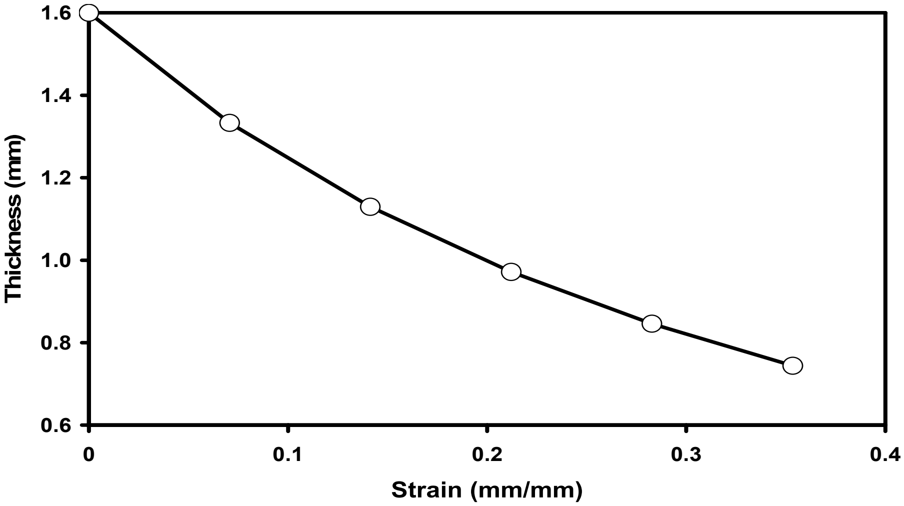

Figure 87. Thickness change from simulating the equi-biaxial extension test is shown. This result was used to estimate thickness change in Figure 88.

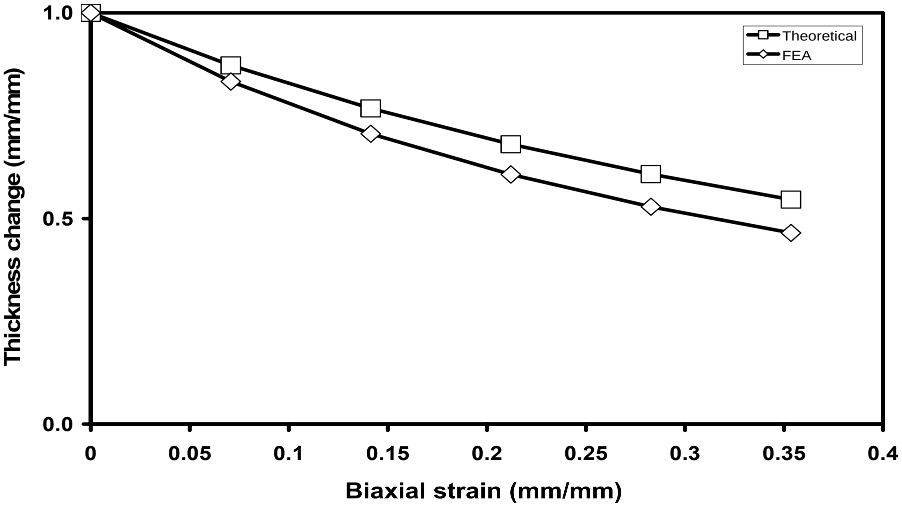

Figure 88. The estimated strains in thickness show the differences between theoretical and FEA values are significant. The error between theoretical and FEA values at 7% biaxial strain is 4.48%, and at 35% strain is 14.8%.

5.1.3.4 Uniaxial Compression Test

According to ref. [95], uniaxial compression is equivalent to equi-biaxial tension for incompressible materials, and the conversion relationship is described in Section 2.5.4. For the uniaxial compression test the top and bottom specimen surfaces are lubricated to reduce or eliminate shear deformation. Then this test result can be converted into biaxial extension test. If the top and bottom surfaces are not lubricated, this test is not equivalent to biaxial extension.

This FEA simulation (Figure 89) includes fixed (Figure 90) and lubricated surfaces (Figure 91) to check whether the compression test can approximate the equi-biaxial extension test.

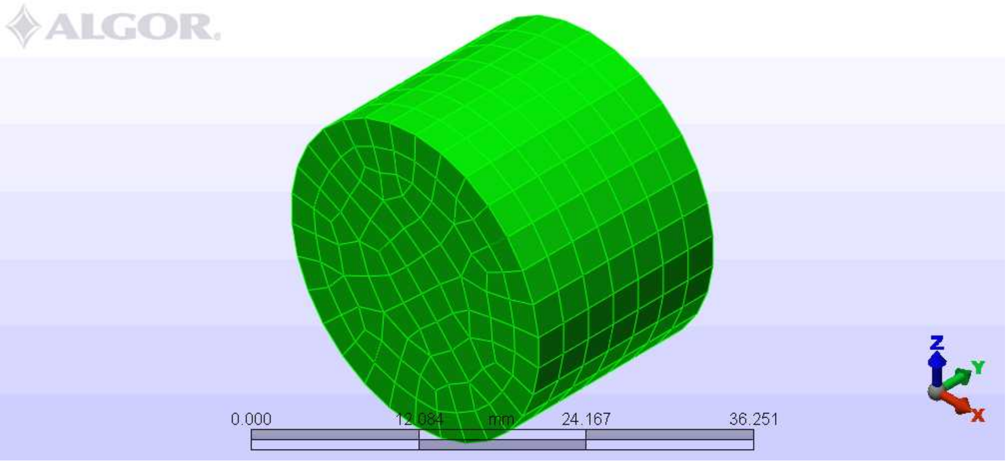

Figure 89. FEA model is imported from Algor®. Specimen size is: 25.3mm diameter X 17.8mm thickness

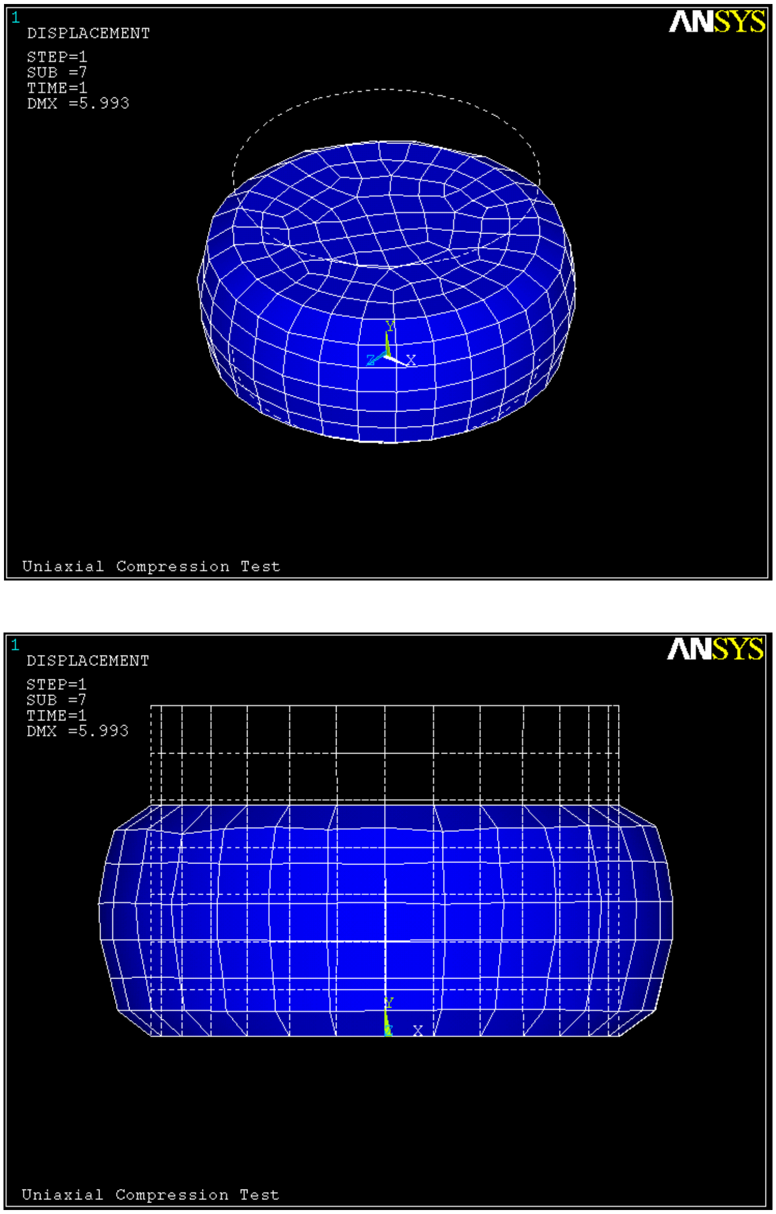

Figure 90. FEA simulation shows 30% compression strains for fixed boundary conditions.

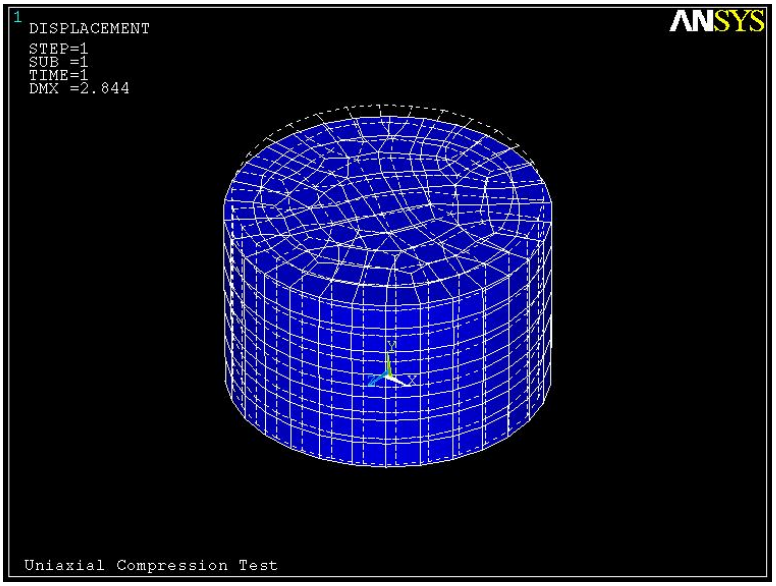

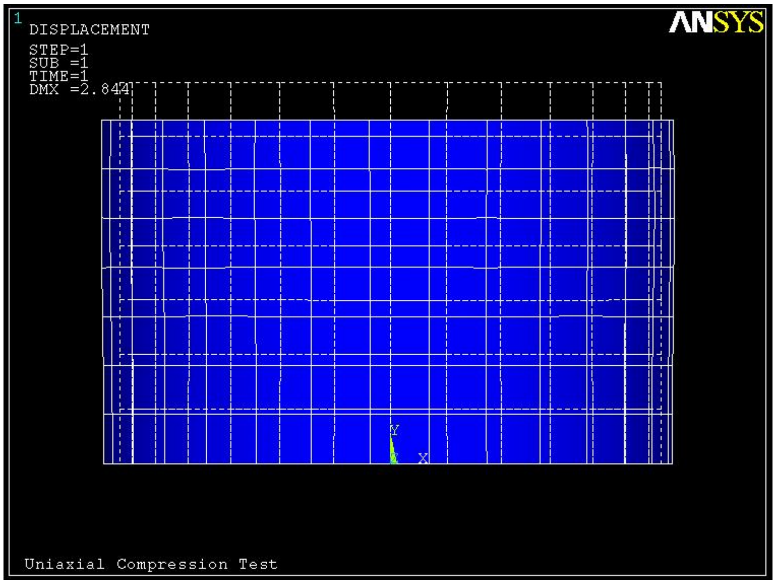

Figure 91. FEA simulation shows 10% compression strains for lubricated surfaces.

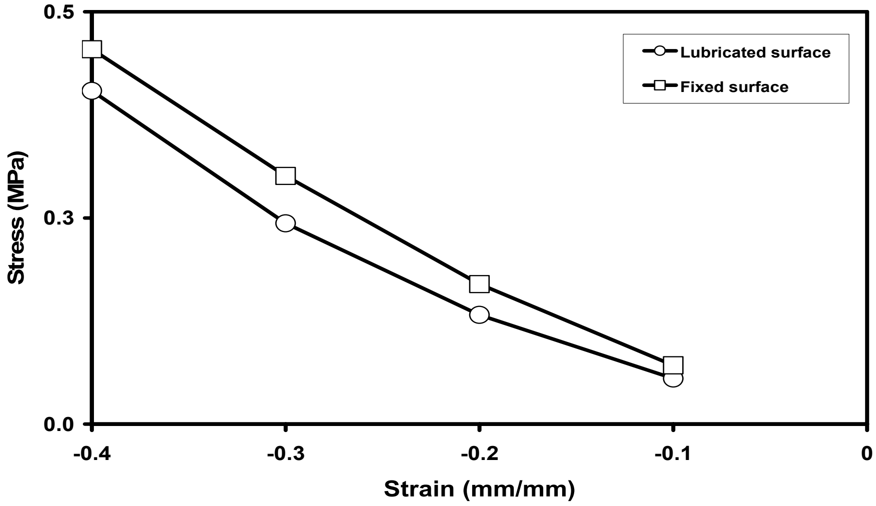

Figure 92. Simulated compression test shows that non-lubricated surfaces produce significant error in an experiment that must stand in for biaxial extension.

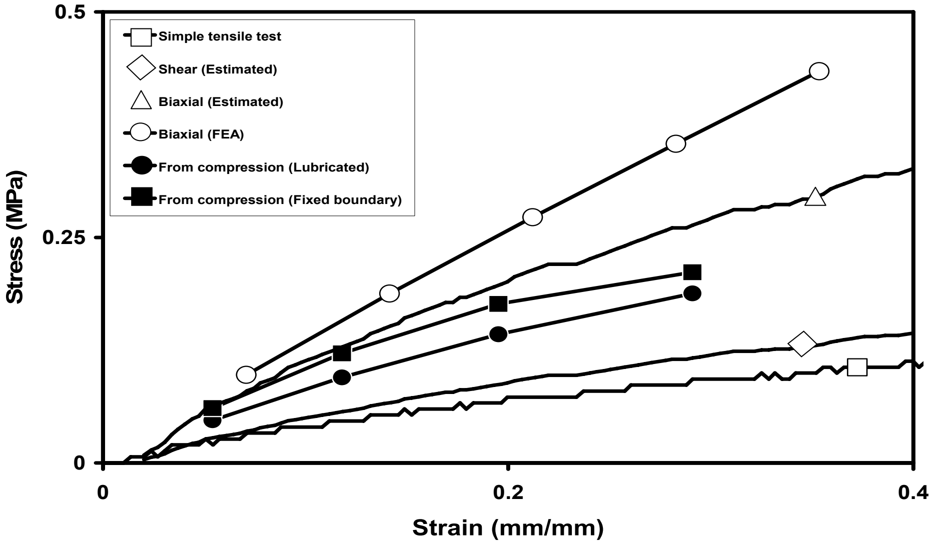

Figure 93. Results from compress test are converted to equi-biaxial strains and stresses. It shows biaxial test from lubricated compression test is matched until only 10% strains, while biaxial test from fixed compression test is not matched with guessed biaxial test curve.

5.1.3.5 Modified Hyperelastic Model for Biaxial Tension and Uniaxial Compression Test

Since simulated biaxial test shown in Figure 92 and Figure 93 did not match well with the estimated biaxial curve, the biaxial test curve was modified to the new estimate shown in Figure 94. This new biaxial curve shows better agreement with the typical elastomer test data set in Figure 70.

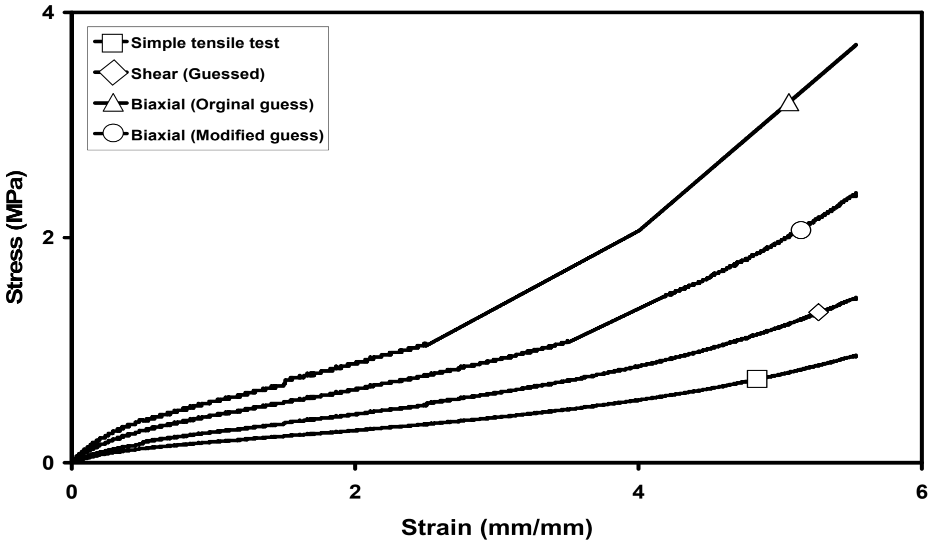

Figure 94. Modified guessed biaxial curve is lower than the first estimate.

The curve fitting software found new Ogden constants. Simple tensile test data, “originally guessed” shear test based on simple tensile data, and biaxial (modified guess) curves are used for curve fitting.

$$\mu_1=3.6567,\ \mu_2=-0.0228219,\ \mu_3=0.00558044 \text{ MPa}$$

$$\alpha_1=0.0841536,\ \alpha_2=-1.5232,\ \alpha_3=3.77668$$

Using new Ogden constants, commercial ANSYS® software performed 3 FEA simulation sets for these hyperelastic tests: biaxial extension, uniaxial compression with fixed boundary conditions, and uniaxial compression with lubricated surfaces.

The FEA simulation models and boundary conditions are same as before. Figure 95 shows the result. Biaxial test data calculated from lubricated compression test shows a good match with the guessed biaxial test.

However, the simulated biaxial test and biaxial data calculated from dry surface compression overpredict the stress. Figure 95 shows these results.

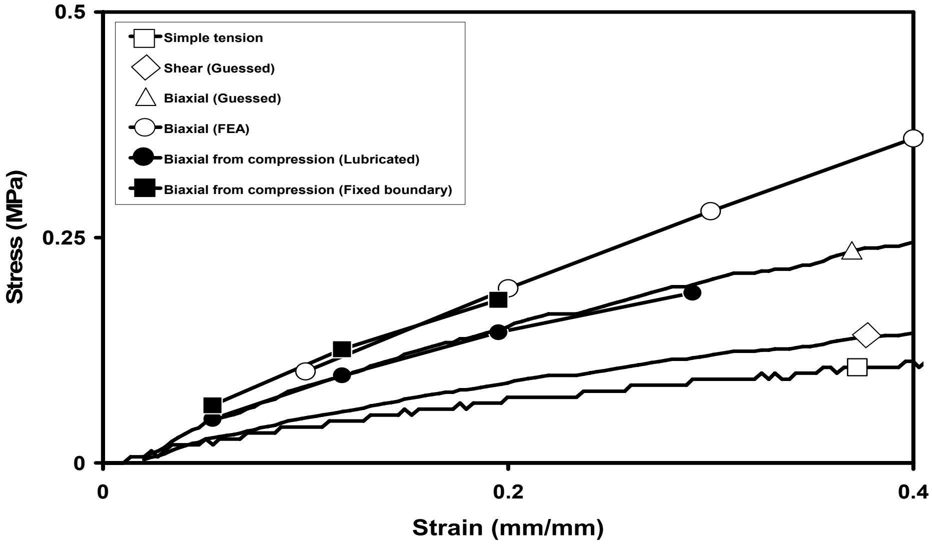

Figure 95. FEA simulation results with modified biaxial curve.
The result shows biaxial data calculated from compression (lubricated) has good match with the guessed curve, while biaxial data (FEA) and biaxial from compression (fixed boundary) overpredict results.

5.1.3.6 Simulation of Biaxial Extension Test using Circular Specimen

For a complementary purpose, a new circular model from Axel paper [58] has been applied to new FEA simulation for biaxial extension test (Figure 96).

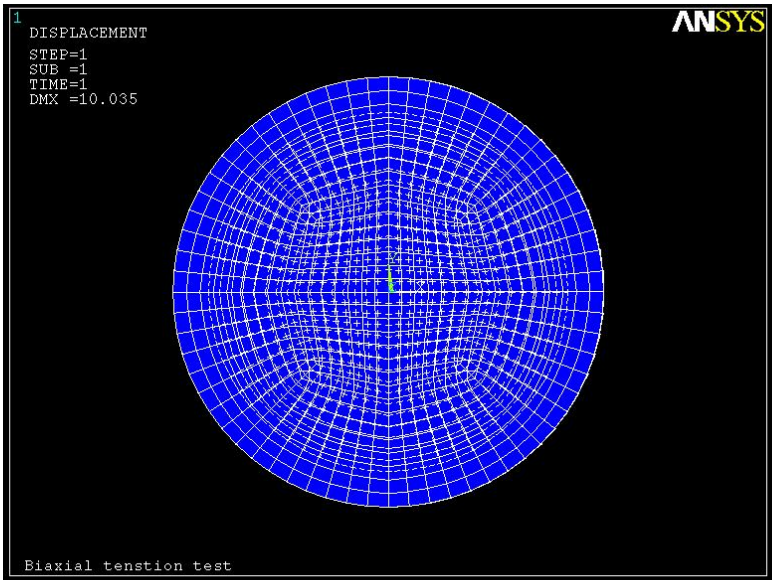

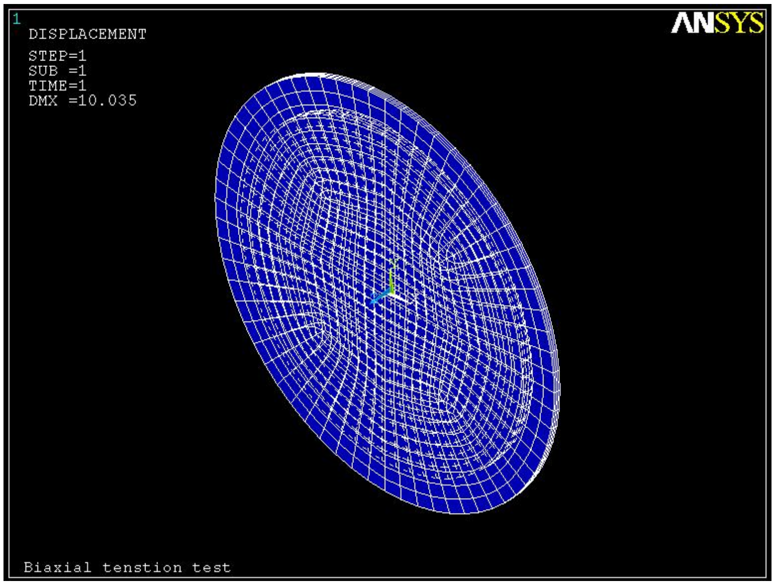

Figure 96. The biaxial tension model is a 50mm radius disk that is 2.8mm thick. This image shows the model at 20% deformation.

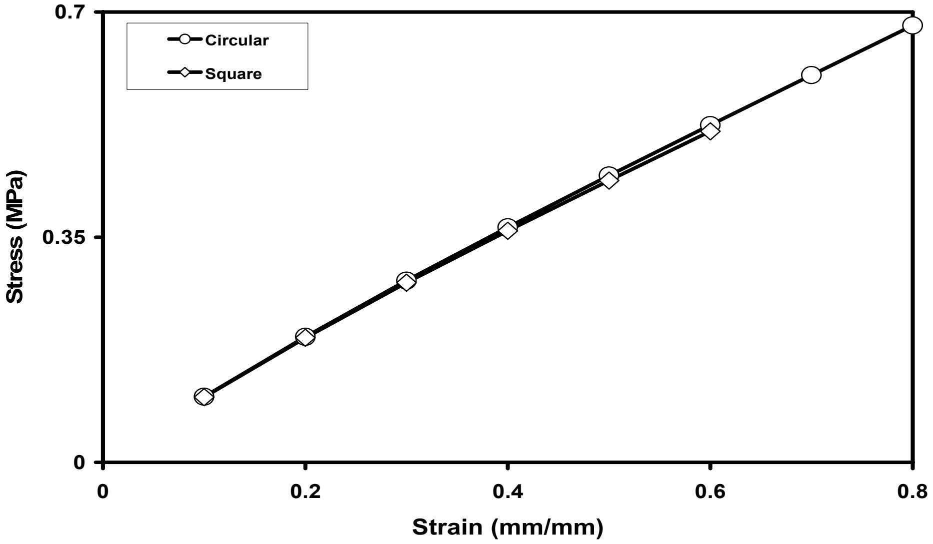

Figure 97. The simulation results for biaxial tension test using circular and square model. The result shows no difference between two models.

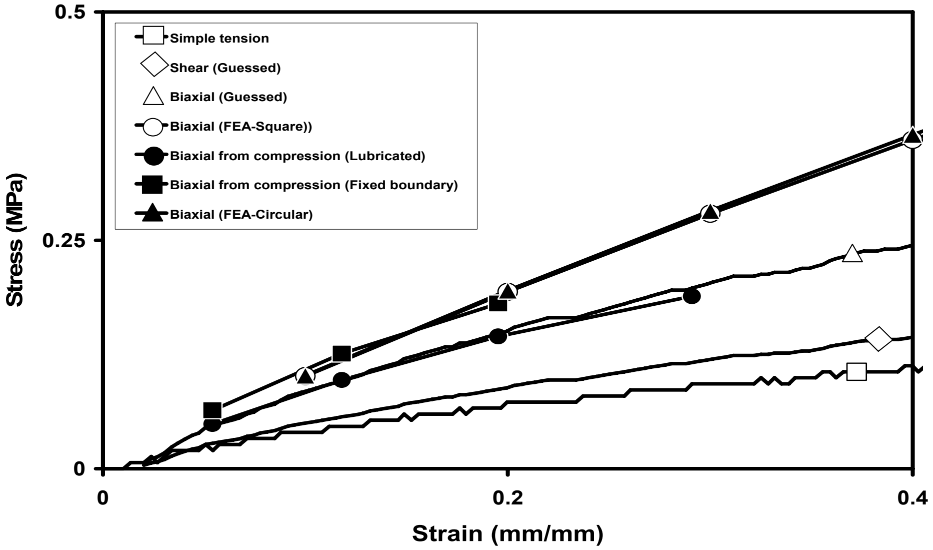

Figure 98. The FEA simulation over-predicts the biaxial extension stresses, that is, the model does not return the biaxial extension behavior supplied to the software.

From the simulation results so far, biaxial test simulation from circular specimen (Figure 97 and Figure 98) still overestimate the biaxial stresses over given biaxial strains.

Then the square model from ref. [54-56] has been updated with the whole grip region included (Figure 99) while the last square model only shows the inside square's deformation.

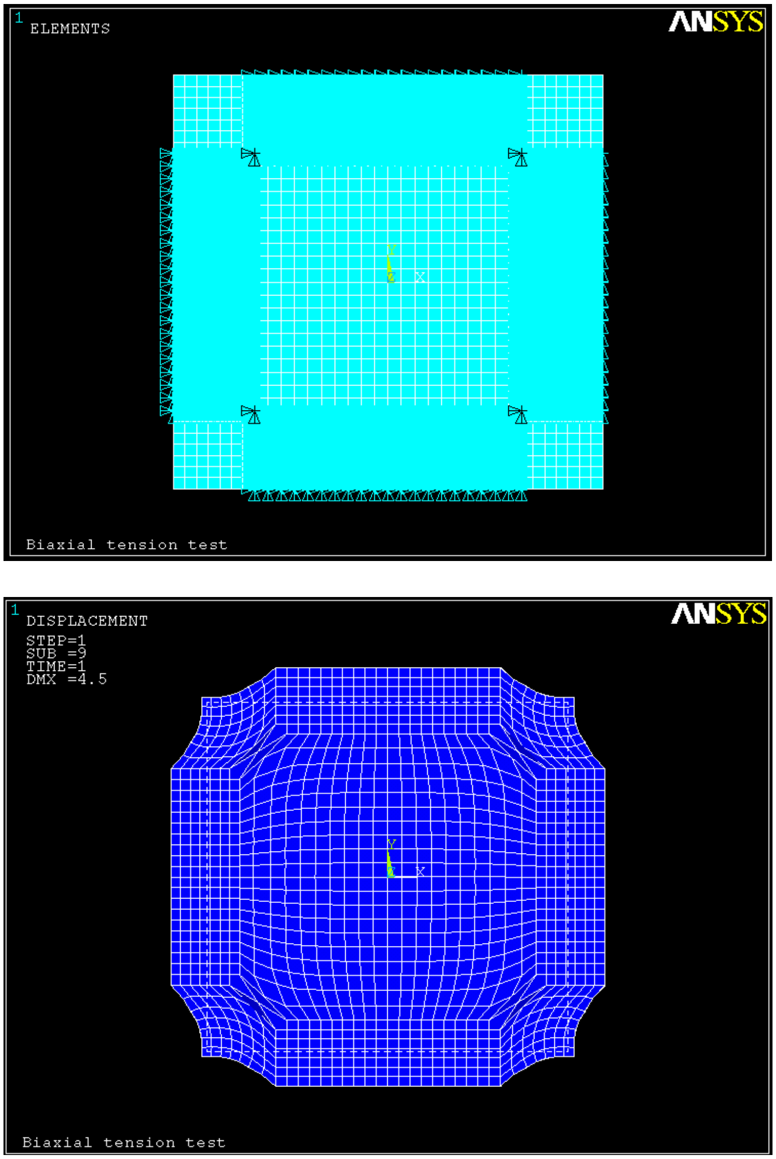

Figure 99. Updated biaxial FEA model using ANSYS shows the model at left and the model at 20% strain at right. 1X magnified.

There is the region, near the specimen centroid, where horizontal and vertical stresses are identical. Figure 100 and Figure 101 shows the results from FEA simulation.

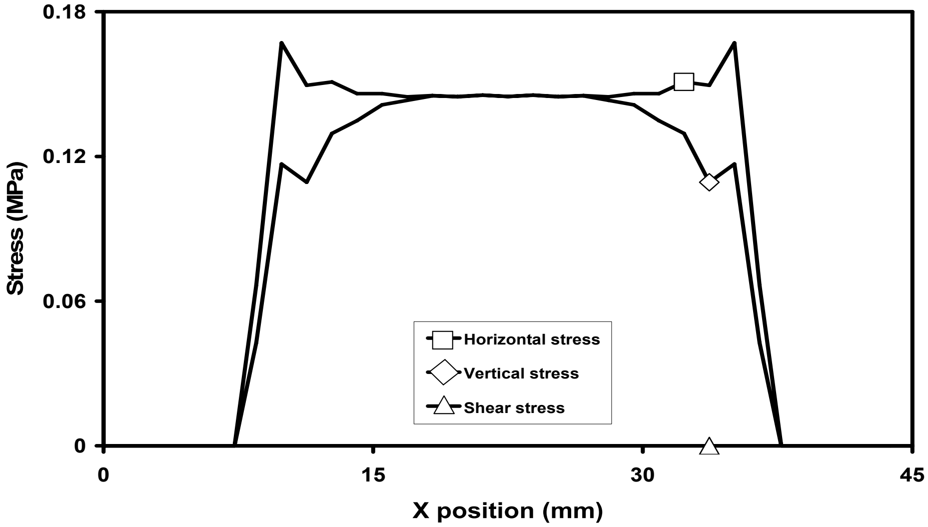

Figure 100. Strain distribution in the center of the square biaxial specimen shows that only data in the center is in equal biaxial extension. Result shows stresses from 15mm to 30mm are identical (at 10% strain).

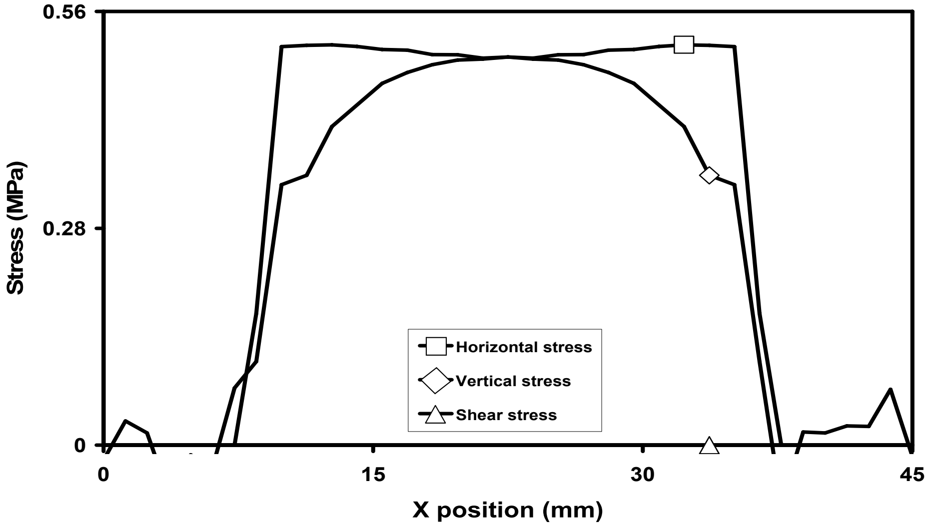

Figure 101. As biaxial strain goes large, the identical region becomes smaller (at 40% strain shown).

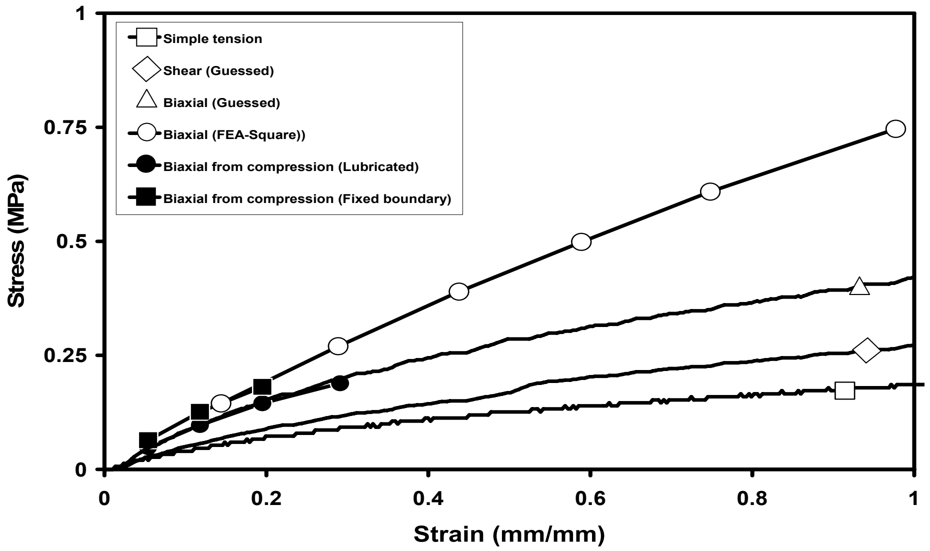

Figure 102. FEA simulation result using updated biaxial extension specimen still overpredict the biaxial stresses over given biaxial strain.

As shown in Figure 102, the simulation results in this work by commercial FEA software ANSYS®, and references [54-56] overestimate the biaxial stresses. As a conclusion, with these identical results, the biaxial test calculated from compression test will match better with the guessed curve.

5.1.4 Hyperelastic material characterization and simulation from 1035 resin

The 1035 resin characterization used simple tensile test data from Section 5.1.1.2, planar tension-pure shear test data from Section 5.1.2, and guessed biaxial extension data. Section 5.1.2 showed planar tension test data is equivalent to pure shear data.

The 4th order Ogden constants came from curvefitting software in ANSYS®. FEA simulations showing simple tensile, planar tension-pure shear, and lubricated compression equi-biaxial performance must return the same Ogden constants to prove that the data is consistent. The applicable stress/strain limits for the Ogden constants are discussed.

5.1.4.1 Hyperelastic Curve Set from 1035 Resin Tests

New hyperelastic test curves were prepared as Figure 103 shows. The simple tensile test curve is from Ewumi's data [92], the pure shear curve is from the section 5.1.2, and biaxial curve is estimated from from pure shear curve. This curve set is different from typical elastomer stress-strain set in Figure 104.

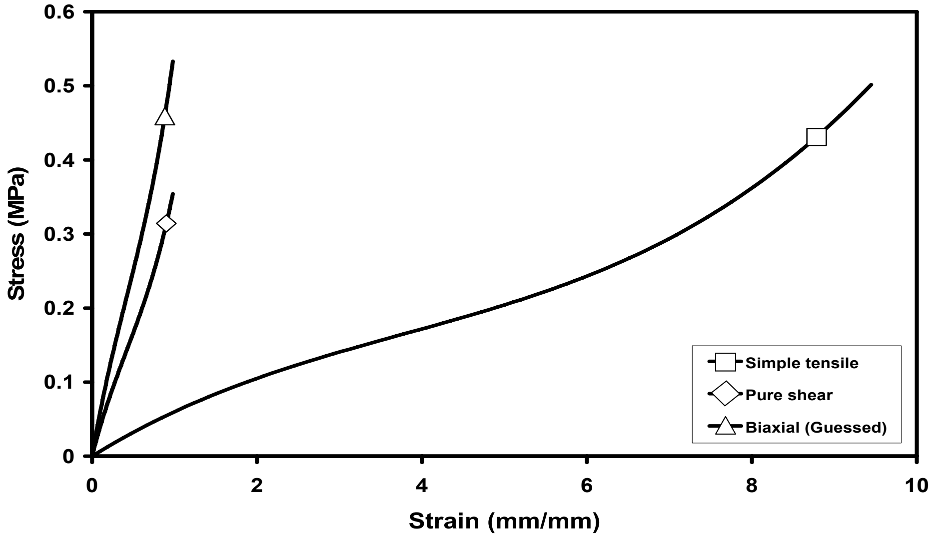

Figure 103. Hyperelastic curves for 1035 resin are shown. Simple tensile test data and pure shear data from planar tension test are used. Biaxial curve is guessed based on pure shear test data.

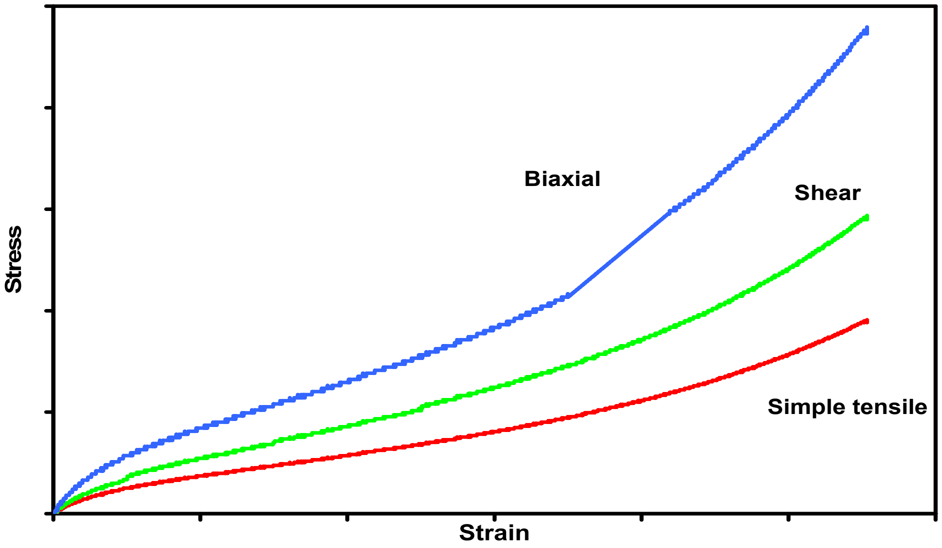

Figure 104. The curves above are different from typical elastomer stress-strain set (after ref. [94]) because the pure shear data only goes to 100% strain while simple tensile data goes more than 900% strain.

Commercial FEA software ANSYS® has a curvefitting software to find the material constants for hyperelastic models. For Ogden material, ANSYS® can find the 1st, 2nd , 3rd , or higher order material property. In this work, the 3rd, 4th, 5th, and 9th order constants are found by curvefitting, see Figure 105~Figure 108.

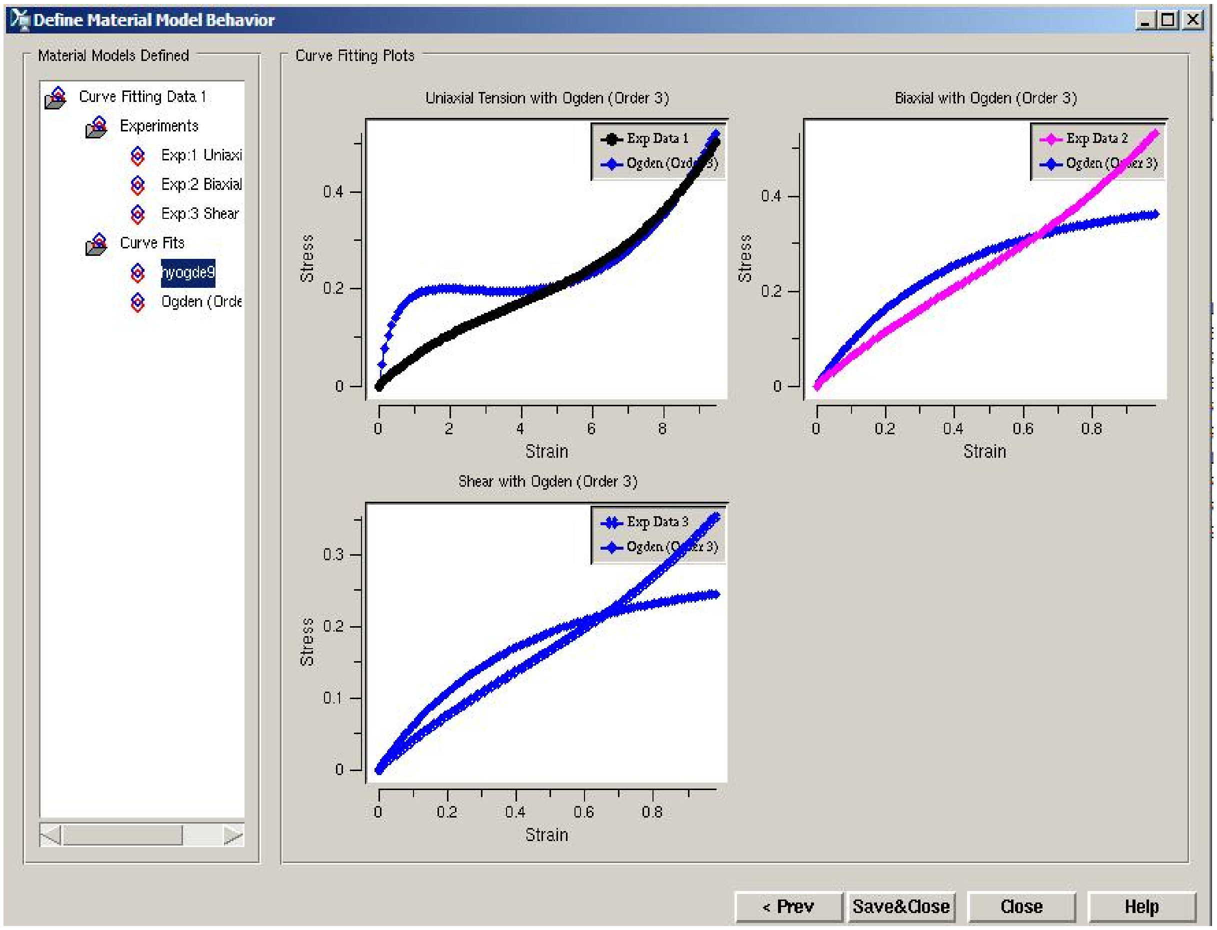

Figure 105. This captured image shows test results and fitted curve for the 3rd order Ogden constants from ANSYS® software.

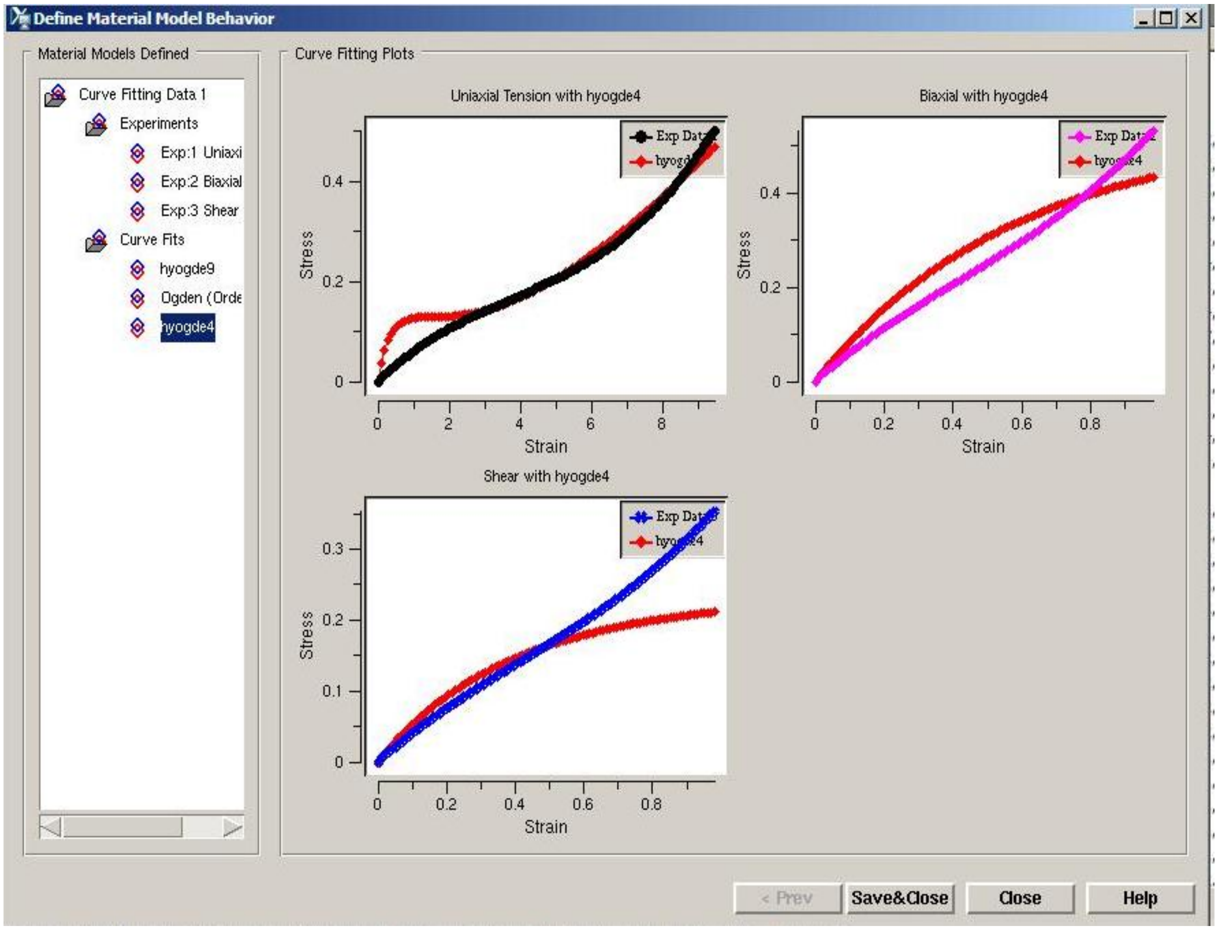

Figure 106. This captured image shows test results and fitted curve for the 4th order Ogden constants.

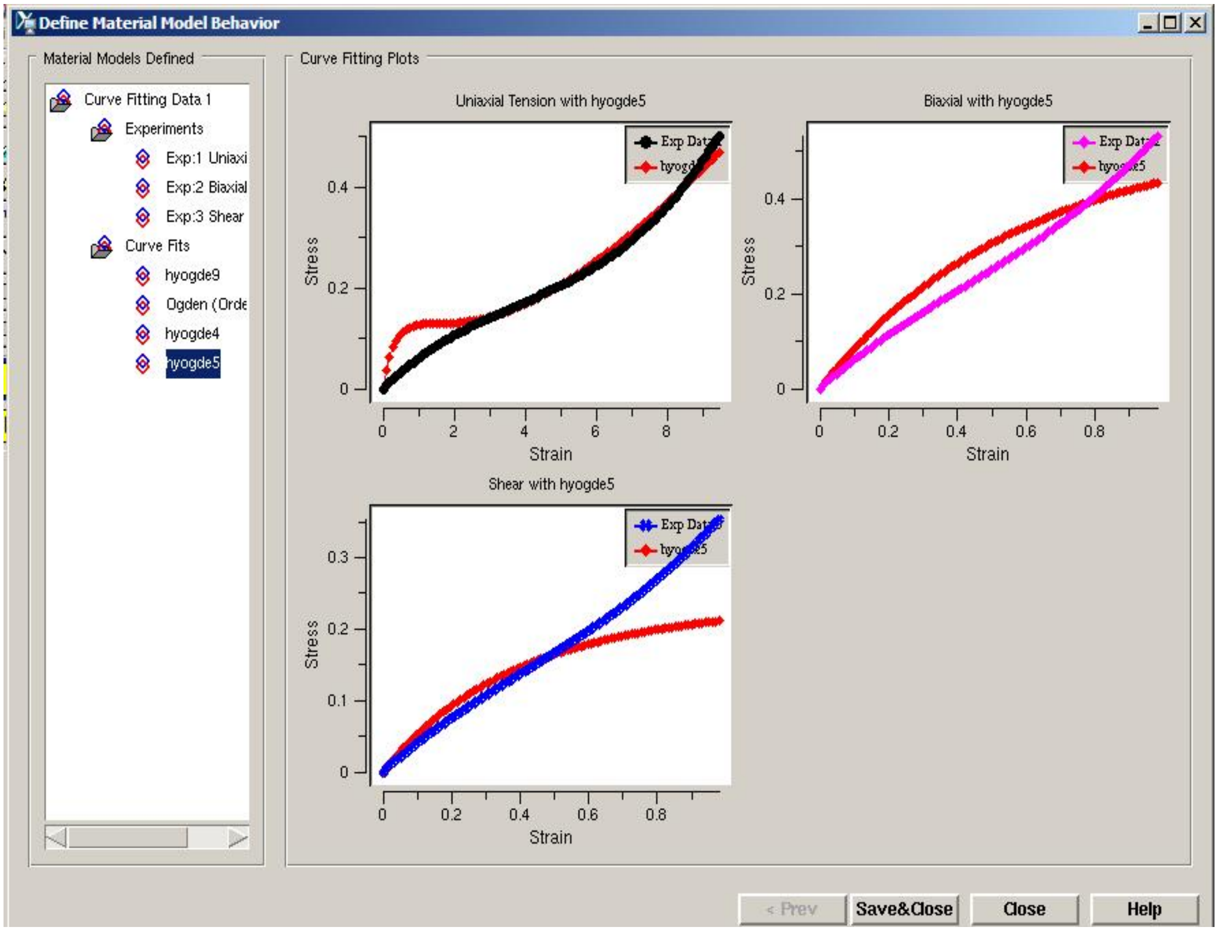

Figure 107. This captured image shows test results and fitted curve for the 5th order Ogden constants.

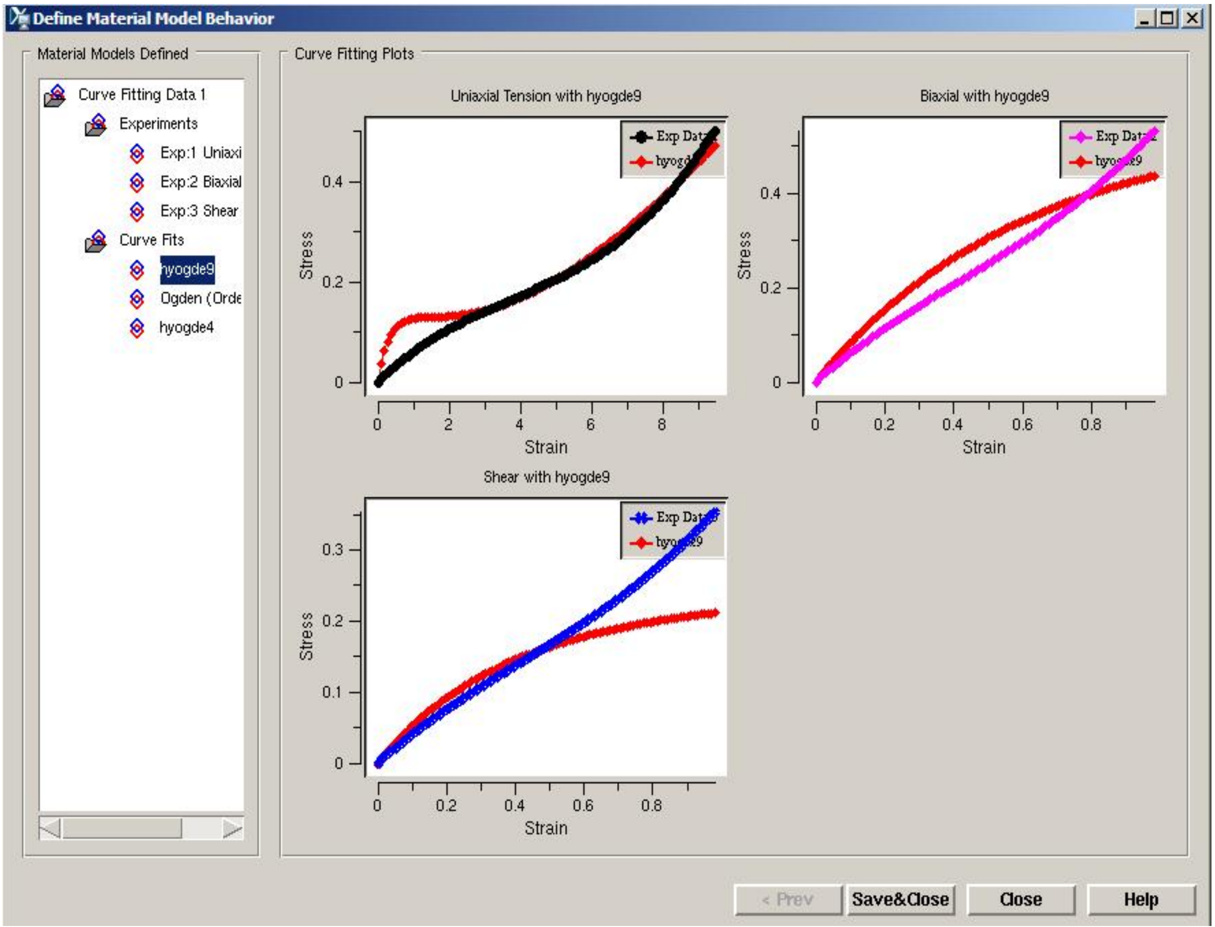

Figure 108. This captured image shows test results and fitted curve for the 9th order Ogden constants.

As shown in Figure 105~Figure 108, the curvefitting results for the 3rd order Ogden constants shows large overshoot in less than 300% strain in tensile test. The curvfitting for the 4th, 5th, and 9th Ogden constants shows similar results. Next, FEA simulations performed to check the simulation results match well with fitted curve or not.

FEA simulation using the 3^{rd} order Odgen constants for 1035 resin

As described before, commercial FEA software ANSYS® has the curvefitting algorithm for hyperelastic material properity. The 3^{rd} order Ogden constans found are

$$\mu_1=3.29407868918E\text{-}5,\ \ \mu_2=3.3208448391,\ \ \mu_3=3.49915865219\ \text{MPa}$$
$$\alpha_1=5.00737571163,\ \ \alpha_2=0.0517907194523,\ \ \alpha_3=0.0520713215461$$

FEA simulated simple tensile test, planar tension-pure shear test, and biaxial extension from lubricated compression test were performed to verify the 3^{rd} order Ogden constants. Figure 109, Figure 110, and Figure 111 show the simulation results.

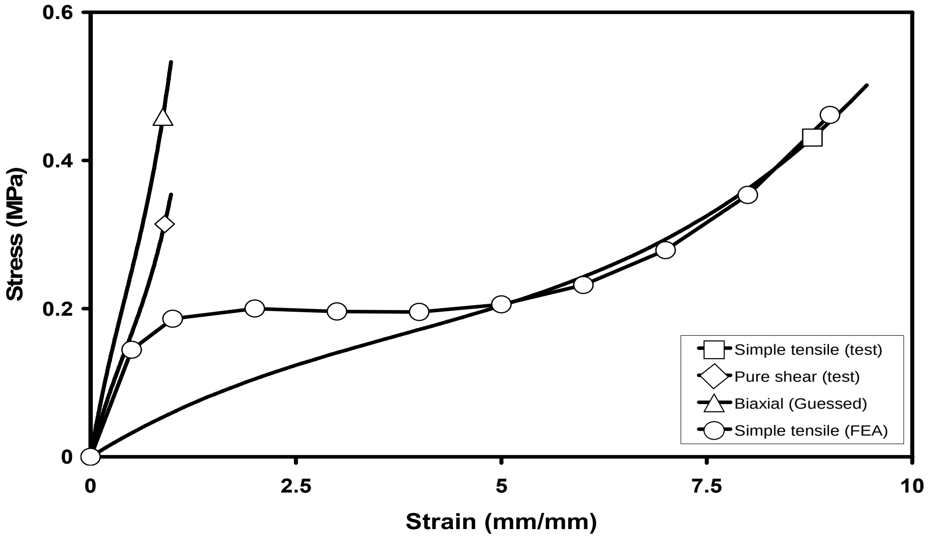

Figure 109. FEA simulated simple tensile test made with the 3^{rd} order Ogden constants is shown. The FEA results matches well with the data curve from Figure 105 for huge strains that are not likely in this analysis.

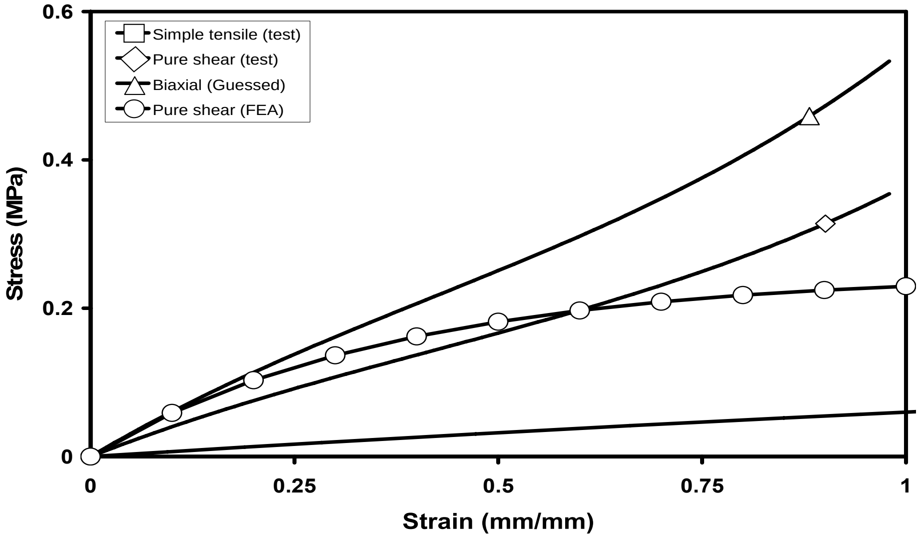

Figure 110. FEA simulated planar tension-pure shear test results with the 3rd order Ogden constants also has good match with data from Figure 105 for strain under 0.75.

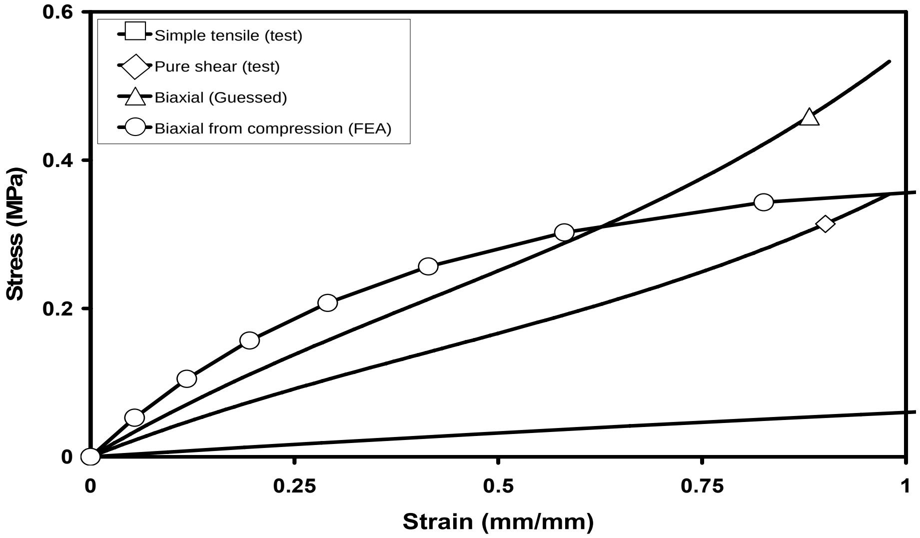

Figure 111. FEA compression test simulation results with 3rd order Ogden constants were converted to biaxial test and the data also shows good agreement with fitted curve.

As a conclusion, FEA simulations using the 3rd order Ogden constants shows good match with fitted curve by curvefitting software. Now this result is compared to the 4th order constants to decide what constants will be used, on the following page.

FEA simulation using the 4th order Odgen constants for 1035 resin

Commercial FEA software ANSYS® can find higher—4th or higher—order Odgen constants for hyperelastic material properity. The 4th order Ogden constans found are

μ_1= -3.80611293727, μ_2= 0.020180574353, μ_3= 7.9035829192, μ_4=7.93743654455MPa

α_1= 0.443685229869, α_2= 2.426861504, α_3= 0.122285224823, α_4=0.123151748913

Similar to the 3rd order constants case in previous pages, Simple tensile test, planar tension-pure shear test, and biaxial extension FEA simulations from lubricated compression test are performed to verify the 4th order Ogden constants, see Figure 112~Figure 114.

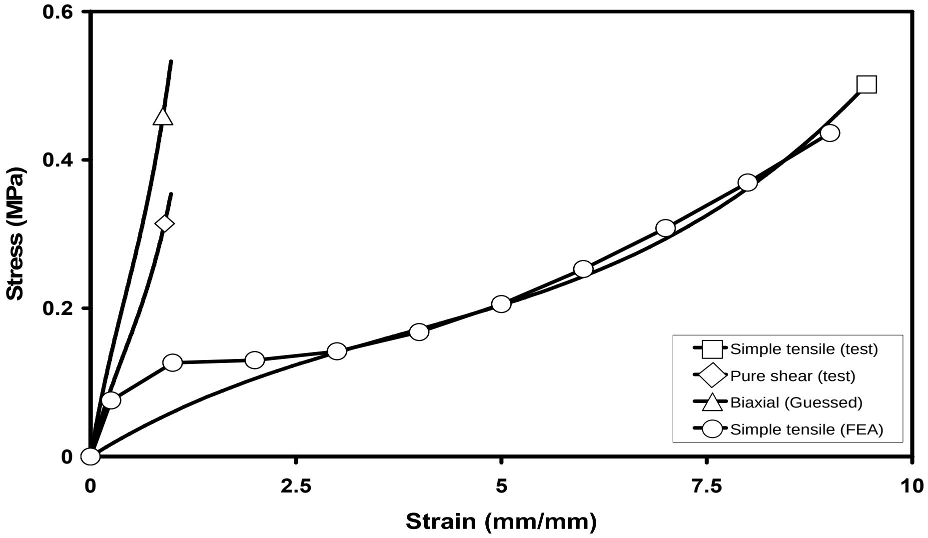

Figure 112. FEA simple tensile test simulation results with the 4th order Ogden constants shows the FEA results matches well with fitted curve in Figure 106.

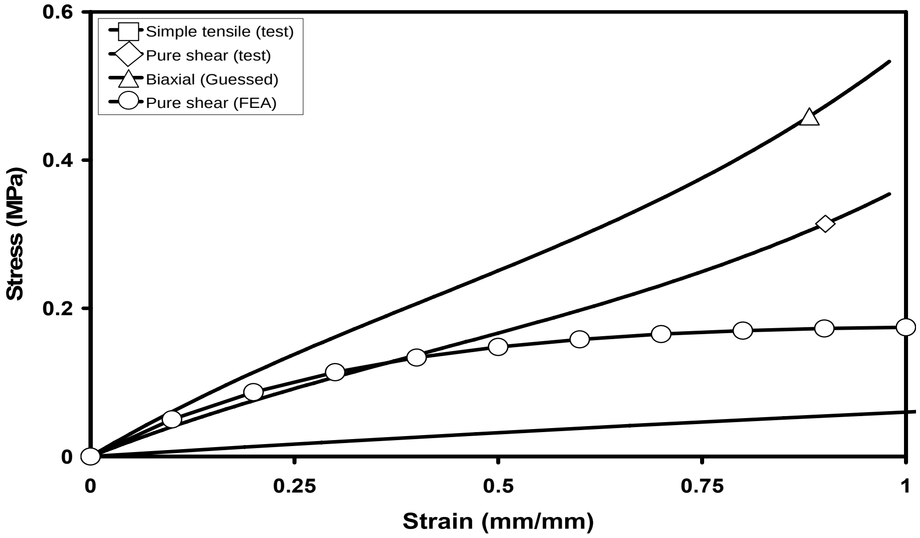

Figure 113. FEA simulation of planar tension-pure shear test results with the 4th order Ogden constants also shows good match with fitted curve in Figure 106.

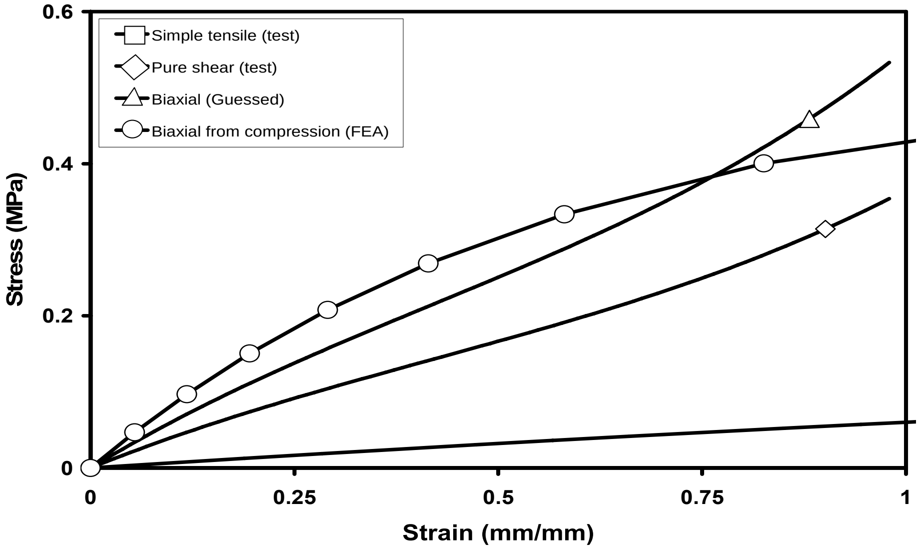

Figure 114. FEA simulation of compression test results with the 4th order Ogden constants were converted to biaxial test. The data also shows good agreement with fitted curve.

As stated in Chapter II, elastomer's complex and sensitive behavior makes it difficult to find the "near-perfect" model in for numerical and analytical investigations. But we still need to understand the chosen hyperelastic model's advantages and disadvantages to prevent unexpected error and to get the best results possible.

As a conclusion for hyperelastic material properties, the 3rd and 4th order Odgen constants matched well with fitted curve from ANSYS® software. It means we can get the expected results -almost same from curvefitting- from numerical simulations.

From the candidates, the 4th order Ogden constants are selected for shear actuator FEA simulation because they are closer to the test curves, and used for this research hereafter. However, one must keep in mind that this Ogden constant set, when it is used for FEA simulations, has "overshoot" between 0~200% deformation in simple tensile test. The large deformation region—higher than 300%—in simple tensile test shows good agreement with real test data.

Similarly, for the pure shear test, the 4th order Ogden constants matches well with real test data under 50% deformation. Because The shear actuator in this research shows less than 50% shear deformation, these constants are used for numerical simulation.

5.2 Behavior of Kevlar Fabric – Lens Element

Kevlar fabric lens element itself is an actuator, so actuator performance curve must be determined by the test. For tensile lens element test with Kevlar fabric, Fray check® has been used to maintain the fabric's integrity during the test (Figure 115). This test followed the procedure described in section 4.2.

Figure 115. Fray Check® used for Kevlar fabric to maintain the integrity of specimen during the test.

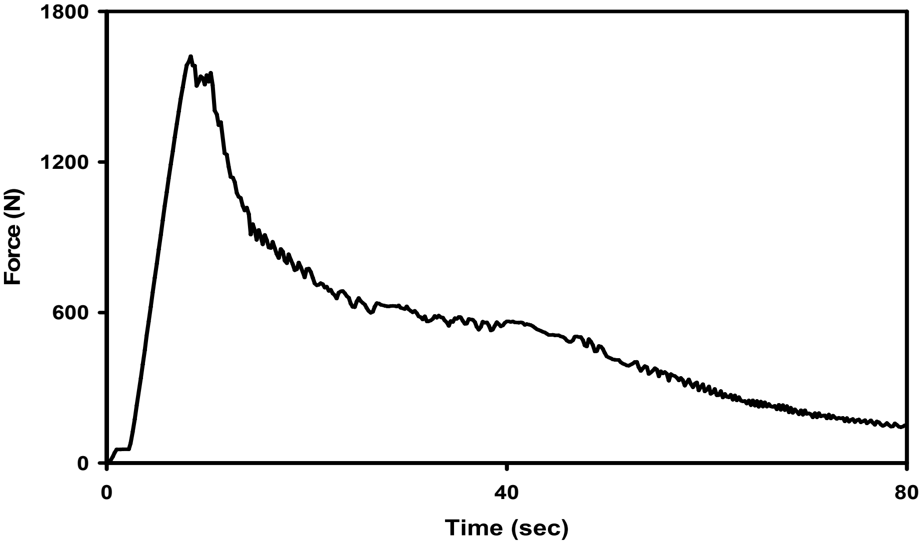

Figure 116. Force vs. time plot of single pull-out test of Kevlar fabric. 70% of the maximum force (1622.3 N) here is selected as the conservative force (1135.6 N) for tensile test of Kevlar fabric lens element.

Figure 116 and Figure 117 show force-time plot of Kevlar fabric and lens element, respectively. The result in Figure 118 shows nonlinear actuator characteristics.

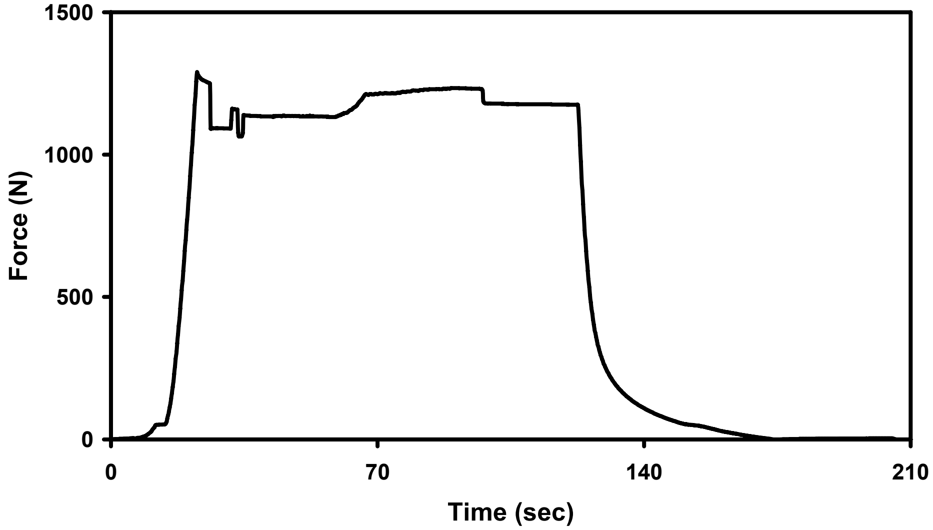

Figure 117. Force-time plot of lens element pressurized by 0.651 MPa (95 Psi) is shown as an example. Applied pressures to lens element are 0.069 MPa, 0.138 MPa. 0.345 MPa, and 0.651 MPa. After the tensile force reaches the conservative force (1135.6 N) from single pull out test in Figure 116, the crosshead movement stopped and actuated for each pressures, then maintained with same pressure and returned to original position. The down curves due to each pressures are showing the actuator performance chart in next figure.

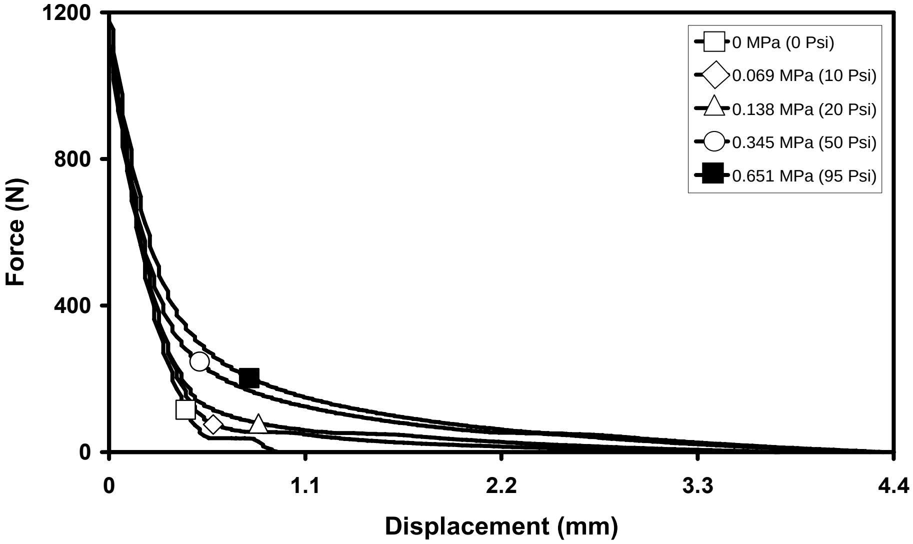

Figure 118. Force vs. displacement plot of Kevlar fabric lens element shows nonlinear actuator characteristics.

5.3 Experimental Evaluation of Shear Actuator Performance

After finished curing in the mold (in section 3.3.1), the single shear actuator is pressurized to check its free strain behavior. After that, it is bonded to an aluminum block. The peak shear strain is measured by applying various pressures.

5.3.1 Behavior of shear actuator when pressurized

As shown in Figure 119, and Figure 120, the pressurized single shear actuator shows rotating behavior before clamped to an aluminum block.

5.3.2 Pressure vs. free strain relationship

The shear actuator is bonded to the aluminum block. To measure the free shear strains, it is actuated up to 1.241 MPa (180 Psi). At this pressure, small leak occurred at the clamping area, so measurement was not performed at this pressure level. Below 1.241 MPa, there was almost no leak.

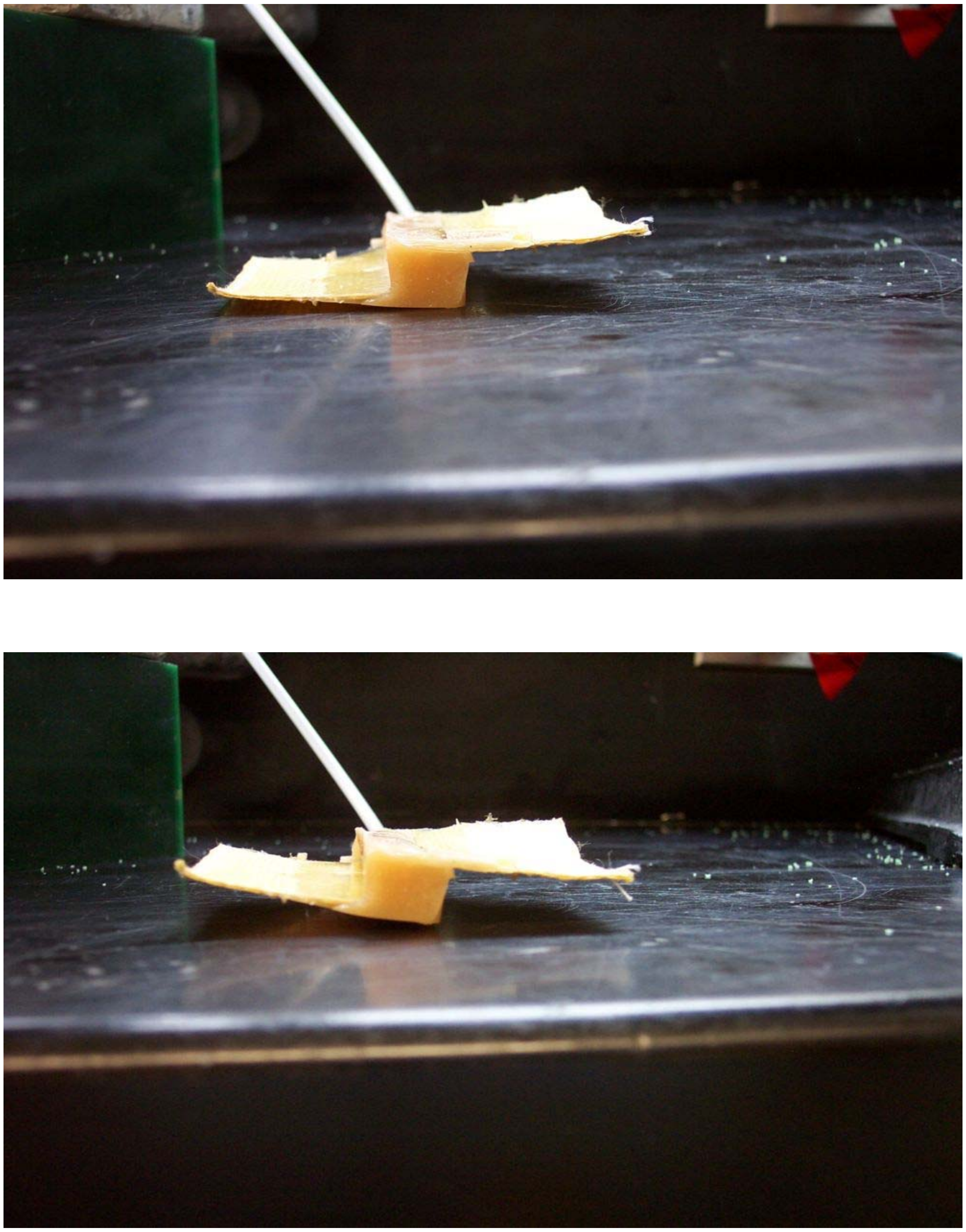

Figure 119. Without clamping bottom, the actuator shows rotating behavior. Front view of actuator; without pressure (top), pressurized (bottom)

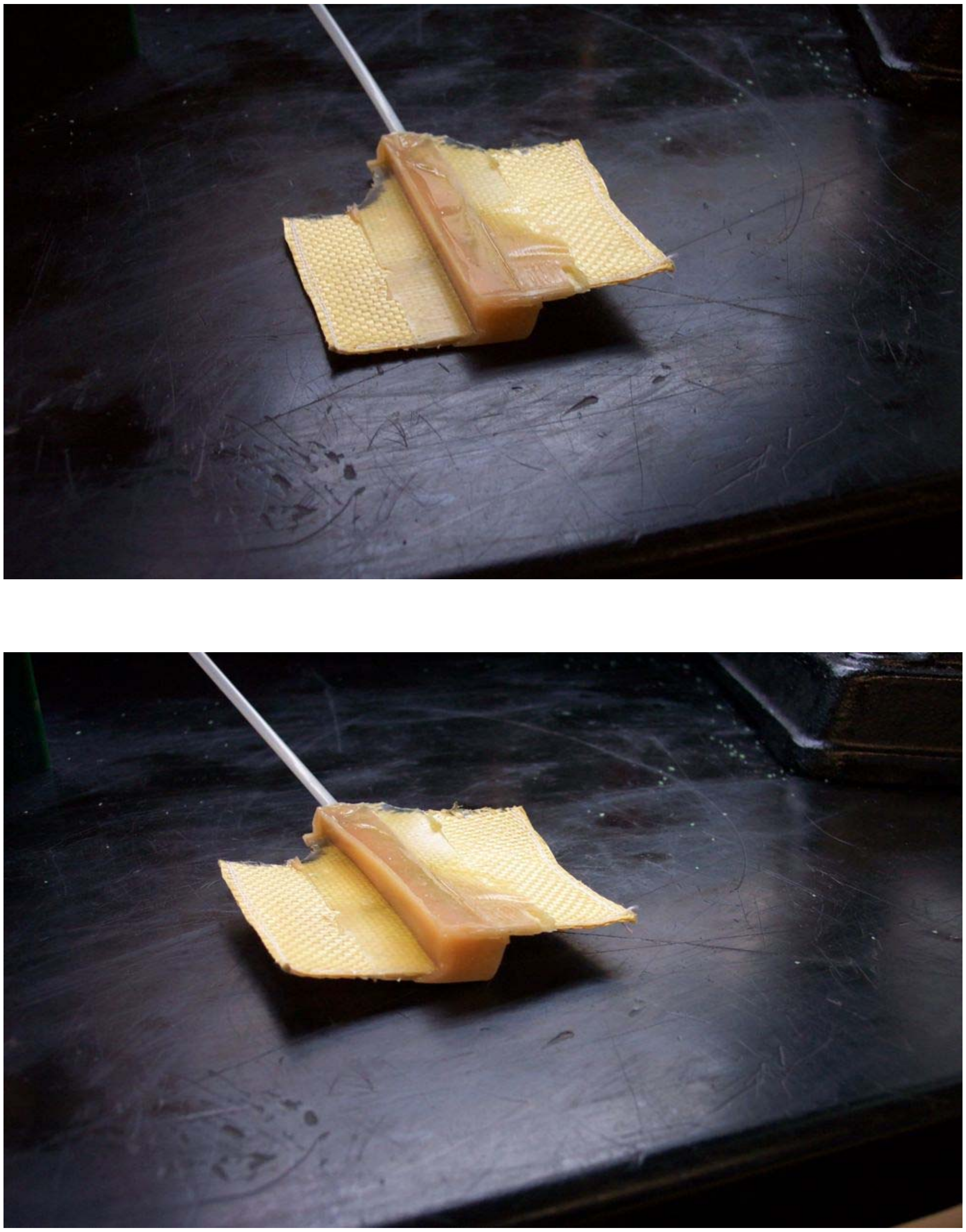

Figure 120. Isometric view of the actuator is showing also the rotating deformation behavior; without pressure (left), pressurized (right)

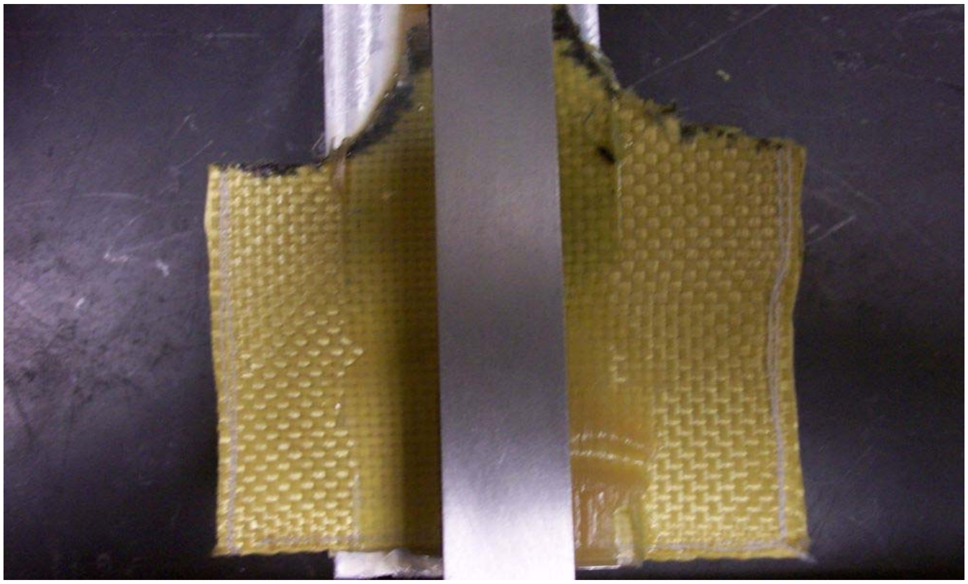

Figure 121. This picture shows the top view of the single element shear actuator before actuation.

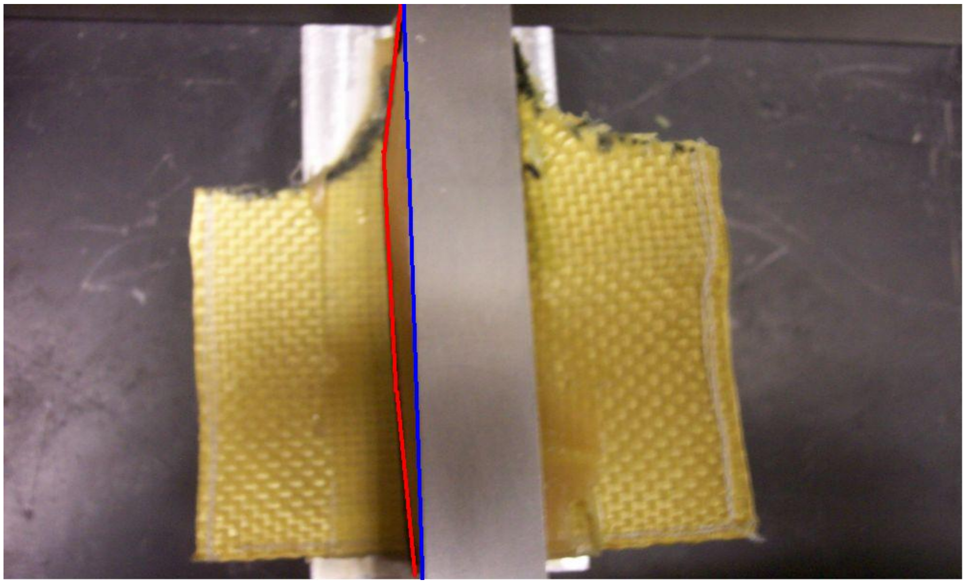

Figure 122. Single shear actuator is pressurized with 0.67 MPa (96.5 Psi). Shear amount is shown red and original line is shown in blue.

Figure 121 shows the top view of the shear actuator. At each pressure level (0.138, 0.276, 0.414, 0.552, 0.67, 0.827, and 1.034 MPa), top side free deformation is measured as in Figure 122. Free shear deformation at each pressure is calculated as in Figure 123. The result shows single shear actuator shows peak free strain up to 34% when pressurized with 1.034 MPa.

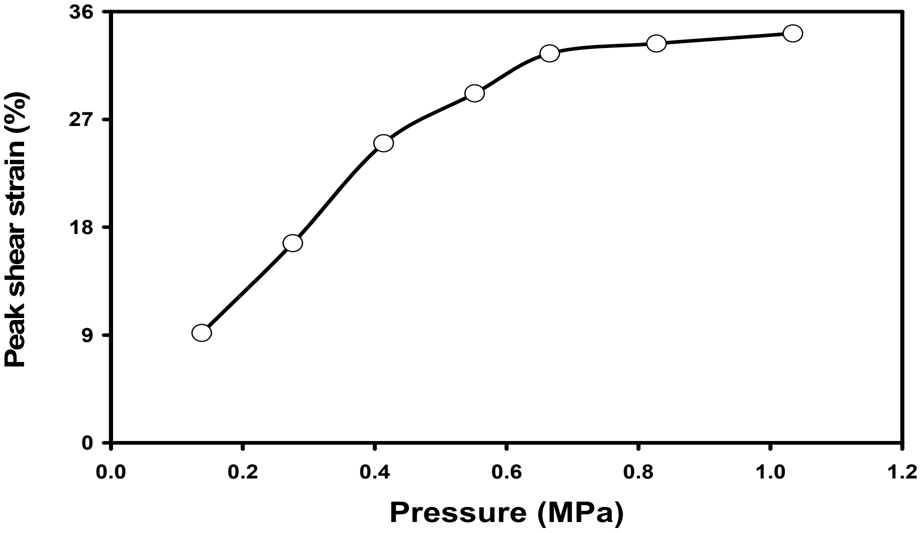

Figure 123. Pressure-shear strain plot represents that the single shear actuator shows more than 34% free shear deformation pressurized with 1.034 MPa. Reference height to calculate shear strain amount is 12mm.

5.4 Numerical Analysis of Single and Multi-Cell Behaviors

A single-shear direction model two-shear direction model is considered as the unit cell. The free strain behavior is described. Work performance are calculated using conventional work density and scientific work density. The multi-cell behavior is also simulated, based on single-direction model and two-direction model.

5.4.1 Application of failure criteria

As described in the section 2.6, rubber's fracture/failure modes include

(1) horizontal cracks occur near the bonded edges

(2) horizontal cracks occur in the free surface

For the free strain case, the criterion for internal rupture is [61]

$$-P_{\max} > \frac{3}{4}E \tag{34}$$

where $-P_{\max}$ is the maximum negative pressure developed in the block.

- Material properties of soft polyurethane matrix: from tensile test with 1035 resin.
  - 100% secant modulus: 0.060023 MPa
  - Poisson's ratio: 0.499999 (assumed from incompressibility condition)
- Material properties of Kevlar fabric element from Mr. McCutcheon's test data

- Young’s modulus : 100GPa
- Poisson’s ratio : 0.35

So the pressure inside the lens to make the matrix’s hydrostatic pressure correspond to 0.04502 MPa needs to be determined.

For blocked stress case, the maximum shear stress developed near the bonded edges, should be not exceed G, i.e. that the maximum shear deformation should not exceed about 100%. This is applied to each shear actuator analysis case.

By the failure criterion above, allowable actuation pressure inside lens for single shear actuator (without periodic boundary conditions) is

- For blocked stress: 14.77 MPa (= 2141.1 PSI = 147.7 Bar)
- For free strain: 1.2 MPa (=174 PSI = 12 Bar)

For twin shear actuator, maximum allowable actuation pressure inside lens for twin shear actuator (left lens pressurized only) is

- For blocked stress: 15.31 MPa (= 2220.45 PSI = 153.1 Bar)
- For free strain: 2.35 MPa (=340.998 PSI = 23.53 Bar)

5.4.2 Behavior of shear actuator

Two shear actuators are considered. The first one is single-shear direction model. It has only one lens element, and called single shear actuator hereafter. Second is two-shear direction model. It has two lens element, and can shear for left or right direction according to what lens is pressurized.

5.4.2.1 Single Shear Actuator

Single-shear direction actuator FEA simulations show that the deformation behavior is near perfect simple shear at lower pressure (Figure 124). Also with increasing pressure, the shear deformation is still dominant as in Figure 125. Figure 126 shows free shear strain vs. pressure plot.

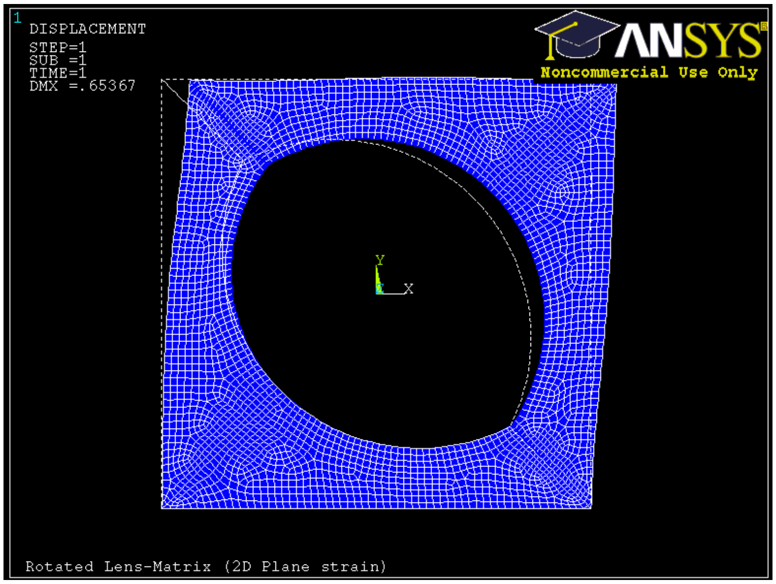

Figure 124. Free strain behavior of single shear actuator at 0.055 MPa (7.93 Psi) shows simple shear deformation. Boundary conditions are fixed bottom (Top, left & right edges are free)

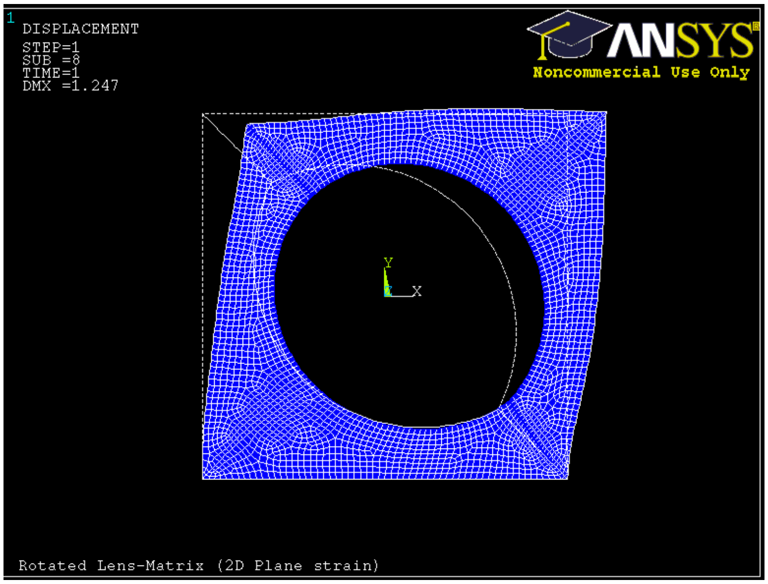

Figure 125. Free strain deformation behavior of single shear actuator with 1.09 MPa (158.6 Psi) shows shear dominant motion. Boundary conditions are same as in Figure 124.

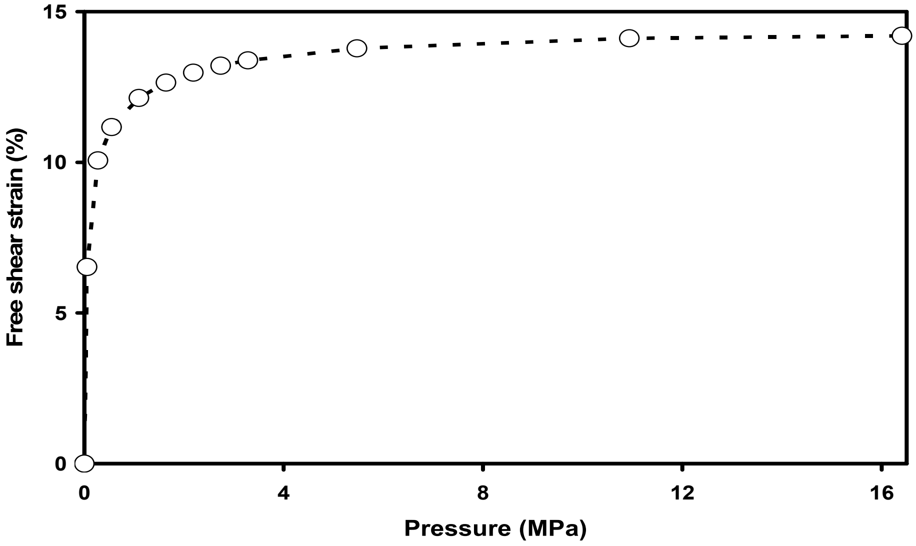

Figure 126. Free (peak) shear strain vs. pressure plot from nonlinear FEA simulation of single shear actuator shows 14.2% peak shear strain with 16.4 MPa. Boundary conditions are same as in Figure 124 and Figure 125.

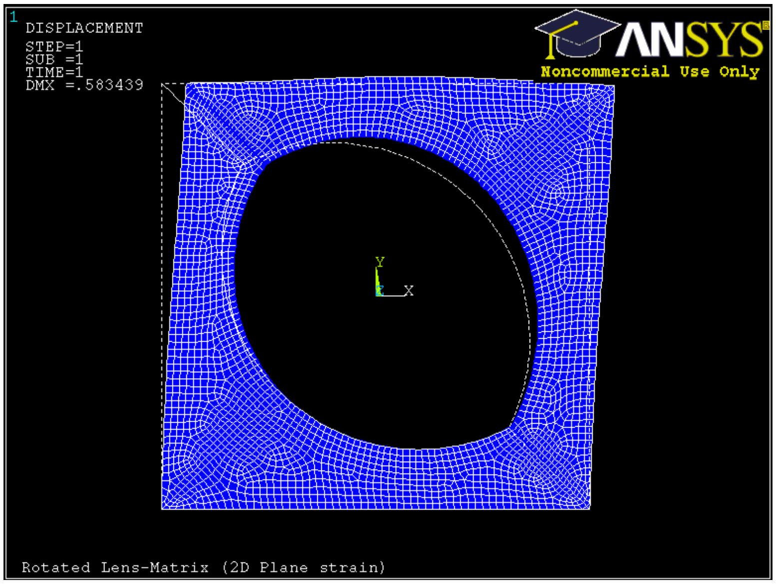

Figure 127. Free strain behavior of single shear actuator at 0.055 MPa (7.93 Psi) shows simple shear dominant deformation when periodic boundary conditions imposed on left & right edges. Other boundary conditions are same as before.

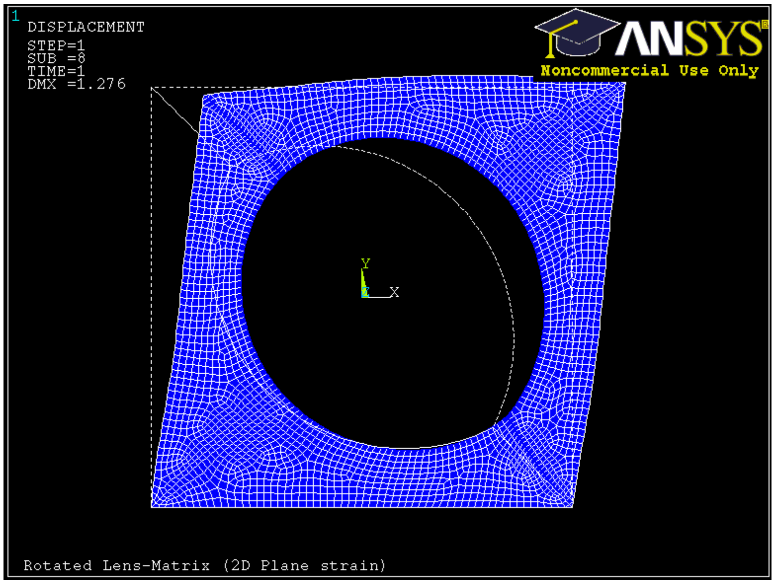

Figure 128. Free strain deformation behavior of single shear actuator at 1.09 MPa (158.6 Psi) shows still shear dominant motion. Boundary conditions are same as in Figure 127.

Figure 127~Figure 129 show the free strain behavior when periodic boundary conditions imposed on left and right edges.

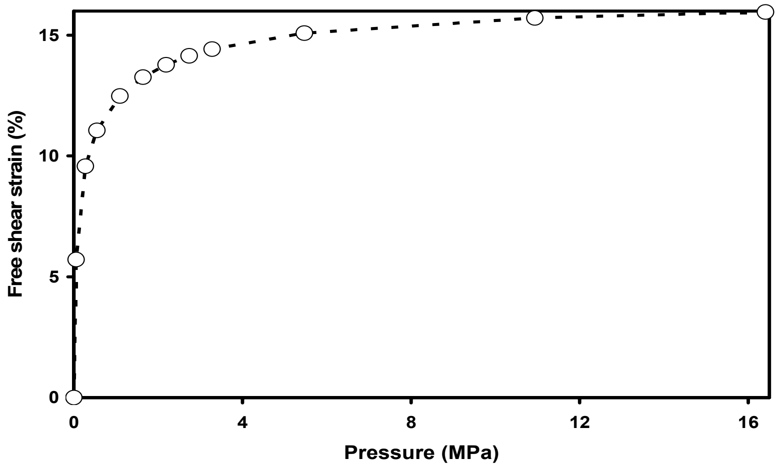

Figure 129. Free (peak) shear strain vs. pressure plot of single shear actuator is shown when periodic boundary condition imposed. Peak strain reaches 16% with 16.4 MPa this case.

5.4.2.2 Twin Shear Actuator

In this work, only left lens in twin shear actuator is pressurized, and twin shear actuator is showing shear in right direction (Figure 130 and Figure 131).

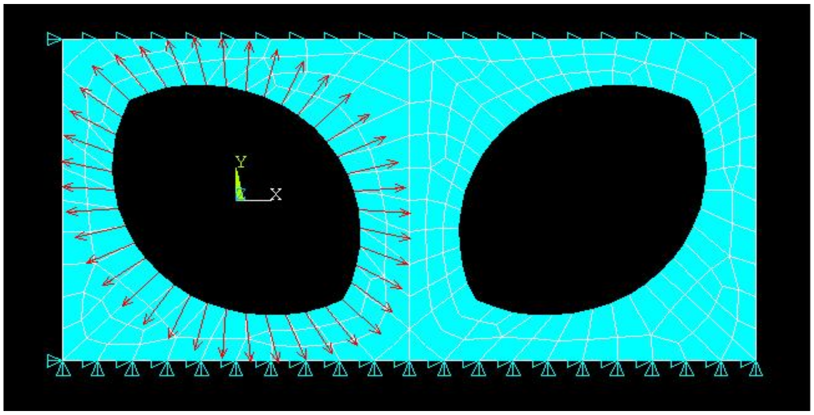

Figure 130. Twin shear actuator model shows pressure is applied to the left lens element.

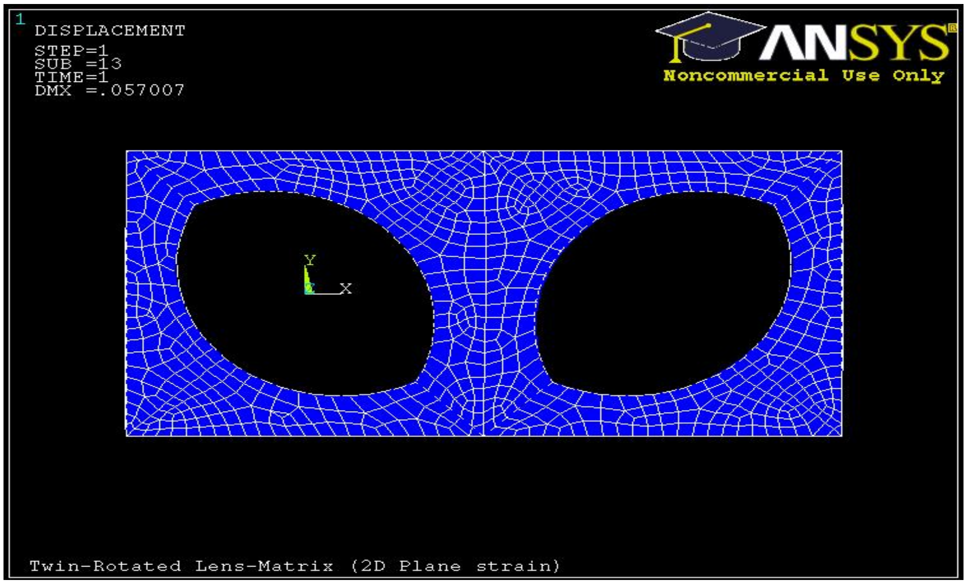

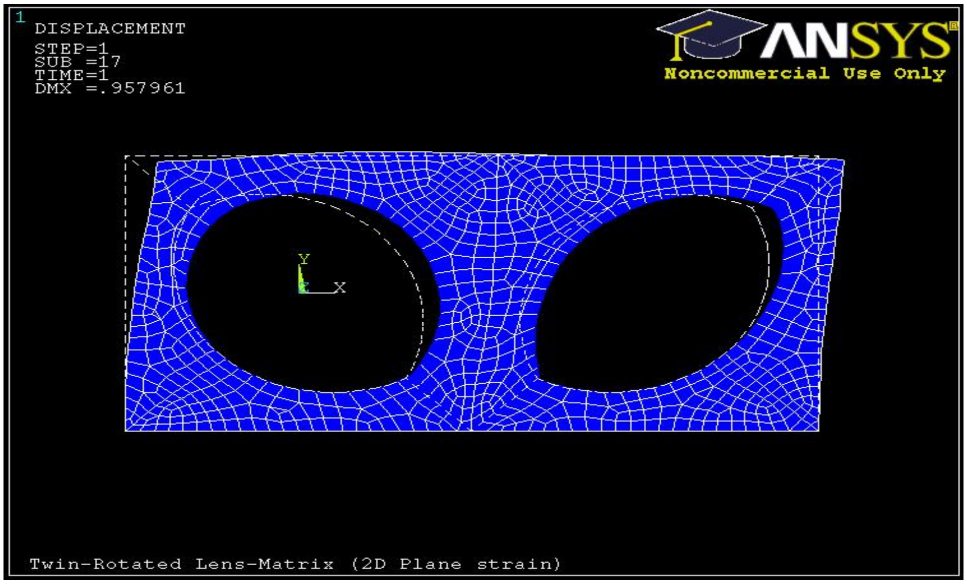

Figure 131. Left lens element is pressurized for this two direction shear actuator. Blocked stress state is shown top, and free strains is shown at bottom.

5.4.3 Work performance of shear actuator

In this section, work performance is calculated as work per actuator unit volume. It started with single-shear actuator work density, calculating both conventional work density and scientific work density. The values are compared to the existing actuating materials from the reference (Figure 132 and Figure 133). Same procedure is applied to two-direction shear actuator and find work performances.

5.4.3.1 Work Density of Single Shear Actuator

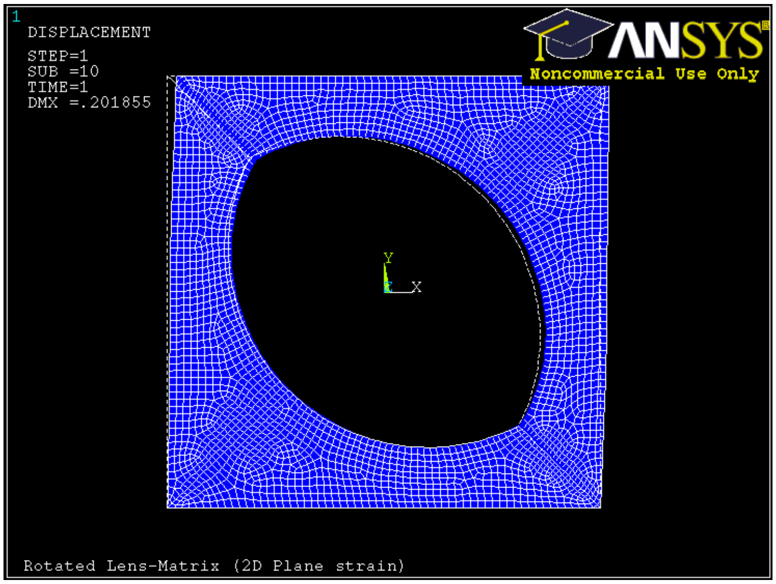

Figure 132. To calculate work density, prescribed displacements are imposed to the FEA models. This picture shows an example of given 2% shear strain on the top plane. Other boundary conditions are Bottom fixed, top Uy (horizontal move) fixed, and left & right edges are free.

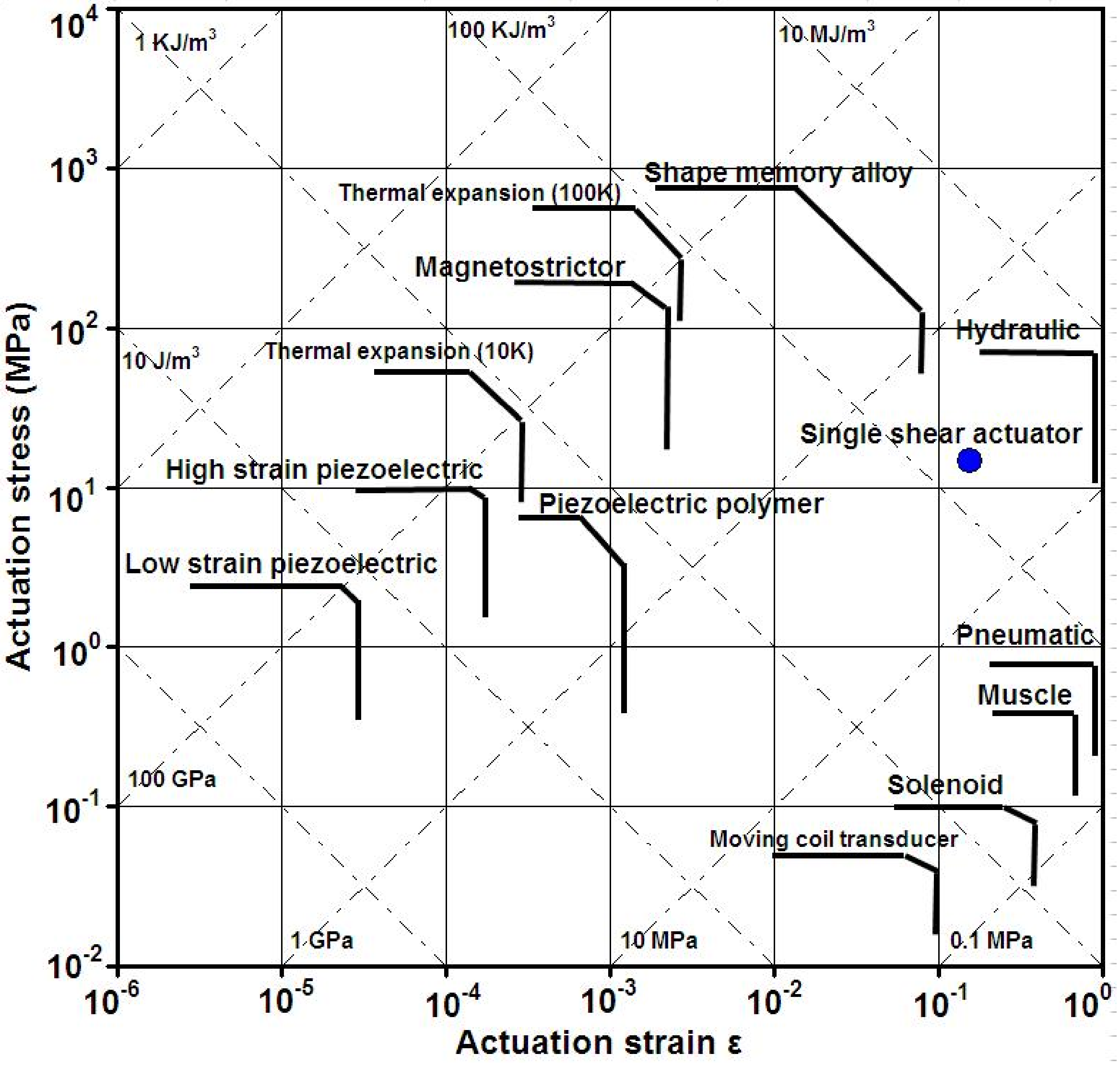

Figure 133. This actuator performance chart [40] is based upon industrial convention, which is calculated from blocked stress and free strain of the actuator. For single shear actuator, conventional work density is 228.9 KJ/m^3 (=0.229 MJ/m^3), and shown as a dot in right side. It shows the work density line of single shear actuator is slightly less than shape memory alloy, but is much higher than piezoelectrics and magnetostrictor.

Figure 134 shows scientific work density of single-shear actuator.

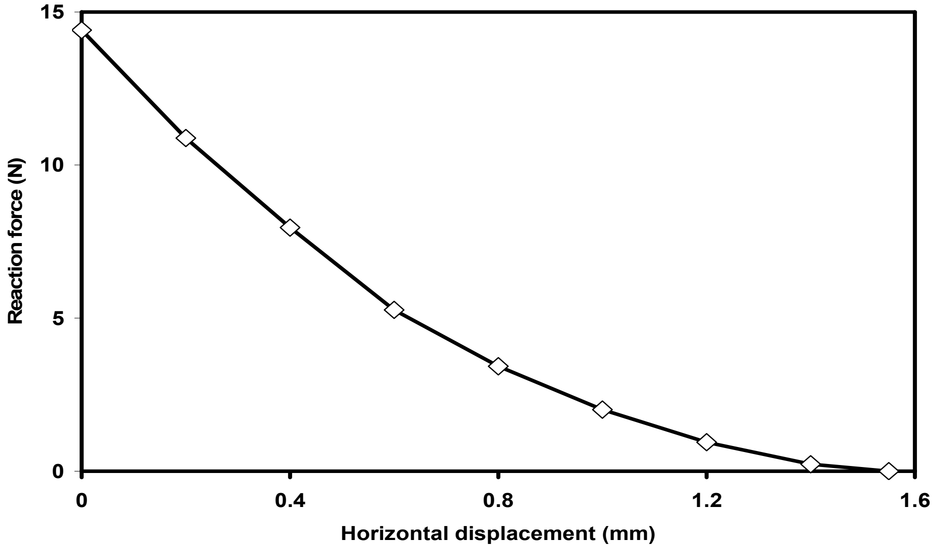

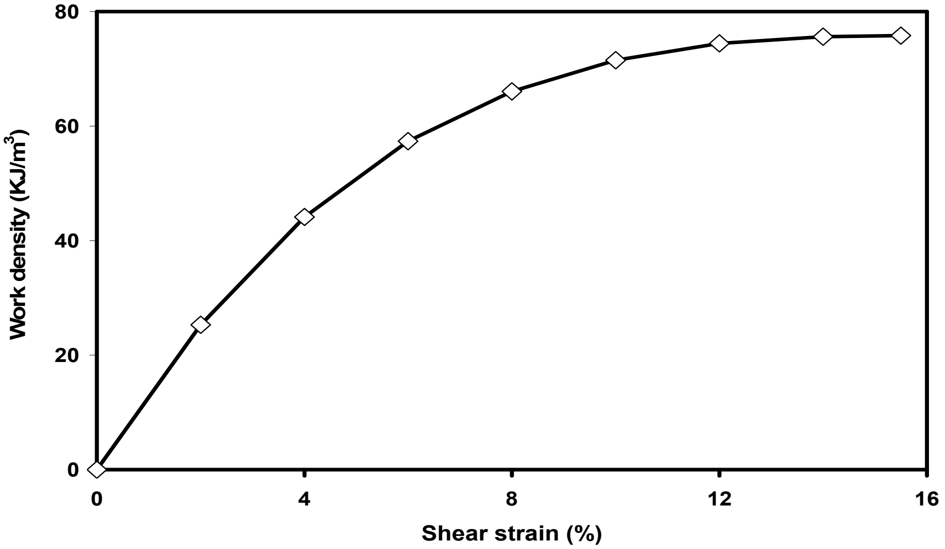

Figure 134. By scientific calculations, work density reaches 75.8 KJ/m^3 for single shear actuator. This is lower than the conventional density as expected because the integration area (force-displacement) to calculate work density is smaller than conventional work density.

5.4.3.2 Work Density of Twin Shear Actuator

Twin shear actuator work density is calculated in a similar manner to single shear actuator. For conventional work density in Figure 135, this actuator has lower blocked stress than shape memory alloy, thermal expansion, magnetostrictor, and hydraulic, but higher blocked stress than piezoelectrics, pneumatic, muscle, solenoid, and moving coil transducer.

The free strain is higher than shape many existing actuating materials, for example, shape memory alloy, magnetostrictor, and piezoelectrics. For the work density values, it is slightly less than shape memory alloy, but higher than magnetostrictor, thermal expansion, and piezoelectrics.

Figure 136 shows scientific work density of twin shear actuator.

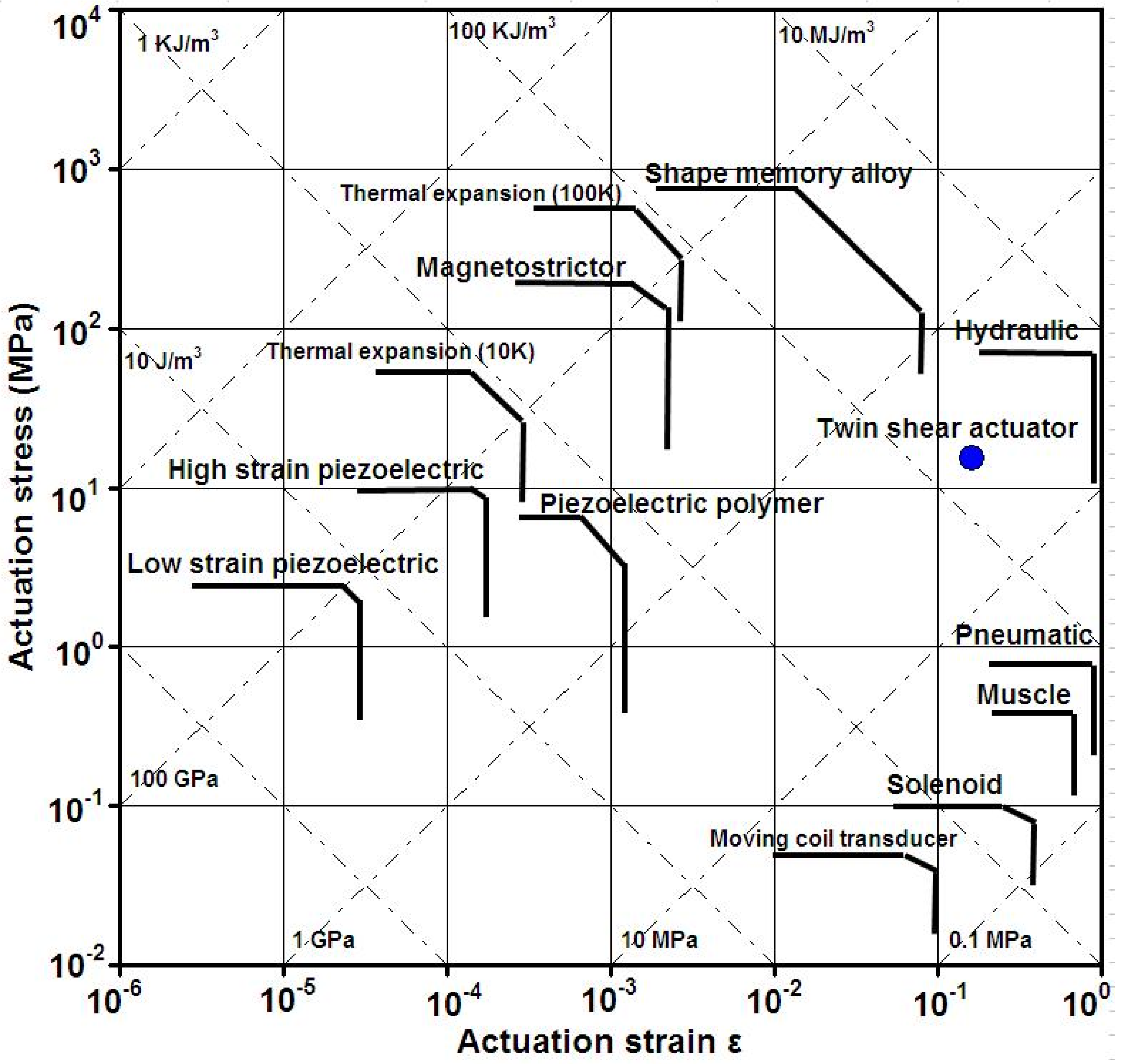

Figure 135. For twin shear actuator, by industrial convention [40], work density is 248.2 KJ/m^3 (=0.2482 MJ/m^3). It is shown as a dot in right side. This actuator has almost same work density as shape memory alloy, and higher than magnetostrictor, thermal expansion, and piezoeletrics.

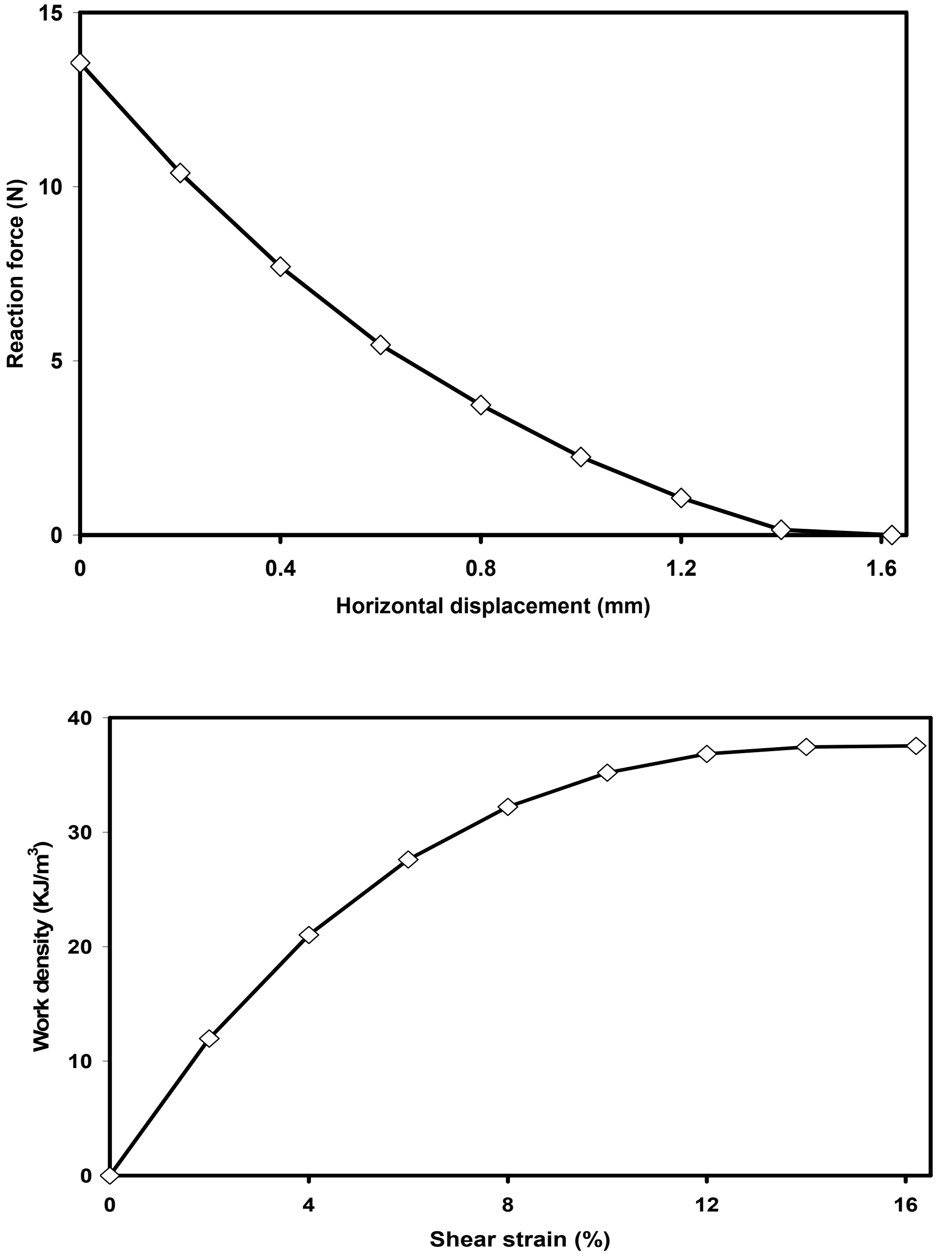

Figure 136. By scientific calculations, work density reaches 37.5 KJ/m^3 for twin shear actuator. Similar to single shear actuator case, the scientific work density is smaller than conventional work density. Also note that the scientific work density of twin shear actuator is smaller than single shear actuator because the volume of actuator is as twice as the single shear actuator.

5.4.4 Power vs. efficiency of single and twin shear actuator

According to the ref. [40], volumetric power and efficiency is defined as follows.

- Volumetric power (p): The mechanical power output per unit initial volume in sustainable cyclic operation.
- Efficiency (η): The mechanical work output-energy input ratio during a complete cycle in cyclic operation.

For estimating volumetric power, the operating frequency for both single and twin shear actuator is assumed as 2 Hz.

Now calculation examples for single actuator are shown a s the following. The results is summarized in Table 5.

- Work density, single shear actuator = 228.8813 KJ/m^3
- Power: $1W = 1J / s$
- So, volumetric power (= power output per unit volume) = 457.76269 KW/m^3

  = 457762.69 W/m^3
- For energy input, as shown in Figure 137, energy input per unit volume is 1237.7 KJ/m^3, and mechanical work output per unit volume for single actuator is 228.8813 KJ/m^3.
- Therefore, efficiency for single shear actuator is $\frac{228.8813}{1237.7} = 0.1849$.

The calculation examples for twin actuator is as the following

- Volumetric power = 248.216 KJ/m^3 × 2 Hz (= 2 cycles/s)

  = 496.43 KW/m^3 = 496431.3 W/m^3

- And efficiency for twin shear actuator is

$$\frac{Mechanical\ work\ output\ \ per\ unit\ volume}{Energy\ input\ \ per\ unit\ volume} = \frac{248.22}{1431.67} = 0.1734\,.$$

The estimated power vs. efficiency is shown in Figure 138. The power is lower than piezoelectrics because piezoelectric actuator has lower blocked stress, but much higher operating frequency.

Also the shape memory alloy power is higher than shear actuator because shape memory alloy has significantly high blocked stress.

Table 5. Power and efficiency estimations for single and twin shear actuator

	Single	Twin
“Guessed” operating frequency	2 Hz	2 Hz
Work density (using industrial convention) = mechanical work output per unit volume	228.8813 KJ/m^3	248.2257 KJ/m^3
Volumetric power (= power output per unit volume)	457762.69 W/m^3 = 457.76 KW/m^3 = 0.4578 MW/m^3	496431.3 W/m^3 = 496.431 KW/m^3 = 0.4964 MW/m^3
Energy input per unit volume	1237.7 KJ/m^3	1431.67 KJ/m^3
Efficiency	0.1849	0.1734

Figure 137 shows energy input for single and twin shear actuator, and Figure 138 shows volumetric power and efficiency.

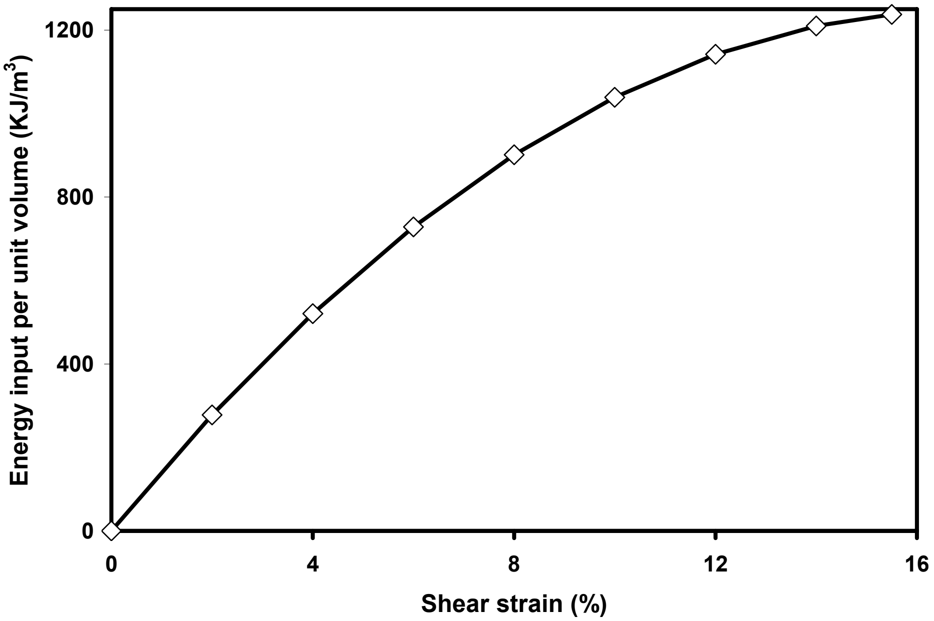

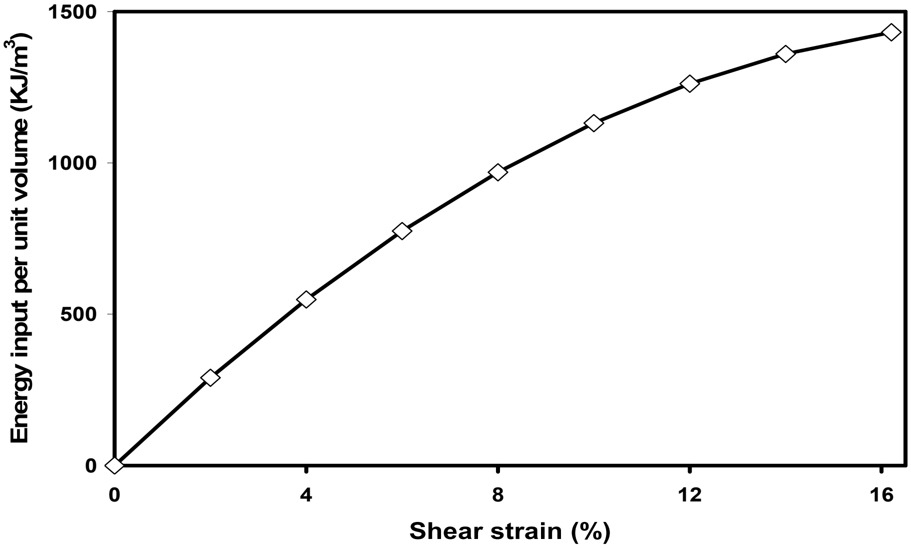

Figure 137. These pictures show energy input to calculate the efficiency in Table 5 for the single (top) and twin (bottom) shear actuator.

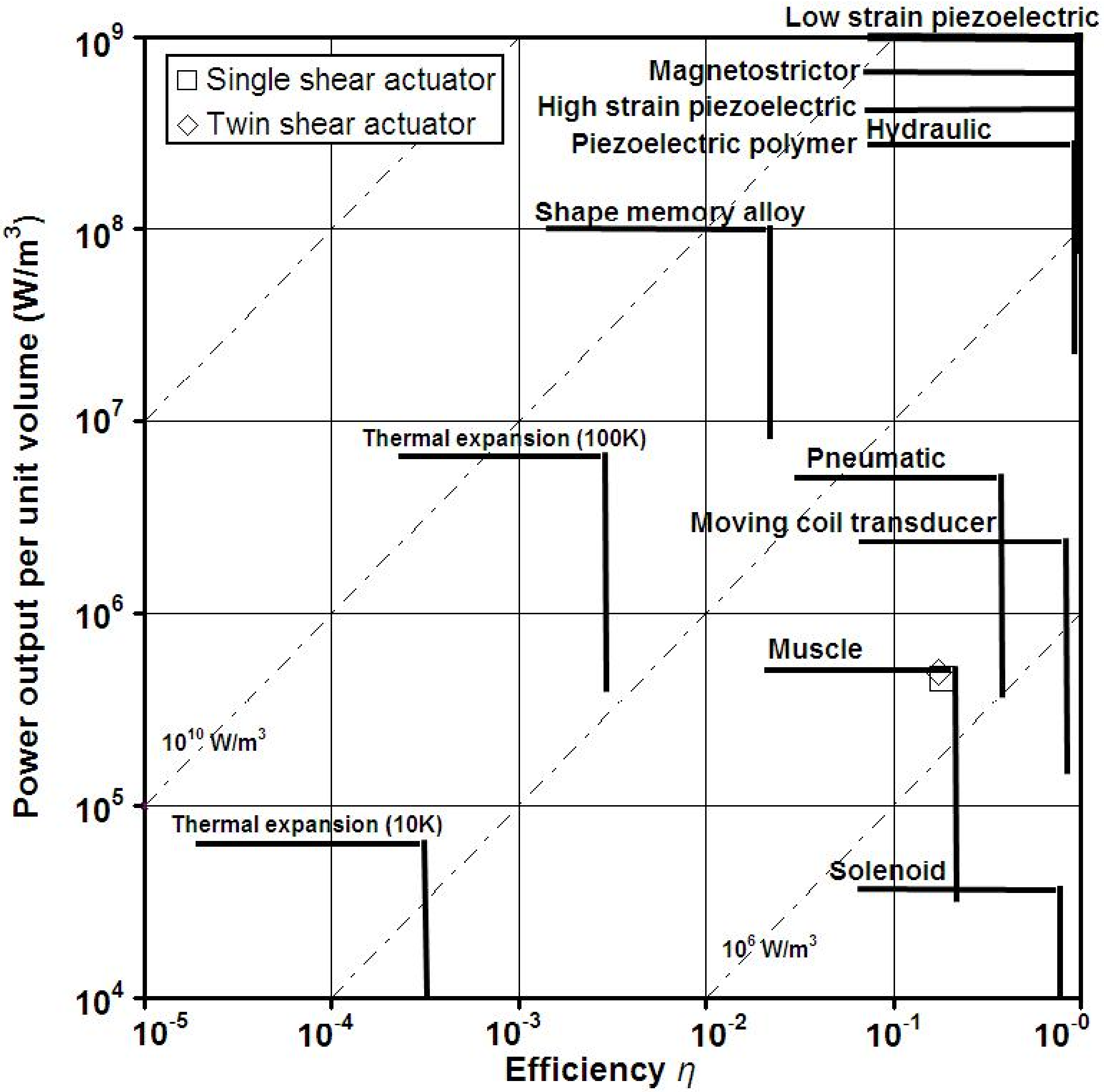

Figure 138. Volumetric power and efficiency chart (after [40]) is shown. The single and twin actuator is shown as square and diamond, respectively, in the right side. The piezoelectrics has higher operating frequency so it has higher power than shear actuator even though blocked stress of piezoelectrics are low. The shape memory alloy has higher blocked stress so the power of shape memory alloy is higher than shear actuators.

5.4.5 Numerical simulations of multi-cell array

Repeated single shear actuator array (1, 3, 5, 7, 9, 11, and 13 unit cells), and twin shear actuator (2, 6, 10 unit cells) are modeled and simulated. The maximum shear strains and work densities are obtained from FEA simulations to predict the array's behavior.

5.4.5.1 FEA Model of Array with Single and Twin Shear Actuator

This section shows the FEA models used to simulate the array behavior using single and twin shear actuator (Figure 139, Figure 140, and Figure 141).

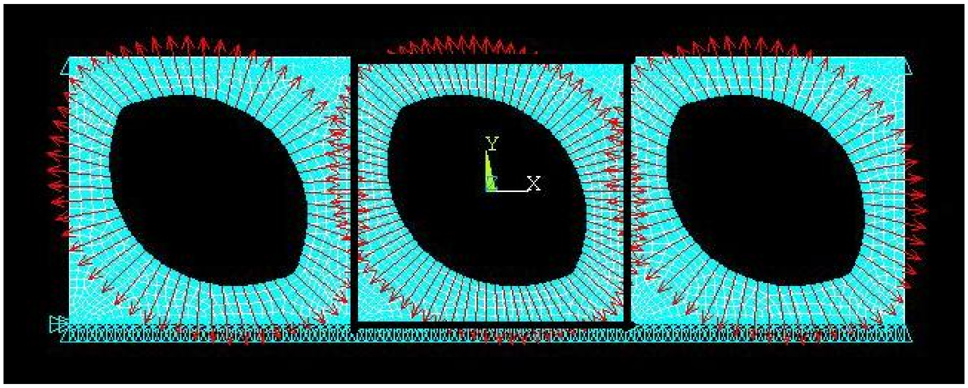

Figure 139. This array of shear actuator is composed of 3 singles. The box shows unit cell.

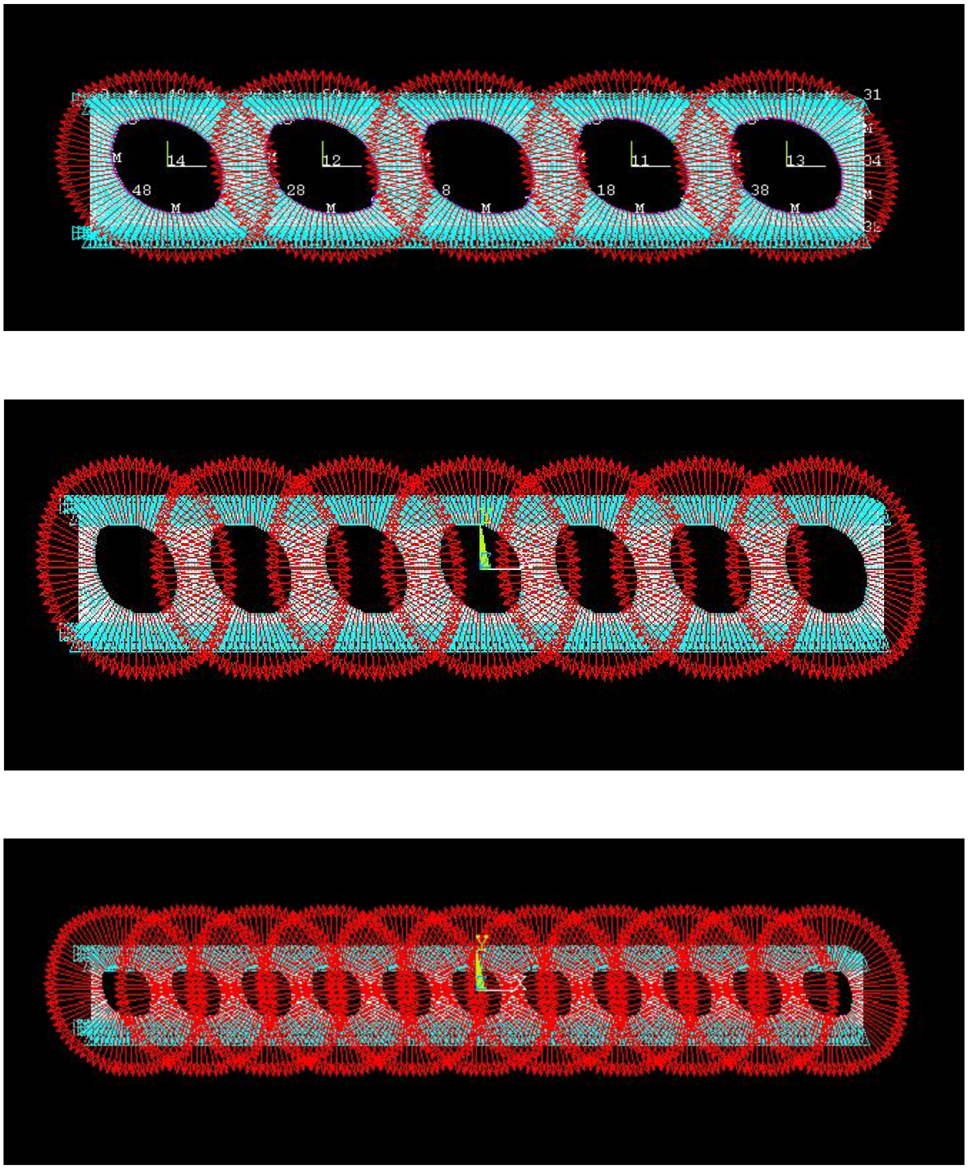

Figure 140. This picture shows FEA models of array of shear actuator – 5, 7, and 11 shear actuators.

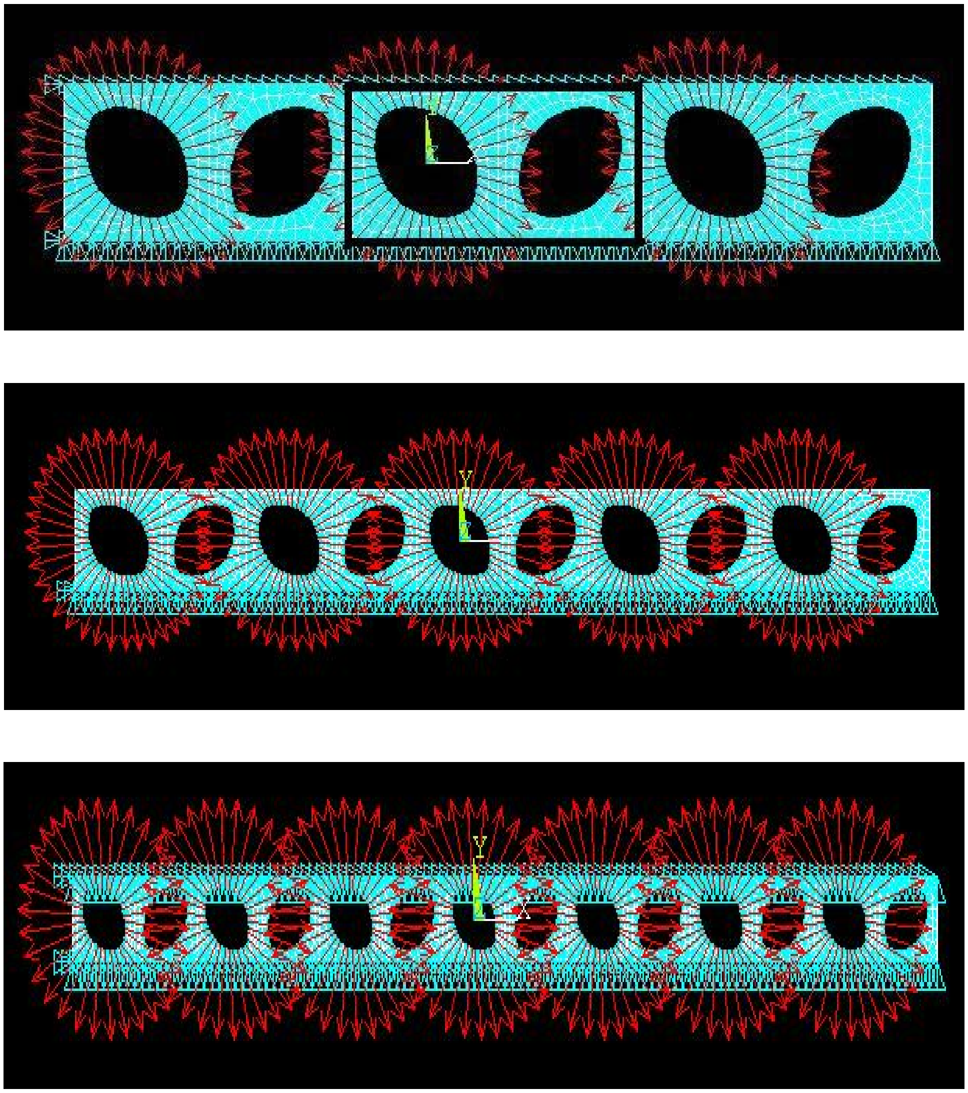

Figure 141. Array of shear actuator composed of 6, 10, 14 shear actuators.
Please note that 14 actuator model was running for free strain case only as in Figure 143.

5.4.5.2 Work Performance of Multi-Cell Array

To predict multi-cell array performance, the shear strain and work performance of the single shear actuator in Figure 139 and the twin shear actuator in Figure 141 is shown below. Please note that the performance of the unit cell is shown so that we can see if solo and array performance differ; we want the whole array performance.

For single-shear actuator arrays, the center unit cell shear strains remain constant after 7 cells are in the model. The work density reaches the highest value at 5 cells, and converges to the same value for whole actuator and unit cell. Figure 142 shows this information.

For arrays containing twin-shear actuator, the center unit-cell shear strain and work density becomes constant after 6 cell-twins actuator. Figure 143 shows the change in this values with increasing model size.

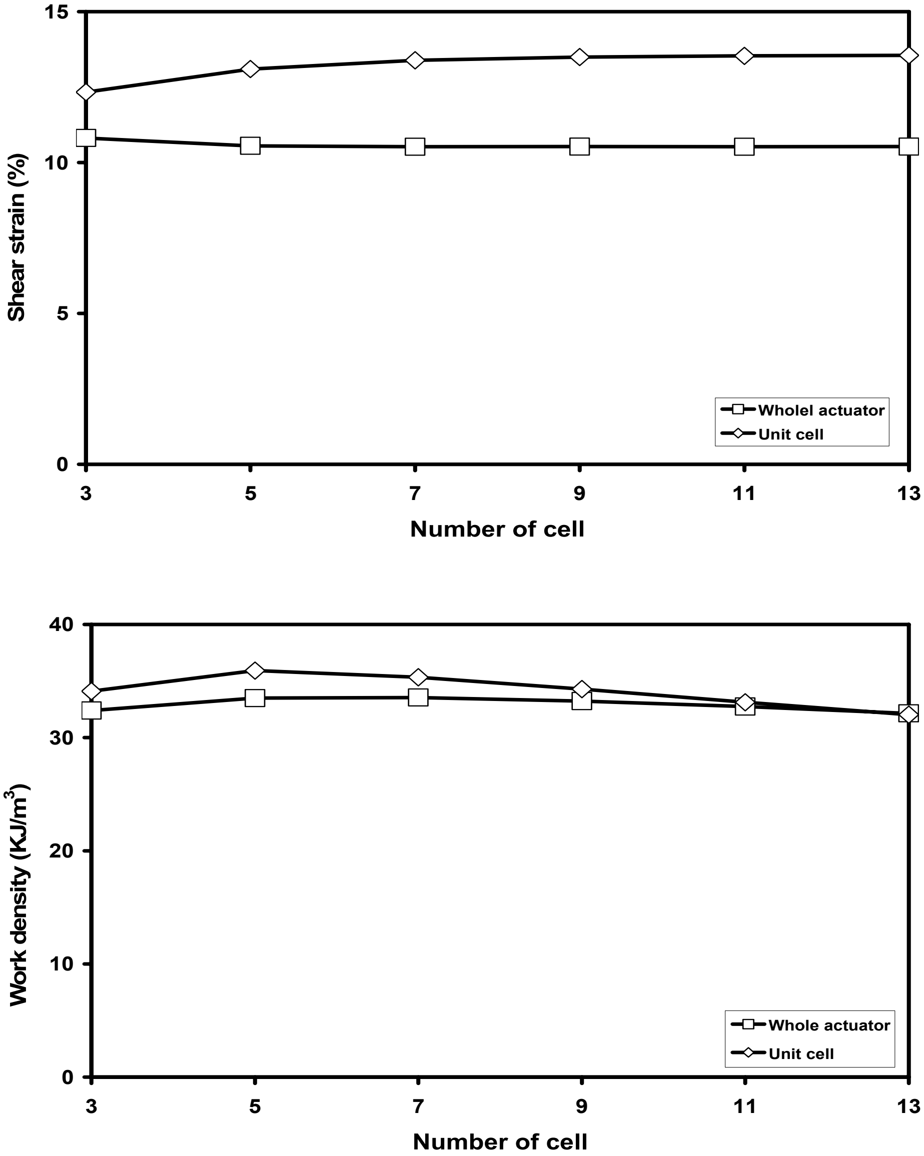

Figure 142. Maximum shear strain; work density vs. number of cells of single shear actuator is shown. The shear strains remain constant after 7 cells. The work density reaches the highest value at 5 cells, and converges to the same value for whole actuator and unit cell.

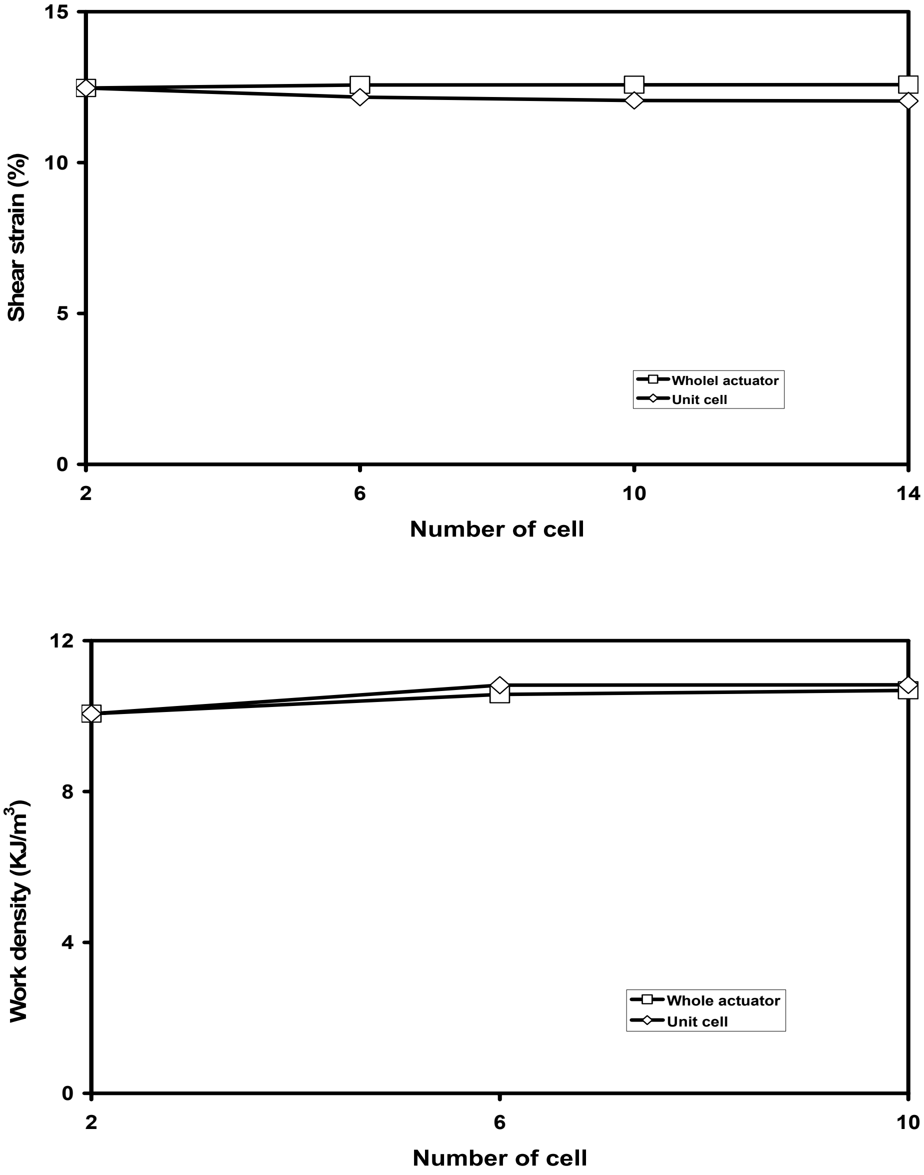

Figure 143. Maximum shear strain; work density vs. number of cells of twin shear actuator is shown. The shear strain and work density held constant after 6 cell twin actuator.

CHAPTER VI

INTEGRATION INTO THE STRUCTURAL APPLICATIONS

6.1 Application to the Structural Panel

The triangular beam is modeled in this chapter. The nastic actuator and conventional motor provide power to twist the beam. To estimate the efficient and powerful way, each mechanism's work performance, power, and price are analyzed and compared.

6.1.1 Split beam model - the beam with monolithic rubber block

The split beam is made with aluminum. The monolithic elastomer block, representing the nastic actuator, is applied between the split (Figure 144, Figure 145, and Figure 146). The aluminum beam—aluminum Alloy 6061-O[96]—has material properties:

- Young's modulus : 68.947 GPa
- Poisson's ratio : 0.33

Von Mises stress criteria provides this beam's failure stress (Figure 145). The yield stress of Aluminum alloy 6061-O is 48.3 MPa ([97]). Maximum Von Mises stresses at each node are compared to the yield stress.

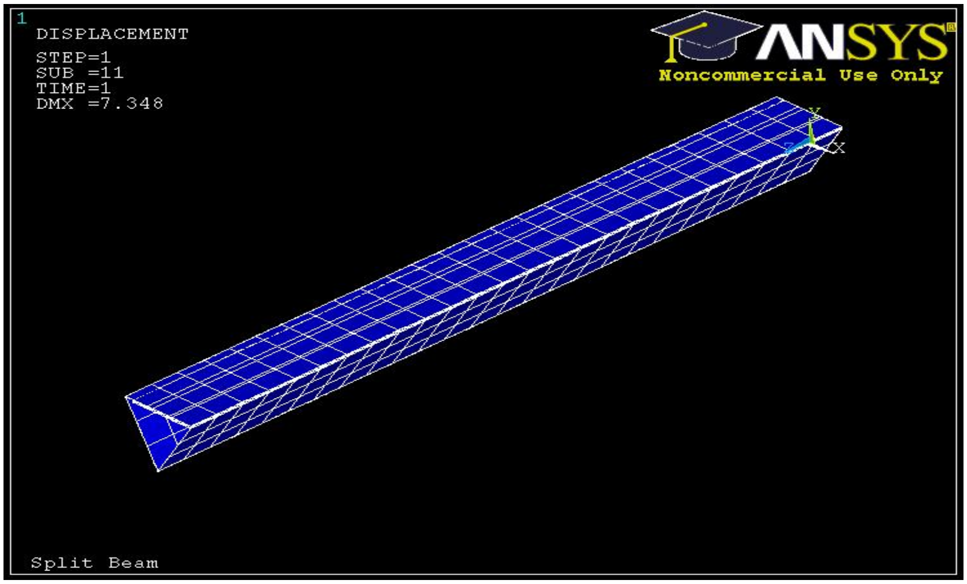

Figure 144. FEA model of split beam with rubber block model is shown in isometric view.

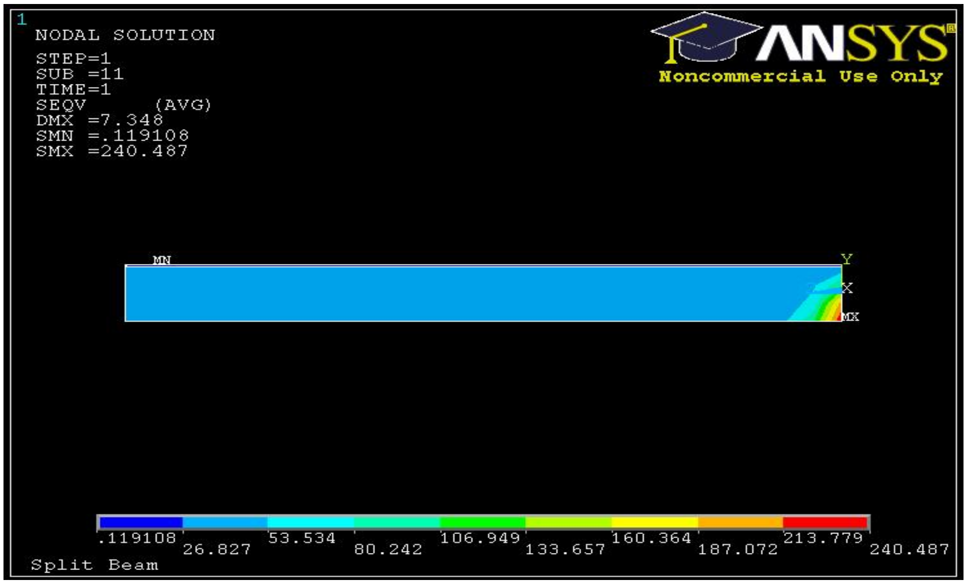

Figure 145. Von Mises stress distribution is shown at applied pressure 48.9 MPa.

The failure criteria applied to split beam model. The maximum twist angle correspond to this criteria is 12.76° (0.051° per unit length), and the deformation state in this twist angle is in Figure 146.

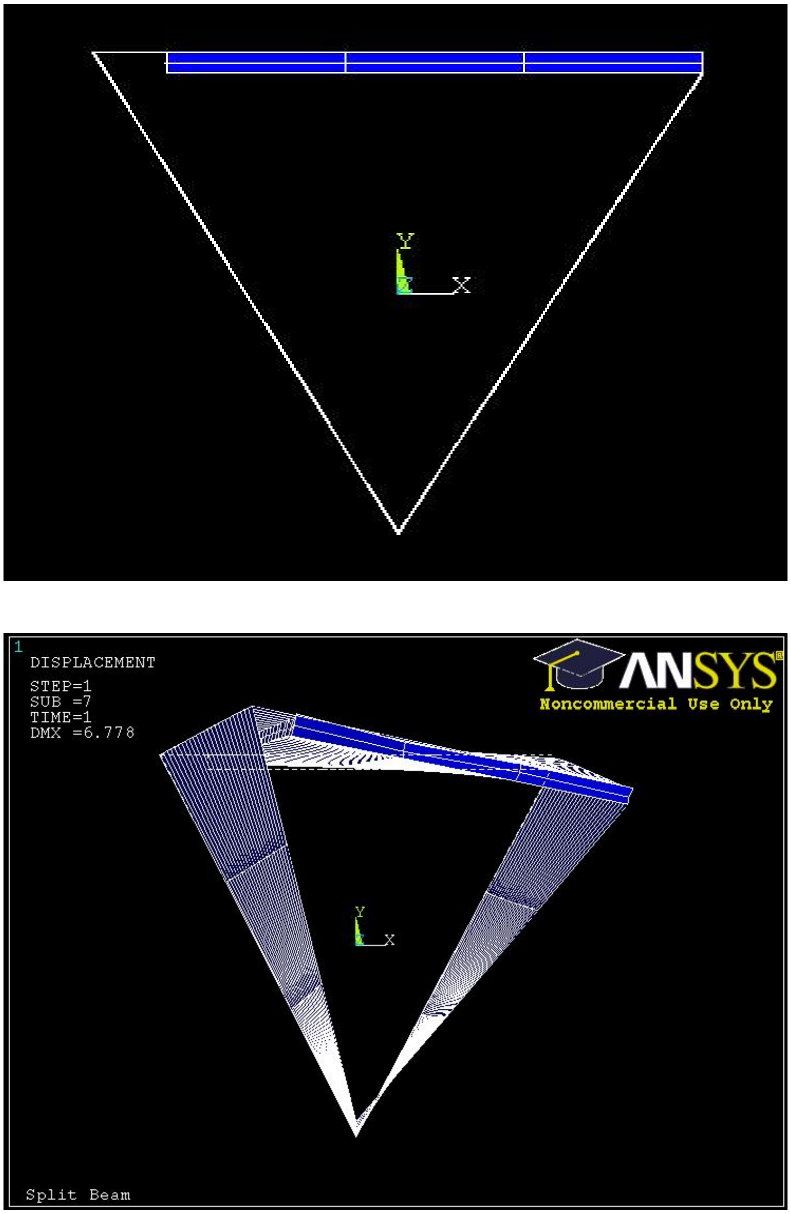

Figure 146. Front view of split beam with monolithic rubber block is shown; (Top) undeformed model, (Bottom) Deformed model (12.76° rotated) pressurized with 50.6 MPa.

The conventional work density is calculated from the maximum allowable actuation stress and actuation strain. The split beam/nastic actuator's conventional work density is 1.127 MJ/m^3, which appears as a dot in Figure 147.

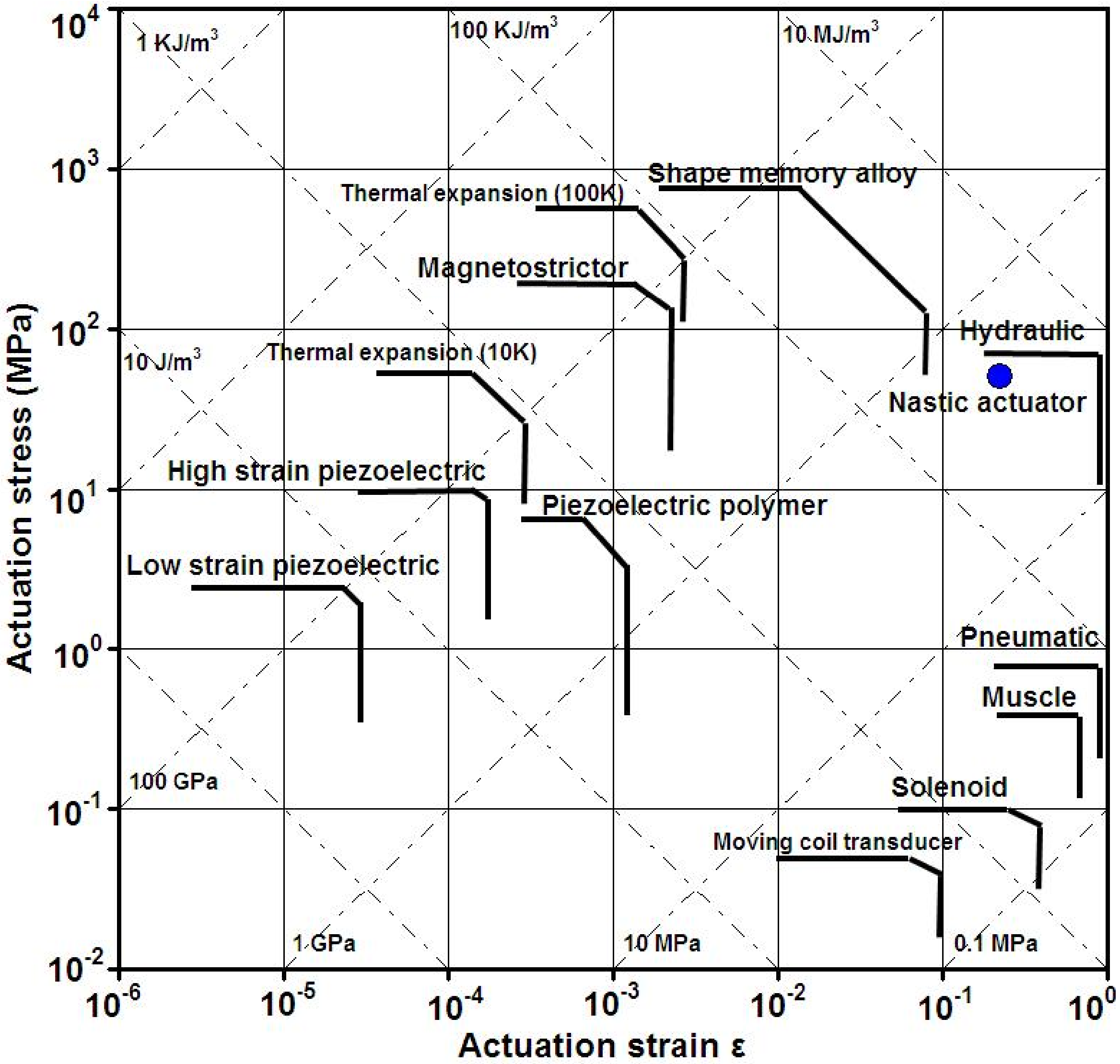

Figure 147. Conventional work density for split beam is 1.127 MJ/m^3 (actuator performance chart drawn after [40]) The nastic actuator is shown as a dot in right side. It has same or higher work density than most of existing actuators including shape memory and piezoelectrics.

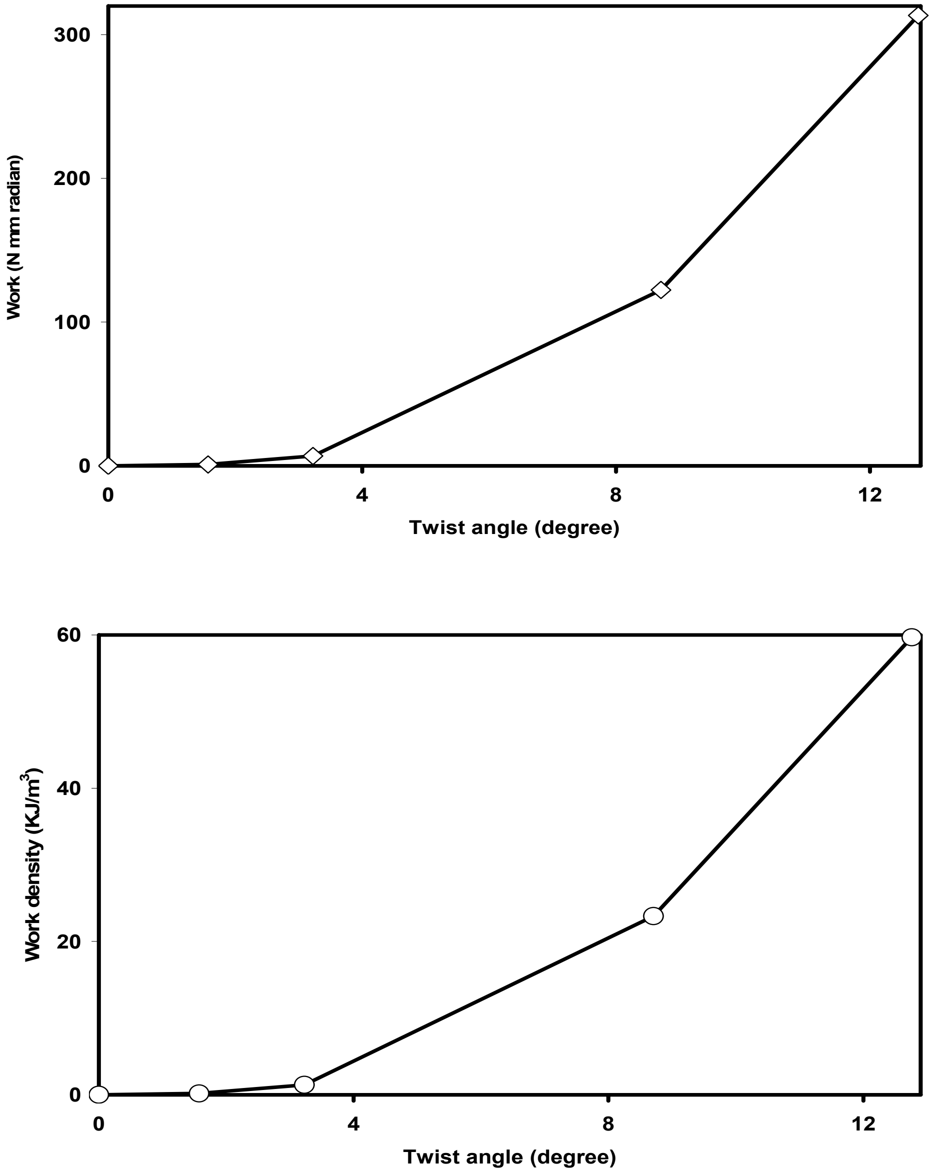

Figure 148. Scientific work performance of the beam with nastic actuator reaches 59.7 KJ/m^3. Although work value is lower, work density is bigger due to smaller volume of the actuator.

Scientific work density for the split beam with nastic actuator shows 59.7 KJ/m^3 (Figure 148). The equation to calculate scientific work density is the following

- For both nastic actuator and conventional actuator (motor)

$$\frac{reaction\ moment \times Twist\ angle}{Volume} = \frac{N \cdot mm \times \alpha(radian)}{Base \times Height \times Depth(mm^3)} = MJ / m^3$$

6.1.2 Conventional triangular beam model

Triangle beam with conventional motor and rod is modeled (Figure 149). The triangle beam uses same Aluminum Alloy 6061-O as the split beam with nastic actuator in previous section.

The material used for the rod is AISI 1010 Steel, cold drawn (low carbon steel). The material property is as the following [98]

- Young’s modulus 205 GPa
- shear modulus 80 GPa
- Poisson’s ratio 0.29
- Yield strength 305 MPa

For triangle beam with conventional motor and rod, the torque required the twist beam same angle (12.76°) as the nastic actuator is as follows.

- Torque required (N•mm)=26604.88N•mm=27.15Kgf•mm

Maximum motor power output 27.15Kgf•mm×46rpm/974=1.282107KW

Two motor candidates were selected. One can provide higher power, but expensive. The other can provide the torque only about half as needed, but it is much cheaper.

- Motor 1: High-Torque Face-Mount Air-Powered Gear motors [99]

  Gives more torque needed (1.384 KW), Price: $3476,

- Motor 2: DC gear motors [99]

  Gives half the torque needed (0.605 KW), Price: $607.

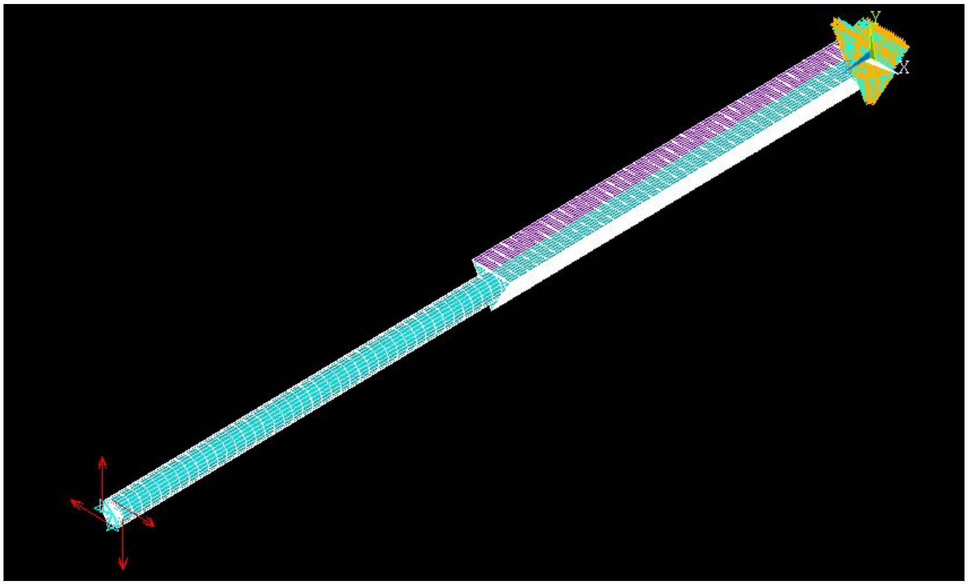

Figure 149. This picture shows equivalent model of cylinder inside the beam.

Figure 150 and Figure 151 show the work value and work density from conventional beam-motor systems, respectively.

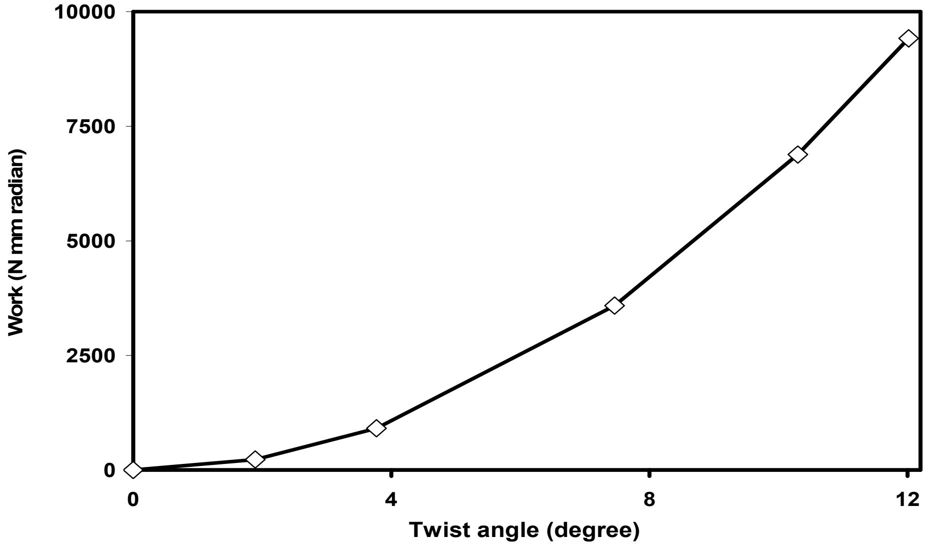

Figure 150. The work value is calculated for conventional beam-motor system. Please note that work value (9416.36 N•mm•radian) is much higher (2904 %) than work of nastic actuator (313.42 N•mm•radian) from Figure 148. This means conventional actuator system needs much more work to twist the beam as the same angle as nastic actuator.

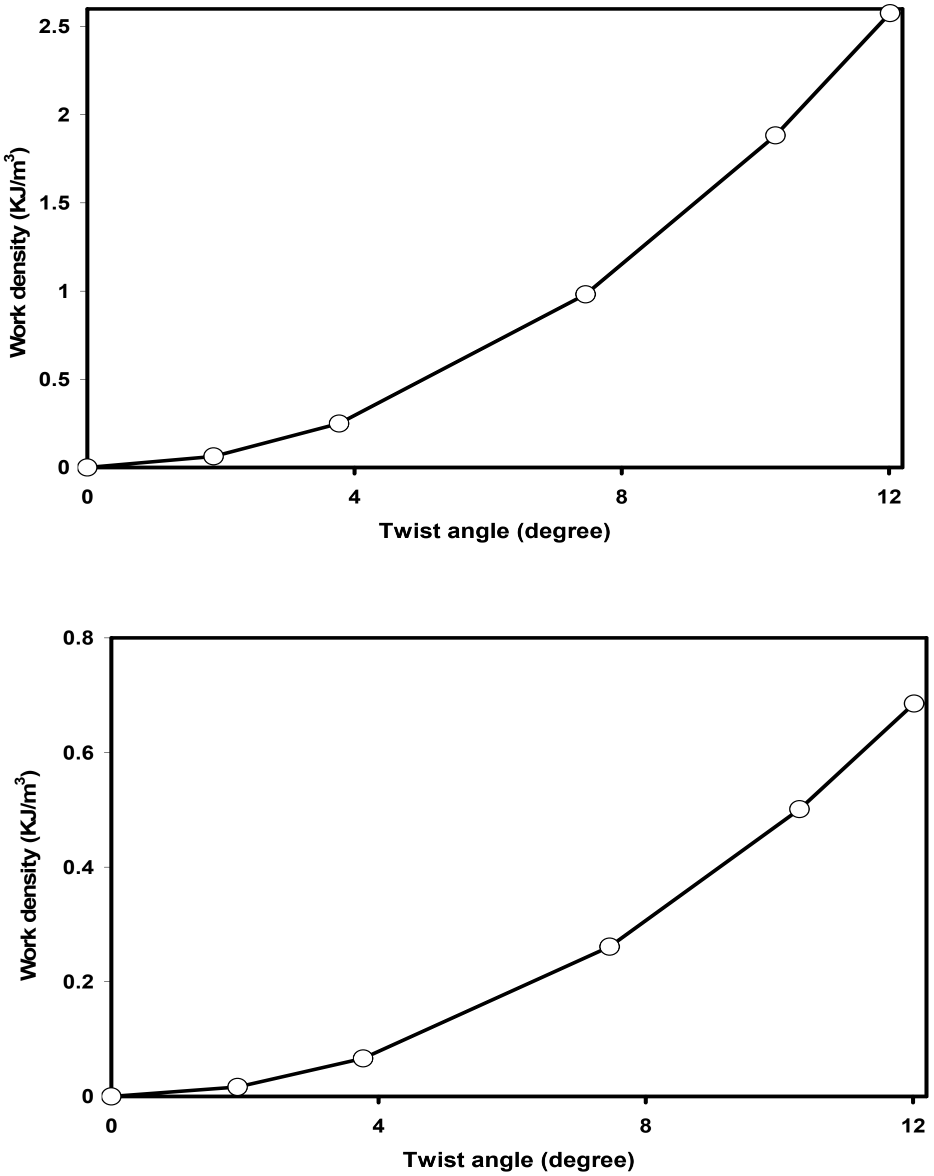

Figure 151. Work performance of equivalent model: Work vs. twist angle (top), work density using motor1 (Middle), work density using motor2 (Bottom). The work density values are much smaller than the nastic actuator. In calculation, the work density (work per unit volume) of nastic actuator is as high as 2280~8471% than the conventional actuators using electric motors.

6.2 Work per Unit Mass of Each System

In this research, actuating system work performance refers to the work density as work per actuator unit volume. However, the work density as work per unit mass (Figure 152) of the actuator is also an important factor for actuating system, especially for aircraft or space vehicles because their weight is constrained.

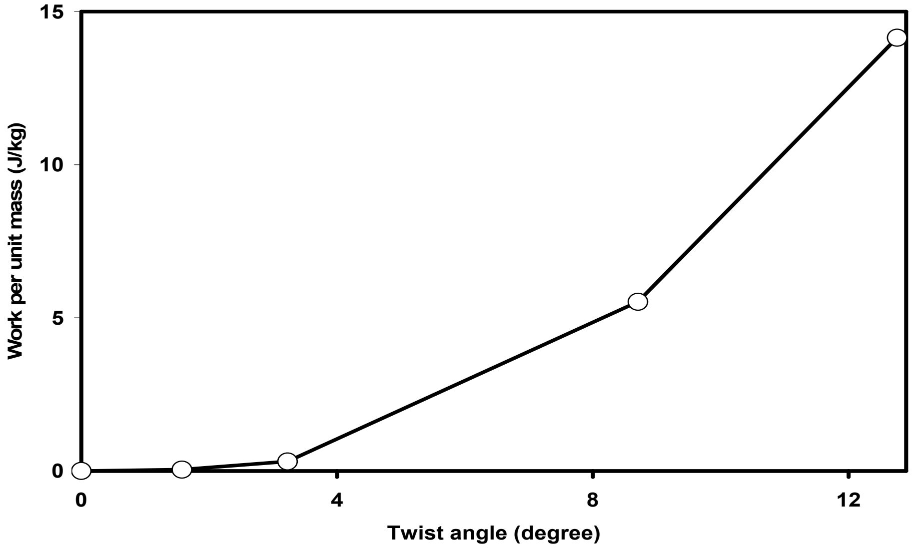

Figure 152. Work per unit mass (split beam with nastic actuator) is shown.
As a conclusion, work per unit mass of nastic actuator is as high as 2592~13900% than electric motor system (Figure 153) because nastic actuator uses much lighter material than motors.

.

6.2.1 The weight of the nastic actuator for split beam

- Calculation of the mass of rubber block

- FMSC 1035 Polyurethane; Gallon kit – Net. Wt. 16 lbs=7.2576Kg

$$1 \text{ Gallon} = 3.7854\ l = 3.7854\times10^{6}\text{mm}^{3}.$$

- Density of 1035 polyurethane= 7.2576Kg/(3.7854×10^{6}mm^{3})=1.9173×10^{6}Kg/mm^{3}

- Density of rubber block (shear actuator) = 6000 mm^{3}.

Therefore, weight of rubber block = Density×Volume=0.0115 Kg.

- Weight of Kevlar fabric; 6.5 oz per square yard.

We need 55.8 in^{2} Kevlar fabric. By the unit conversions and calculations, the weight of Kevlar fabric is 0.00793388 kg.

- Weight of tube fitting; 0.01 g.

We need 250 fittings, so total weight of tube fitting=2.5g=0.0025kg

- Weight of nylon tube per unit length; 7.112×10^{-6} kg/m

We need 5” long tube for each single actuator, so for 250 cells, 104.17 ft = 31.7514m needed. Therefore, total weight of nylon tube = 0.00022582kg

- Total weight of nastic actuator = rubber block+Kevlar fabric+tube fitting+nylon tube

=0.02216 kg

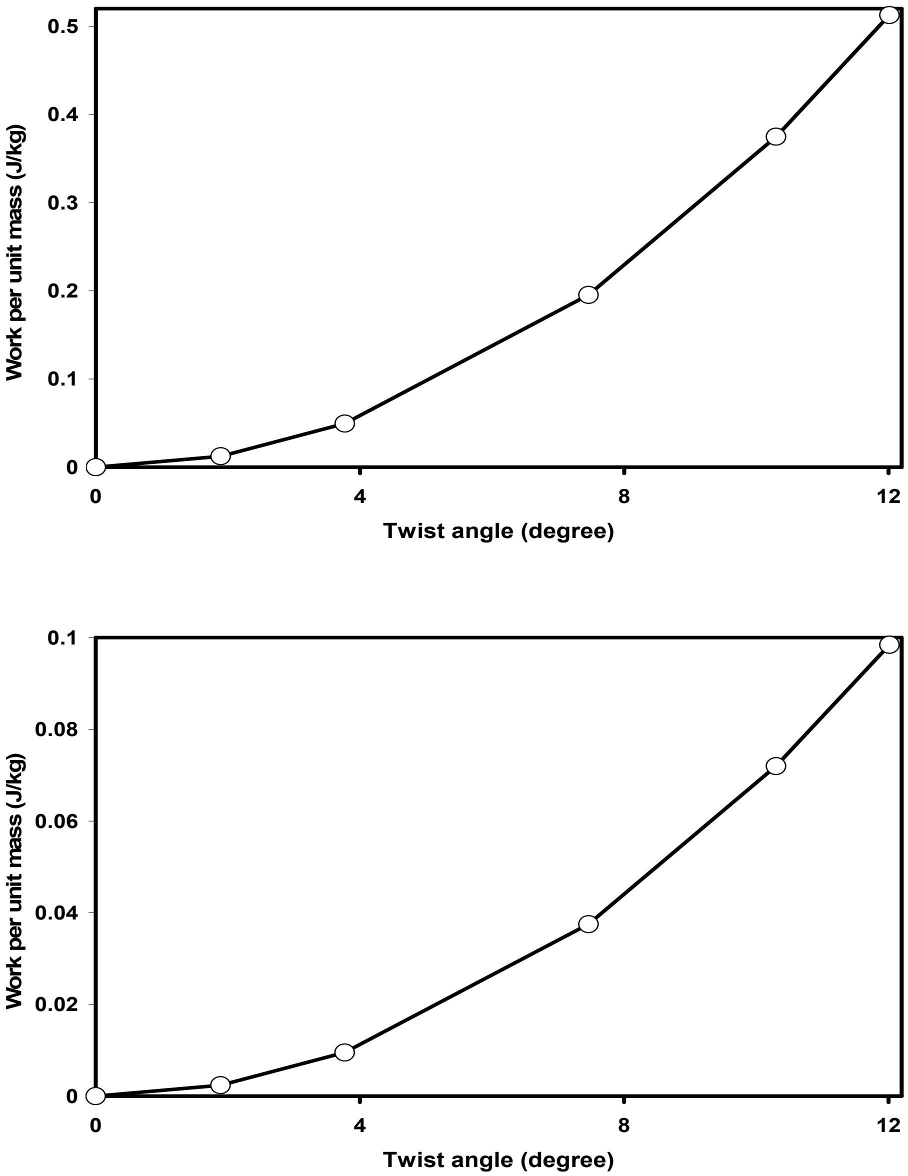

Figure 153. Work per unit mass for split beam with conventional actuator are shown; (top) motor 1, (bottom) motor 2. Comparison with nastic actuator is discussed in Figure 152.

6.2.2 Calculation of the weight of the conventional beam

- Weight of the rod (AISI 1010 Steel) = 2.967 Kg
- Weight of the triangular beam (Aluminum Alloy 6061-O) = 0.65475 Kg
- Weight of the motor; Motor 1 = 15.4 Kg (equivalent model from other supplier)

  Motor 2 = 92.7 Kg

Therefore, total weight of the conventional beam; Motor 1 = 19.02 Kg

Motor 2 = 96.32 Kg

Work per unit mass for split beam with conventional actuator is shown in Figure 153.

6.3 Price of the Triangular Beam Systems

The prices for each actuating system are based upon the estimate of commercial product, mostly from web-based merchandizing sites, and are shown in Table 6 and Table 7.

Table 6. Nastic actuator (rubber-block)

Part	Supplier	Unit price	EA	Total
Freeman 1035 Polyurethane	Freeman Supply	$96.55 per Gallon kit	1 Gallon	$96.55
Double pinch hose and tube clamp	McMaster	$8.00 per pack of 25	10 Pack (250 EA)	$80
Nylon tube	McMaster	$22.40 26" long	10	$16.67
Toy Balloon		$1.00 (assumed) Per pack of 10	25	$25.0
Kevlar fabric		$13.00 8 inches wide by 13 feet long	1	$13.00
Total:				$231.22

Table 7. Conventional beam with motors

Part	Supplier	Unit price	EA	Total
Steel rod	Freeman Supply	\$22.30 16mm diameter and 304.8mm long (12")	1	\$96.55
Motor1	McMaster	\$3476	1	\$3476
Motor2	McMaster	\$607	1	\$607
Total:				\$3572.55 (Motor1) \$703.55 (Motor2)

As shown in the tables above, the nastic actuator is much cheaper than the conventional system, especially due to the high price of the motors. The work per unit mass vs. prices of each system is shown in Figure 154. The nastic actuator shows higher work performance and lower price than the conventional actuating systems.

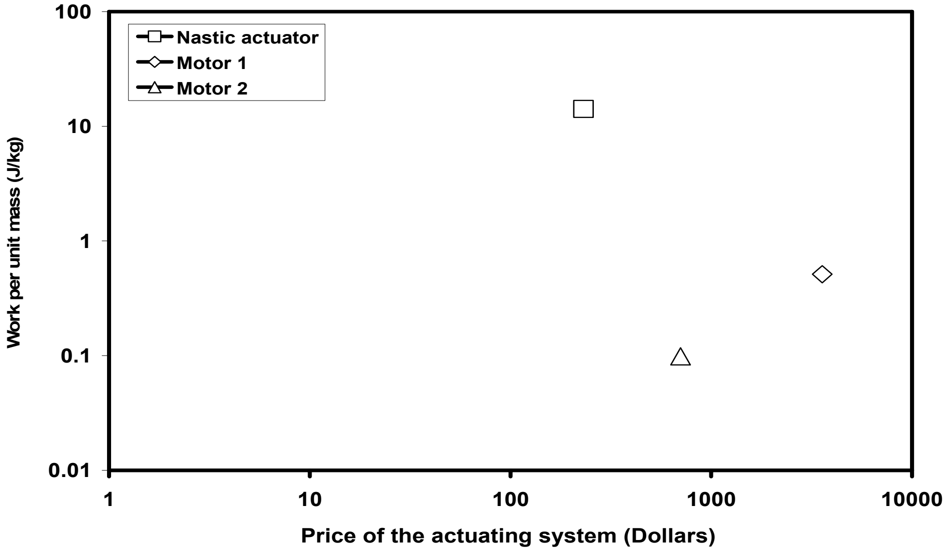

Figure 154. Work per unit mass vs. Price of the system is shown. The price of nastic actuator is much cheaper than conventional actuating system with motors as 204~1445%.

6.4 Power Output for Triangular Beams

As commented in the previous chapter, the power of the system is defined as

Power: 1W = 1 J/s

To calculate the power, the operating frequency is assumed as 1 Hz for triangular beams. In both aspects of power outputs (volumetric power and power per unit mass), the nastic actuator shows much superior performance than the conventional actuator systems (Figure 155).

- For volumetric power (power output per unit volume)

- Nastic actuator (rubber block): 59.7 KW/m^3

- Conventional beam, Motor 1: 2.576 KW/ m^3

Motor 2: 0.686 KW/ m^3

- For power per unit mass,

- Nastic actuator: 14.14 W/kg

- Conventional beam, Motor 1: 0.513 W/ kg

Motor 2: 0.0984 W/kg

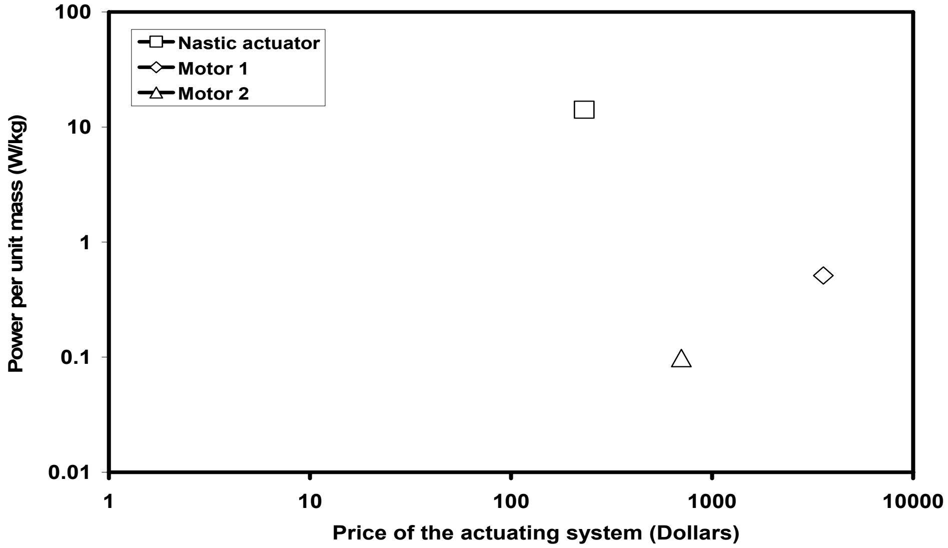

Figure 155. Power per unit mass vs. Price of the system is shown. The power per unit mass of nastic actuator is 2217~8602% higher than conventional actuating system with electric motors.

6.5 Summary

As a conclusion, the nastic actuator has much superior work performance and power compared to the conventional actuator. Conventional actuators using commercial electric motors need 3047% higher input force to implement same degree of twist angle than the nastic actuator. Please note that if we use the work calculation for reaction forces of the beams, the work will be almost identical for nastic and conventional actuator because twist angles are same. The work performance (work per unit volume) of nastic actuator is 2280~8471% higher than conventional actuator because the volume of nastic actuator is much smaller than the conventional actuator using electrical motors. This means nastic actuator is much efficient than conventional actuator.

Another measure of work density is work per unit mass. This definition of work performance is important for aerospace vehicles, especially for satellites because of their weight constraints. Nastic actuator is also 2592~13900% higher performance than conventional actuator because the actuator is composed of much lighter materials.

For volumetric power, the nastic actuator is 2217~8602% higher than conventional actuators. Also the nastic actuator is 2656~14269% higher than conventional actuators for power per unit mass.

Even with higher performances, the price of nastic actuator is much cheaper (204~1445%) because of the high prices of the electric motors for conventional actuators.

As with the comparisons above, the nastic actuator might be helpful to the industrial world to save energy and materials, as well as the costs when applied to real applications, for example, commercial structures.

CHAPTER VII

CONCLUSIONS, APPLICATIONS, AND FUTURE WORK

This chapter presents the conclusion from experiments and analysis of nastic shear actuator, some possible applications, and suggested future work for structural application by implementing micro-actuation technology.

7.1 Conclusions

The lens shaped element is designed by first-order geometric analysis, and is embedded into the polymer matrix. The lens element is made from Kevlar fabric, and soft polyurethane made the matrix.

The hyperelastic material property has been found experimentally and numerically. Simple tensile test and planar tension test have been performed to characterize hyperelastic material property of matrix. Optical measurement shows planar tension test results can be converted to pure shear data. Biaxial test is guessed from typical stress-strain relationship of elastomer, and added to set of hyperelastic material curves. Though the good fitting throughout the whole deformation range is difficult due to the complex nature of elastomer material, the Ogden material constant set is shown good agreement within the working range of shear actuator.

A single-element shear actuator is fabricated, and tested free strain behavior. Peak shear strain is over 30% when pressurized with 1.03 MPa.

Unit cell and the array of single-direction and two-direction shear actuator is modeled to check the single and multi-cell behavior. Work performance and power of the actuator are calculated from numerical analysis. The performance of the array shows consistent property after 5 or 7 repeated unit cells.

The application of nastic actuator to the structural beam shows its advantage compared to the conventional actuating mechanism. The work performance, power, and the prices of the nastic actuator system is estimated much higher, by the order of 10^3 or 10^4, than the conventional electric motors.

7.2 Applications

One of the possible applications is the novel aerospace vehicle using tilt-rotor system (Figure 156). The nastic actuator can provide quick shape change during the operations, that is stilly carrying the structural loads.

Also, the variable (controllable) pitch propellers (Figure 157) for aircraft and ships can be the applications. As the direction and speed of the vehicle change, the nastic actuator can provide more flexibility to the vehicle, quick response, and save the fuels.

Figure 156. V-22 Osprey [100]

Figure 157. Variable (controllable) pitch propellers [101]; Aircraft (left) and Ship (right)

Another possible application is for offshore industry. For an oil well or oil platform (Figure 158), the blowout preventer (BOP) in Figure 159 is used to close the valve if gas overpressure is significant. This might keep the platform and lives of oil workers.

The requirement for blowout preventer is to have fast response time and large blocked pressure. From the characteristics of nastic actuator, it will be worth to condider the application for this area.

Figure 158. An offshore oil/gas platform ([102])

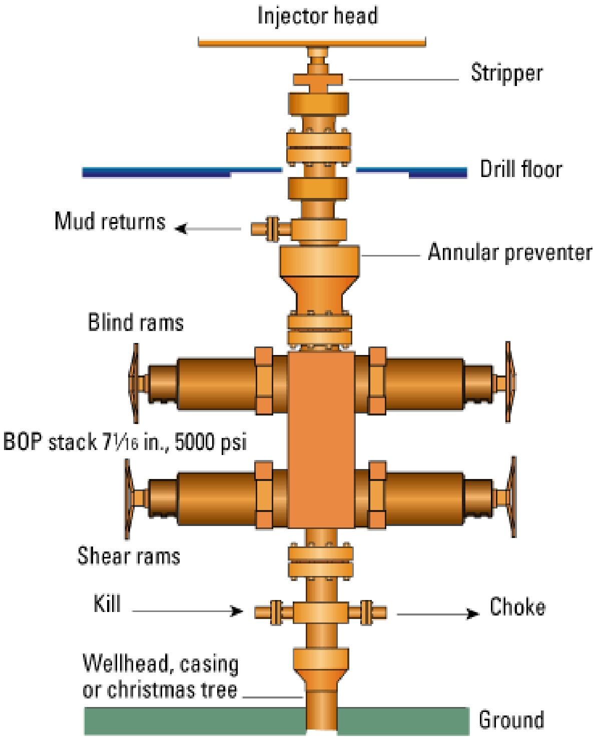

Figure 159. A blowout preventer ([103])

7.3 Future Work

In consideration of hyperelastic material tests, equi-biaxial extension test is not performed, and is substituted by FEA simulations in this study due to the limitation of the testing machines. Implementation of this test can make a whole set of hyperelastic tests, and might enable better fitting of hyperelastic material constants.

In this work, nastic actuator has applied to a split beam. The various shapes of structural applications, for example, sandwich panel using nastic actuator core, can be designed. It might make more efficient way for the structures with specific deformation behavior required.

Finally, the actuation mechanism of micro cells might be the issue when embedded in moving vehicles. The concept of active protein actuation by Sundaresan and Leo [50, 52, 53] was explained in Chapter II. Here in this work, a proposed concept of micro-actuation called "closed cell gas generation" [2, 104] is considered.

7.3.1 Actuation of micro cell by closed cell gas generation

By using Ni-H_2 battery technology, hydrogen (H_2) gas is generated with electrolysis for actuation. This technology controls the volume of cells from electrochemical production of gases. The calculation example for checking the advantage of application follows.

- The change in actuator volume is (ΔV)=0.04624 cc from lens volume change of single shear actuator
- Maximum actuation pressure for single shear actuator ≈ 15 MPa.
- If we assume the operating frequency as 1 Hz, then volume flow rate is

$$\Delta V \times f = 0.04624\text{cc/sec}.$$

- The corresponding number of moles of H_2 can be calculated from ideal gas law (assume room temperature) is

$$n = \frac{PV}{\overline{R}T} = 2.939 \times 10^{-4}\,\text{mol}$$

- 2n moles of electron need assume 100% conversion efficiency, and 96,485 Coulombs to create one mole of electrons. 2Fn=15 Ams/actuator.
- Corresponding power density is 12779.3W/m^3.

- For conventional hydraulic oil actuator with 15.48MPa and 0.04624cc volume change, and assuming 0.8 pumping efficiency, resulting power is 0.895 W/actuator.

REFERENCES

1. Chee CYK., Tong L, Steven GP. A review on the modellling of piezoelectric sensors and actuators incorporated in intelligent structures. Journal of Intelligent Material Systems and Structures 1998;9:3-19.
2. Sater J, Main J. Plants and mechanical motion - nastic materials at DARPA. Proc. International Conference on Adaptive Structure Technology, Bar Harbor, Maine, 2004, pp 1-8.
3. Tzou HS, Lee HJ, Arnold SM. Smart Materials, precision sensors/actuators, smart structures, and structronic systems. Mechanics of Advanced Materials and Structures 2004;11:367-393.
4. Kellogg R., Flatau A. Blocked-force characteristics of Terfenol-D transducers. Journal of Intelligent Material Systems and Structures 2004;5:117-128.
5. Gandhi MV, Thompson BS. Smart Materials and Structures. London: Chapman & Hall; 1992.
6. Banks HT, Smith RC, Wang Y. Smart Material Structures. Chichester, New York: John Wiley & Sons; 1996.
7. Chopra I. Review of state of art of smart structures and integrated systems. AIAA Journal, 2002;40:2145-2187
8. Cady WG. Piezoelectricity; an introduction to the theory and applications of electromechanical phenomena in crystals. New York: Dover Publications; 1964.

9. Lagoudas DC, Bo Z. The cylindrical bending of composite plates with piezoelectric and SMA layers. Smart Materials and Structures 1994;3:309-317.
10. Boyd JG, Lagoudas DC. A thermodynamical constitutive model for shape memory materials. Part I. the monolithic shape memory alloy. International Journal of Plasticity 1996;12(6):805-842.
11. Aboudi J. Micromechanically based constitutive equations for shape-memory fiber composites undergoing large deformations. Smart Materials and Structures. 2004;13: 828-837.
12. Elzey DM, Sofla AYN, Wadley HNG. Shape memory-based multifunctional structural actuator panels. Proc. SPIE Smart Structures and Materials: Industrial and Commercial Applications of Smart Structures Technologies; San Diego, CA, 2002, pp 192-200.
13. Dano ML, Hyer MW. SMA-induced snap-through of unsymmetric fiber-reinforced composite laminates. International Journal of solids and Structures 2003;40:5949-5972.
14. Dean DR, James LT. Adaptive laser optics techniques (ALOT). 1st DOD Conference on High Energy Laser Technology, Naval Training Center, San Diego, CA, 1974, pp 1-10.
15. dos Santos e Lucato SL, Wang J, Maxwell P, McMeeking RM, Evans AG. Design and demonstration of a high authority shape morphing structure. International Journal of Solids and Structures 2004;41:3521–3543
16. Hutchinson RG, Wicks N, Evans AG, Fleck NA, Hutchinson JW. Kagome plate structures for actuation. International Journal of Solids and Structures, 2003;40:6969-6980.

17. Wlezien, RW, Horner GC, McGowan AR, Padula SL, Scott MA, Silcox RJ, Simpson JO. The aircraft morphing program. AIAA Journal, 1998;1927:1-13.
18. Simpson JO, Wise SA, Bryant RG, Cano RJ, Gates TS, Hinkely JA, Rogowski RS, Whitley, KS. Innovative materials for aircraft morphing. NASA 98-5 SPIE.
19. Lee DH. Aeroelastic studies on a folding wing configuration. in 46th AIAA/ASME/ASCE/AHS/ASC Structures, Structural Dynamics & Materials Conference. 18-21 April 2005. Austin, Texas.
20. Morphing aircraft structures. Available at www.darpa.mil/dso/archives/mas/index.htm; 2008.
21. Cadogan D, Graham W, Smith T. Inflatable and rigidizable wings for unmanned aerial vehicles. in 2nd AIAA "Unmanned Unlimited" Systems, Technologies, and Operations. 15-18 September 2003. San Diego, California.
22. Cadogan D, Smith T, Uhelsky F, MacKusick M. Morphing inflatable wing development for compact package unmanned aerial vehicles. in Proc. 45th AIAA/ASME/ASCE/AHS/ASC Structures, Structural Dynamics & Materials Conference. 19-22 April 2004. Palm Springs, California, pp 1-13.
23. Allred RE, Hoyt AE, Harrah LA, McElroy PM, Scarborough S, Cadogan D, Pahle JW. Light curing rigidizable inflatable wing. in Proc. 45th AIAA/ASME/ASCE/AHS/ASC Structures, Structural Dynamics & Materials Conference. 19-22 April 2004. Palm Springs, California, pp 1-15.
24. Cadogan D, Scarborough S, Gleeson D, Dixit A, Jacob J, Simpson A. Recent development and test of inflatable wings. in Proc. 47th AIAA/ASME/ASCE/AHS/ASC

Structures, Structural Dynamics & Materials Conference. 1-4 May 2006. Newport, Rhode Island, pp 1-15.

25.Simpson A, Santhanakrishnan A, Jacob J, Smith S, Lumpp J, Cadogan D, Mackusick M, Scarborough S. Flying on air: UAV flight testing with inflatable wing technology. in AIAA 3rd “Unmanned Unlimited” Technical Conference, Workshop and Exhibit. 20-23 September 2004. Chicago, Illinois, pp 1-14.

26. Usui M, Jacob J, Smith S, Scarborough S, Cadogan D. Second generation inflatable/rigidizable wings for low-density flight applications. in Proc. 46th AIAA/ASME/ASCE/AHS/ASC Structures, Structural Dynamics & Materials Conference. 18-21 April 2005. Austin, Texas, pp 1-9.

27. Marks P. Acrobatic robot set to fly with the flock. New Scientist, 2007;194(2611):26.

28. Morphing aircraft mimics a bird on the wing. Available at www.newscientist.com/ article/dn13419-morphing-aircraft-mimics-a-bird-on-the-wing.html; 2008.

29. Muller UK, Lentink D. Turning on a dime. Science 2004;306(5703):1899-1900.

30. Lentink D, Muller UK, Stamhuis EJ, de Kat R, van Gestel W., Veldhuis LLM, Henningsson P, Hedenstrom A, Videler JJ, van Leeuwen JL, How swifts control their glide performance with morphing wings. Nature 2007;446:1082-1085.

31. Christodoulou L, Venables JD. Multifunctional material systems: The first generation. Journal of Materials 2003;55(12):39-45.

32. Momoda LA, The future of engineering materials : Multifunction for performance-tailored structures. Washington DC: National Academy of Engineering (NAE).

33. Matic P. Overview of multifunctional materials. in Smart Structures and materials:Active materials: Behaviors and mechanics, Proceedings of SPIE. 2003, pp 61-69.
34. Hawkins GF, Augmenting the mechanical properties of materials by embedding simple machines. Journal of Advanced Materials 2002;34(3):16-20.
35. Kim J. Passive machine augmented composite for multifunctional properties, Ph.D. dissertation, Texas A&M University: College Station, 2005.
36. Kim J, Creasy TS, Hawkins GF, O'Brien MJ. Performance of a machine augmented composite. in Proc. Annual Technological Conference, Boston, MA. 2005, pp 1258-1262.
37. McCutcheon DM, Machine augmentation composite materials for damping purposes, M.S. thesis, Texas A&M University: College Station, 2004.
38. McCutcheon DM, Reddy JN, Ochoa O, O'Brien MJ, Creasy TS, Hawkins GF. Development of damping machine augmented composite materials. in Proc. Annual Technological Conference, Boston, MA. 2005, pp 1263-1267.
39. McCutcheon DM, Reddy JN, O'Brien M J, Creasy TS, Hawkins GF. Damping composites materials by machine augmentation. Journal of Sound and Vibration, In press.
40. Huber JE, Fleck NA, Ashby MF. The selection of mechanical actuators based on performance indices. Proc. R. Soc. Lond. A. 1997;453:2185-2205.
41. Findlay GP. Nastic movements, In: Wilkins MB, editor. Advanced Plant Physiology. London: Pitman.1984 pp 186-200.

42. Hill BS, Findlay GP, The power of movement in plants: the role of osmotic machines. Quarterly Reviews of Biophysics 1981;14:173-222
43. Darwin C. The Power of Movement in Plants. New York: Appleton, 1896.
44. Bose SJC. The Nervous Mechanism of Plants. London: Longmans, Green and Co., 1926.
45. Bose SJC. The Motor Mechanism of Plants. London: Longmans, Green and Co., 1928.
46. Bose SJC. Growth and Tropic Movements of Plants. London: Longmans, Green and Co., 1929.
47. Selsam M.E. Plants that Move. New York: Morrow, 1962.
48. Forterre Y, Skotheim JM, Dumais J, Mahadevan L. How the Venus flytrap snaps. Nature 2005;433:421-425
49. Nastic materials. Available at www.darpa.mil/dso/thrust/matdev/nastic.htm; 2006.
50. Sundaresan VB, Leo DJ. Experimental investigation for chemo-mechanical actuation using biological transport mechanisms. in IMECE2005-81366. 5-11 November 2005. Orlando, Florida.
51. Giurgiutiu V, Matthews L, Leo DJ, Sundaresan VB. Concepts for power and energy analysis in nastic structures. in IMECE2005-82786. 5-11 November, 2005. Orlando, Florida.
52. Mattews L, Sundaresan VB, Giurgiutiu V, Leo DJ. Bioenergetics and mechanical actuation analysis with membrane transport experiments for use in biomimetic nastic structures. Journal of Materials Research 2006;21(8):2058-2067.

53. Sundaresan VB, Leo DJ. Controlled fluid transport using ATP-powered protein pumps. Smart Mater. Struct. 2007;16:207-213.
54. Crocker LE, Duncan BC, Hughes RG, Urquhart JM. Hyperelastic modeling of flexible adhesives. National Physical Laboratory Report No. CMMT (A) 183, 1999.
55. Duncan BC, Test methods for determining hyperelastic properties of flexible adhesives. National Physical Laboratory Report No. CMMT (MN) 054, 1999.
56. Duncan BC, Maxwell AS, Crocker LE, Hunt R. Verification of hyperelastic test methods. National Physical Laboratory Report No. CMMT (A) 226, 1999.
57. Nonlinear Finite Element Analysis of Elastomers, MSC software Co., Santa Ana, CA.
58. Compression or biaxial extension. Axel products, Inc., Ann Arbor, MI.
59. Gent AN, Chang TYP, Leung MB. Fracture and fatigue of bonded rubber blocks under compression. Engineering Fracture Mechanics 1993;44:843~855.
60. Gent AN, Lindley PB. Internal rupture of bonded rubber cylinders in tension. Proceedings of the Royal Society of London A 1958;249:195~205.
61. Gent AN, Meinecke EA. Compression, bending and shear of bonded rubber blocks. Polymer Engng Sci. 1970;10:48~53.
62. Large deformation nonlinear mechanics. Available at www.engin.umich.edu/class/bme506/bme5062000/bme506formlec/largedeflec/largedef.htm#surfmap; 2006.
63. Crisfield MA, Non-linear Finite Element Analysis of Solids and Structures. Chichester, New York: John Wiley & Sons, 1997.
64. Mooney M. A theory of large elastic deformations. J. Appl. Phys. 1940;11:582-592.

65. Rivlin RS. Large elastic deformations of isotropic materials. Phil. Trans. R. Soc. Lond. A. 1948;241:379-397.
66. Valanis KC, Landel RF. The strain energy function of a hyperelastic material in terms of the extension rations. J. Appl. Phys. 1967;38:2997-3002.
67. Ogden RW. Large deformation isotropic elasticity – on the correlation of theory and experiment for incompressible rubberlike solids. Proceedings of the Royal Society of London. Series A, Mathematical and Physical Sciences 1972;326(1567):565-584.
68. Ogden RW. Large deformation isotropic elasticity – on the correlation of theory and experiment for compressible rubberlike solids. Proceedings of the Royal Society of London. Series A, Mathematical and Physical Sciences 1972;328(1575):567-583.
69. Arruda EM, Boyce MC. A three-dimensional constitutive model for the large stretch behavior of rubber elastic materials. J. Mech. Phys. Solids 1993;41(2):389-412.
70. Oden JT. Finite Elements of Nonlinear Continua. New York: McGraw-Hill, 1972.
71. Oden JT, Kikuch N. Finite element method for constrained problems in elasticity. Int. J. for Num. Meth. in Engng. 1982;18:701-725.
72. Malkus DS, Hughes TJR. Mixed finite element methods-reduced and selective integration techniques: a unification of concepts. Computer Methods in Applied Mechanics and Engineering 1978;15:68-81.
73. Duffett G, Reddy BD. The analysis of incompressible hyperelastic bodies by the finite element method. Computer Methods in Applied Mechanics and Engineering 1983;41: 105-120.

74. Sussman T, Bathe KJ. A finite element formulation for nonlinear incompressible elastic and inelastic analysis. Computers & Structures 1987;26:357-409.
75. Gadala MS. Alternative methods for the solution of hypelastic problems with incompressiblility. Computers & Structures 1992;42:1-10.
76. Dobrowolski M. A mixed finite element method for approximating incompressible materials. SIAM Journal on Numerical Analysis, 1992;29(2):365-389.
77. Saleeb AF, Chang TYP, Arnold SM. On the development of explicit robust schemes for implementation of a class of hyperelastic models in large-strain analysis of rubbers. International Journal for Numerical Methods in Engineering 1992;33:1237-1249.
78. Simo JC, Pister KS. Remarks on rate constitutive equations for finite deformation problems: computational implications. Computer Methods in Applied Mechanics and Engineering 1984;46:201-215.
79. Simo JC, Taylor RL, Pister KS. Variational and projection methods for the volume constraint in finite deformation elasto-plasticity. Computer Methods in Applied Mechanics and Engineering 1985;51:177-208.
80. Simo JC, Ortiz M. A unified approach to finite deformation elastoplastic analysis based on the use of hyperelastic constitutive equations. Computer Methods in Applied Mechanics and Engineering 1985;49:221-245.
81. Simo JC, Taylor RL. Quasi-incompressible finite elasticity in principal stretches. Continuum basis and numerical algorithms. Computer Methods in Applied Mechanics and Engineering 1991;85:273-310.

82. Urayama K. An experimentalist’s view of the physics of rubber elasticity. Journal of Polymer Science: Part B 2006;44:3440-3444.
83. Treloar LRG. The Physics of Rubber Elasticity. Oxford, UK: Oxford Unversity Press,1975.
84. Rivlin RS, Saunders DW. Large elastic deformations of isotropic materials: VII. Experiments on the deformation of rubber. Phil. Trans. R. Soc. Lond. A. 1951;243: 251-288.
85. Urayama K. An experimentalist’s view of the physics of rubber elasticity. Journal of Polymer Science: part B 2006.
86. Mullins L. Effect of stretching on the properties of rubber. Journal of Rubber Research 1947;16:275-289.
87. Mullins L. Thixotropic behavior of carbon black in rubber. Journal of Physical Chemistry 1950;54(2):239-251.
88. Mullins L, Tobin NR. Stress softening in rubber vulcanizates. Use of a strain amplification factor to describe the elastic behavior of filler-reinforced vulcanized rubber. Journal of Applied Polymer Science 1965;9:2993-3009.
89. Mullins L. Softening of rubber by deformation. Rubber Chemistry and Technology 1969;42:339–361.
90. Liff SM. Mullins effect and thixotropy. 2006 NNF Summer reading Series. Department of Mechanical Engineering, Cambridge, MA: MIT.
91. Circle-circle intersection. Available at mathworld.wolfram.com/Circle–CircleIntersection.html; 2006.

92. Ewumi OF. Experimentally characterized embedded McKibben muscles as a nastic material for biomedical applications, M.S. Thesis, Texas A&M University: College Station, Texas, 2007.
93. Treloar LRG. Stress-strain data for vulcanized rubber under various types of deformation. Transactions of the Faraday Society 1944;40:59-70.
94. Miller K. Experimental loading conditions used to implement hyperelastic and plastic material models. Axel products, Inc., Ann Arbor, MI.
95. Bradley GL, Chang PC, McKenna GB. Rubber modeling using uniaxial test data. Journal of Applied Polymer Science 2001;81:837-848.
96. Metals Handbook, 2nd ed. Davis JR, ed. Materials Park, OH: The Material Information Society, 1998.
97. Aluminum alloy 6061-O. Available at www.matweb.com/search/DataSheet.aspx?MatID= 9386; 2007.
98. AISI 1010 steel. Available at www.matweb.com/search/DataSheet.aspx?MatID=6782&ckck=1; 2007.
99. DC gear motors. Available at www.mcmaster.com; 2008.
100. V-22 osprey. Available at en.wikipedia.org/wiki/V-22_Osprey; 2008.
101. Controllable pitch propeller. Available at en.wikipedia.org/wiki/Controllable_pitch_propeller; 2008.
102. Typical oil platform. Available at en.wikipedia.org/wiki/Oil_platform; 2008.
103. Blowout preventer. Available at en.wikipedia.org/wiki/Blowout_preventer; 2008.
104. Controllable active materials via internally generated pressure. by Texas A&M

University and Aerospace Corporation, Research proposal to DARPA (Defense Advanced Research Projects Agency), 2004.

VITA

Sang Jin Lee was born and raised in Seoul, Korea. He received his B.S. degree in 1993 and M.S. degree in 1996 from the Department of Mechancial Engineering of Ajou University, Suwon, Korea. After 4.5 years of industry experience in his home country, he started graduate study at Penn State University where he received another M.S. degree in 2002, and then he and his family moved to College Station, Texas for his Ph.D. study in the Department of Mechanical Engineering, Texas A&M University. He acquired his Ph.D. degree in December 2008.

Sang Jin Lee can be reached at c/o Dr. Creasy, Department of Mechanical Engineering, Texas A&M University, 309 Engineering/Physics Building, College Station, TX 77843-3123. Sang Jin's email address is gooree@hotmail.com.